UNIVERSITY OF CALIFORNIA SAN DIEGO

Physical controls on Southern Ocean biogeochemistry

A dissertation submitted in partial satisfaction of the
requirements for the degree Doctor of Philosophy

in

Oceanography

by

Channing J. Prend

Committee in charge:

Professor Sarah T. Gille, Chair
Professor Lynne D. Talley, Co-Chair
Professor Peter J. S. Franks
Professor Matthew R. Mazloff
Professor David Saintillan

2022

The Dissertation of Channing J. Prend is approved, and it is acceptable in quality and form for publication on microfilm and electronically.

University of California San Diego

2022

EPIGRAPH

Eventually man, too, found his way back to the sea. Standing on its shores, he must have looked out upon it with wonder and curiosity, compounded with an unconscious recognition of his lineage. He could not physically re-enter the ocean as the seals and whales. But over the centuries, with all the skill and ingenuity and reasoning powers of his mind, he has sought to explore and investigate even its most remote parts, so that he might re-enter it mentally and imaginatively.

Rachel Carson

TABLE OF CONTENTS

References . . . 112

LIST OF FIGURES

ACKNOWLEDGEMENTS

First and foremost, I would like to thank my advisors, Sarah Gille and Lynne Talley. They are not only brilliant scientists, but also kind and humble people. I could not have completed this dissertation without Sarah's careful thought or Lynne's infectious curiosity. I admire them both so much and working together has truly been a pleasure.

I am also grateful to Sarah and Lynne for giving me the freedom to travel and collaborate with numerous other scientists during my PhD. Chapter 3 is based on work that I conducted with Glenn Flierl as a fellow in the Geophysical Fluid Dynamics Program at WHOI. Thanks to Glenn for his unwavering patience and deep knowledge of ecosystem modeling. Chapter 5 stems from work done at LOCEAN-IPSL as a Chateaubriand fellow, hosted by Marina Lévy and JB Sallée. Thanks to Marina and JB for their enthusiasm and creativity, which continue to be a source of motivation and inspiration to me.

Next, I have to thank my committee members, Matt Mazloff, Peter Franks, and David Saintillan, who have been an invaluable resource over the past few years. Their limitless supply of thoughtful questions and optimism have made writing my dissertation infinitely more enjoyable.

I would be remiss if I did not mention several mentors from my undergraduate career. I simply would not be an oceanographer without Ryan Abernathey, who introduced me to the field and encouraged me to pursue it. Hyodae Seo and Bob Weller were also instrumental in my development as a scientist and generously guided me through the process of writing my first paper. Special thanks to Bob Anderson for teaching me about ocean biogeochemistry during my final semester of college, which greatly influenced my research focus in graduate school.

Finally, thank you to my family and friends for their continual support. To my parents and sisters for always believing in me. To the 2017 PO cohort—Bobby, Emma, Lauren, Annie, Noel, and Alice—for commiserating through the ups and downs of graduate school (and teaching me dimensional analysis). To Julia, Abigail, and Koiya for making Bonair feel like home. And lastly, to all the students, faculty, and staff at Scripps for making my time here so memorable.

Chapter Two, in full, is a reprint of the material as it appears in the Journal of Geophysical Research: Oceans, 2019. Prend, C. J., S. T. Gille, L. D. Talley, B. G. Mitchell, I. Rosso, and M. R. Mazloff (2019), Physical drivers of phytoplankton bloom initiation in the Southern Ocean's Scotia Sea, *Journal of Geophysical Research: Oceans*, 124, 5811-5826. The dissertation author was the primary investigator and author of this paper.

Chapter Three, in full, is a reprint of the material as it appears in Geophysical Research Letters, 2021. Prend, C. J., G. R. Flierl, K. M. Smith, and A. K. Kaminski (2021), Parameterizing eddy transport of biogeochemical tracers, *Geophysical Research Letters*, 48, e2021GL094405. The dissertation author was the primary investigator and author of this paper.

Chapter Four, in full, has been submitted to Global Biogeochemical Cycles. Prend, C. J., A. R. Gray, L. D. Talley, S. T. Gille, F. A. Haumann, K. S. Johnson, S. C. Riser, I. Rosso, J. Sauvé, and J. L. Sarmiento (submitted), Indo-Pacific sector dominates Southern Ocean carbon outgassing, *Global Biogeochemical Cycles*. The dissertation author was the primary investigator and author of this paper.

Chapter Five, in full, has been submitted to Global Biogeochemical Cycles. Prend, C. J., M. G. Keerthi, M. Lévy, O. Aumont, S. T. Gille, L. D. Talley (submitted). Sub-seasonal forcing drives year-to-year variations of Southern Ocean primary productivity, *Global Biogeochemical Cycles*, submitted. The dissertation author was the primary investigator and author of this paper.

VITA

2017 B. A. in Earth Science & Mathematics (*cum laude*), Columbia University

2022 Ph. D. in Oceanography, University of California San Diego

PUBLICATIONS

Prend, C. J., H. Borstlap, M. M. Carranza, S. T. Gille, M. Lévy, L. D. Talley (2022). Seasonal variability of deep chlorophyll maxima in an oligotrophic regime, in prep.

Brand, S. V., C. J. Prend, L. D. Talley (2022). Modification of North Atlantic Deep Water by Pacific/Upper Circumpolar Deep Water in the Argentine Basin, *Geophysical Research Letters*, submitted.

Prend, C. J., M. G. Keerthi, M. Lévy, O. Aumont, S. T. Gille, L. D. Talley (2022). Sub-seasonal forcing drives year-to-year variations of Southern Ocean primary productivity, *Global Biogeochemical Cycles*, submitted.

Prend, C. J., A. R. Gray, L. D. Talley, S. T. Gille, F. A. Haumann, K. S. Johnson, S. C. Riser, I. Rosso, J. Sauvé, J. L. Sarmiento (2022). Indo-Pacific sector dominates Southern Ocean carbon outgassing, *Global Biogeochemical Cycles*, submitted.

Keerthi, M. G., C. J. Prend, O. Aumont, M. Lévy (2022). Small spatio-temporal scales dominate year-to-year phytoplankton changes globally, *Nature Geoscience*, in revision.

Prend, C. J., J. M. Hunt, M. R. Mazloff, S. T. Gille, L. D. Talley (2022). Controls on the boundary between thermally and non-thermally driven pCO_2 regimes in the South Pacific, *Geophysical Research Letters*, in revision.

Prend, C. J., G. R. Flierl, K. M. Smith, A. K. Kaminski (2021). Parameterizing eddy transport of biogeochemical tracers, *Geophysical Research Letters*, 48, e2021GL094405.

von Berg, L., C. J. Prend, E. C. Campbell, M. R. Mazloff, L. D. Talley, S. T. Gille (2020). Weddell Sea phytoplankton blooms modulated by sea ice variability and polynya formation, *Geophysical Research Letters*, 47, e2020GL087954.

Uchida, T., D. Balwada, R. P. Abernathey, C. J. Prend, E. Boss, S. T. Gille (2019). Southern Ocean phytoplankton blooms observed by biogeochemical floats, *Journal of Geophysical Research: Oceans*, 124, 7328-7343.

Prend, C. J., S. T. Gille, L. D. Talley, B. G. Mitchell, I. Rosso, M. R. Mazloff (2019). Physical drivers of phytoplankton bloom initiation in the Southern Ocean's Scotia Sea, *Journal of Geophysical Research: Oceans*, 124, 5811-5826.

Weller, R. A., J. T. Farrar, H. Seo, C. J. Prend, D. Sengupta, J. Sree Lekha, M. Ravichandran, R. Venkatsen (2018). Moored observations of the surface meteorology and air-sea fluxes in the northern Bay of Bengal in 2015, *Journal of Climate*, 32, 549-573.

Prend, C. J., H. Seo, R. A. Weller, J. T. Farrar (2018). Impact of freshwater plumes on intraseasonal upper ocean variability in the Bay of Bengal, *Deep-Sea Research II*, 161, 63-71.

ABSTRACT OF THE DISSERTATION

Physical controls on Southern Ocean biogeochemistry

by

Channing J. Prend

Doctor of Philosophy in Oceanography

University of California San Diego, 2022

Professor Sarah T. Gille, Chair
Professor Lynne D. Talley, Co-Chair

The Southern Ocean plays an outsized role in the global overturning circulation and climate system by transporting mass, heat, and tracers between basins, as well as between the surface and abyssal oceans. Consequently, the Southern Ocean accounts for a disproportionately large percentage of the total oceanic carbon uptake and helps set global nutrient inventories. Therefore, understanding the coupling between physical and biogeochemical processes in this region is crucial to reducing uncertainty in future climate projections. Historically, studying the Southern Ocean has been limited by the paucity of observational data from this remote environment. However, recent advances in autonomous observing technology have provided

unprecedented spatial coverage of subsurface biogeochemical measurements. This thesis uses data from an array of more than 200 autonomous profiling floats—in conjunction with satellite data, numerical models, and theory—to investigate the fundamental question: How do physical processes in the Southern Ocean drive variability of phytoplankton biomass and carbon system parameters? Naturally, the answer to this question will depend on the spatial and temporal scales of interest. Our approach is to consider multiple scales, with the central motivation of better understanding the carbon cycle on climatic timescales.

First, we investigate regional patterns of phytoplankton seasonality in the Southern Ocean (Chapter 2). Results show that enhanced mixing at topographic features contributes to spatial variability in bloom magnitude and timing. Looking to smaller scales, we examine the generation of phytoplankton patchiness by turbulent stirring (Chapter 3). We find that parameterizing eddy transport as an enhanced diffusion requires timescale separation between the physical and biological processes, which raises concerns for the representation of subgrid scale primary productivity in coarse resolution climate models. Next, we turn to air-sea carbon fluxes. We show that carbon outgassing occurs preferentially in the Indo-Pacific sector of the Southern Ocean due to regional differences in the mixed-layer entrainment of upwelled carbon-rich deep water (Chapter 4). Finally, we quantify the relative importance of different frequency bands in driving year-to-year variations of Southern Ocean primary productivity. We find that changes in annual mean phytoplankton biomass are driven by intermittent sub-seasonal events associated with storms and eddies, rather than low frequency climate variability (Chapter 5). Together, these chapters use a novel combination of in situ measurements, satellite data, and model output to elucidate physical mechanisms that control Southern Ocean biogeochemistry. Understanding these drivers is necessary to improve climate models and predict the response of the ocean to climate change.

Chapter 1

Introduction

The ocean is characterized by motions across a wide range of scales, from the planetary to the planktonic (Talley, 2011). Moreover, these disparate scales all interact, which makes oceanography challenging (and exciting!) from both an observational and modeling perspective. Ocean circulation exerts significant control over biogeochemical processes, which are similarly multi-scale in nature. For example, at the global and basin scales, the meridional overturning circulation (MOC) controls subsurface nutrient and carbon inventories, which in turn influence large-scale and mean patterns in primary production and air-sea carbon flux (Rintoul & Wunsch, 1991; Ganachaud & Wunsch, 2002; Landschützer et al., 2015). On shorter timescales, phytoplankton biomass and carbon system parameters have been observed to be closely linked to synoptic storms, as well as oceanic mesoscale and submesoscale variability (Carranza & Gille, 2015; McGillicuddy, 2016; Lévy et al., 2018; Nicholson et al., 2022). This dissertation aims to address the coupling between physical and biogeochemical processes at several different scales in the Southern Ocean, which surrounds Antarctica.

The Southern Ocean plays a key role in the MOC due to its unique circulation (Gruber et al., 2009; Talley, 2013; Tamsitt et al., 2017). The lack of continental boundaries permits the formation of the Antarctic Circumpolar Current (ACC), which circles the globe on an unbroken path around Antarctica (Firing et al., 1982, 2011). Accordingly, the ACC is a conduit for inter-basin exchange as well as the transfer of fluid between the surface and deep oceans (J. Marshall

& Speer, 2012; Talley, 2013). The importance of the Southern Ocean to global biogeochemical cycles stems from its central place within the MOC (Figure 1.1). In the northern ACC, formation of intermediate and mode waters is linked to global nutrient distributions and subduction of anthropogenic carbon (Sarmiento et al., 2004; Sallée et al., 2012; Bopp et al., 2015). While in the southern ACC, upwelling of carbon-rich deep waters drives CO_2 outgassing (Lovenduski et al., 2008; Gruber et al., 2019). Therefore, processes in the Southern Ocean have a particularly large influence on the global climate system.

Studying the Southern Ocean, especially from observations, is made difficult by its remote location and harsh weather. To ameliorate the paucity of in situ data in the region, the Southern Ocean Carbon and Climate Observations and Modeling (SOCCOM) project began deploying autonomous biogeochemical profiling floats in 2014 (Talley et al., 2019). Today, more than 200 floats have been deployed (Figure 1.2), providing an influx of new observations, many from places with no historical measurements. Here, we use this novel dataset to investigate physical controls on Southern Ocean biogeochemistry, including biophysical interactions and patterns of air-sea carbon exchange.

The thesis is divided into four main chapters. Chapter 2 examines phytoplankton bloom initiation in the Scotia Sea, which is home to the earliest and largest offshore spring bloom in the Southern Ocean. We find that the early bloom timing is linked to shallow mixed-layer depths. This unique stratification is related to lateral advection of cold shelf waters from the Weddell Sea, which sink below the surface waters in the Scotia Sea and inhibit deep winter mixing. We also show that the precise bloom location is tied to the local bathymetry. Namely, vertical transport associated with stratified Taylor column dynamics enhances productivity by supplying subsurface iron to the euphotic zone.

Chapter 3 is a theoretical investigation of eddy transport of biogeochemical tracers. Primary productivity is known to be influenced by oceanic mesoscale and submesoscale processes (McGillicuddy, 2016; Lévy et al., 2018). This is evident from satellite images of ocean color, which clearly show the expression of eddies and other small-scale structures in the flow. It has

been suggested that accounting for (sub-)mesoscale productivity is necessary to close global budgets (Lévy & Martin, 2013). This poses a problem for climate models, which rarely resolve processes smaller than the mesoscale. Therefore, the fluxes of tracers—such as nutrients and phytoplankton—associated with the unresolved dynamics must by parameterized. It is common to assume that the eddy fluxes of any arbitrary tracer are proportional to the gradients in the mean field, the so-called gradient diffusion hypothesis. In this study, we show that the validity of this approximation relies on separation between the biological and physical timescales. However, this scale separation condition is violated for biological processes at the submesoscale, which can help explain biases in climate models.

Turning to the carbon cycle, Chapter 4 characterizes spatial patterns in mean Southern Ocean air-sea carbon fluxes. Using float-based carbon flux estimates, we show that CO_2 outgassing occurs preferentially in the Indo-Pacific sector of the ACC. This zonal asymmetry is driven by systematic inter-basin variations in the mixed-layer entrainment of carbon-rich deep water. Therefore, the long-term Southern Ocean carbon sink variability inferred from sparse shipboard data may be influenced by the fraction of measurements from each basin in a given year. Furthermore, it is necessary to sample these different air-sea flux regimes in order to monitor future changes in oceanic carbon release and uptake.

Finally, Chapter 5 examines year-to-year variations of annual mean chlorophyll in the Southern Ocean. These changes have traditionally been attributed to low-frequency climate variability, however we show that non-seasonal chlorophyll fluctuations are not well correlated with the Southern Annular Mode (SAM). This is because non-seasonal variability is dominated by intermittent events associated with sub-seasonal forcing such as storms and eddies. Low frequency chlorophyll fluctuations are correlated with the SAM, but only account for about 10% of the total variance. Across most of the ACC, the annual mean chlorophyll value is determined by the cumulative effect of high frequency chlorophyll variability. Consequently, the spatial scales associated with consistent variations in the annual mean are small ($\sim$ 250 km).

These four chapters use a range of tools to explore a diverse set of processes and scales.

Chapter 2 focuses on regional patterns in phytoplankton seasonality, and utilizes autonomous float measurements, satellite ocean color data, and model output. Chapter 3 uses theory and idealized simulations to analyze biophysical interactions at eddy scales. Chapter 4 looks at basin-scale differences in mean air-sea carbon fluxes using profiling float data in combination with reanalysis and observation-based data products. Finally, Chapter 5 considers the relative importance of sub-seasonal, seasonal, and multi-annual chlorophyll fluctuations from satellite and float data. Altogether, these chapters contribute to a better understanding of Southern Ocean dynamics and biogeochemistry. Given the unique role that this region plays in the global climate system, investigating these questions is crucial to help society plan for the effects of climate change.

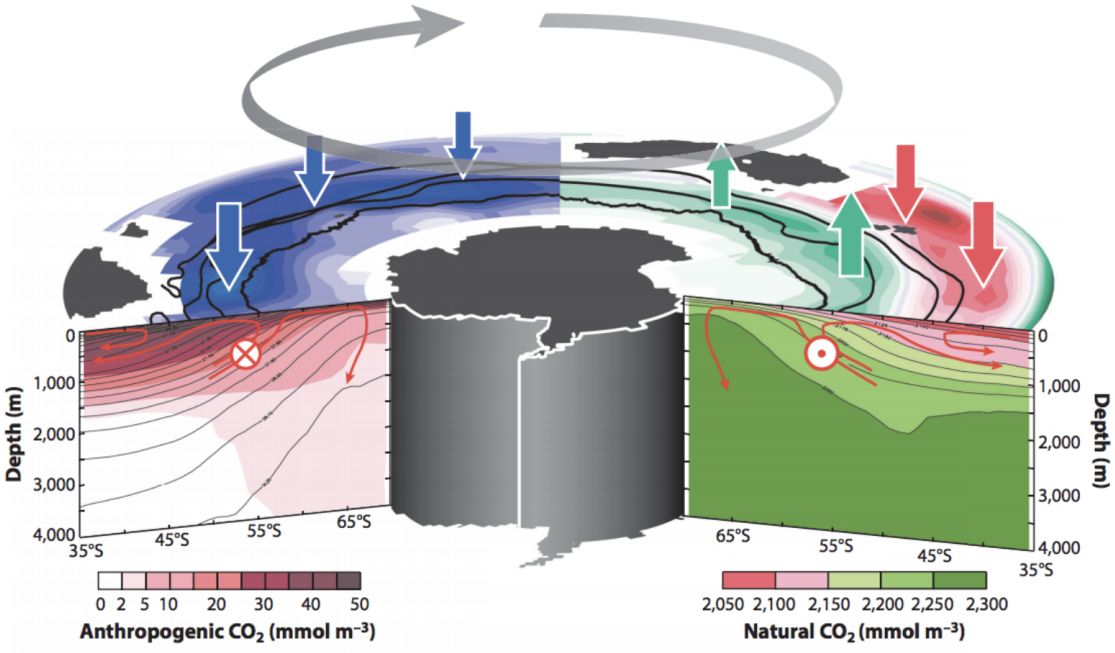

Figure 1.1. Schematic diagram of the zonal mean overturning circulation of the Southern Ocean and the associated fluxes of anthropogenic (left) and natural (right) CO_2 based on the ocean inversion estimates of Gruber et al. (2009). Figure reproduced from Gruber et al. (2019).

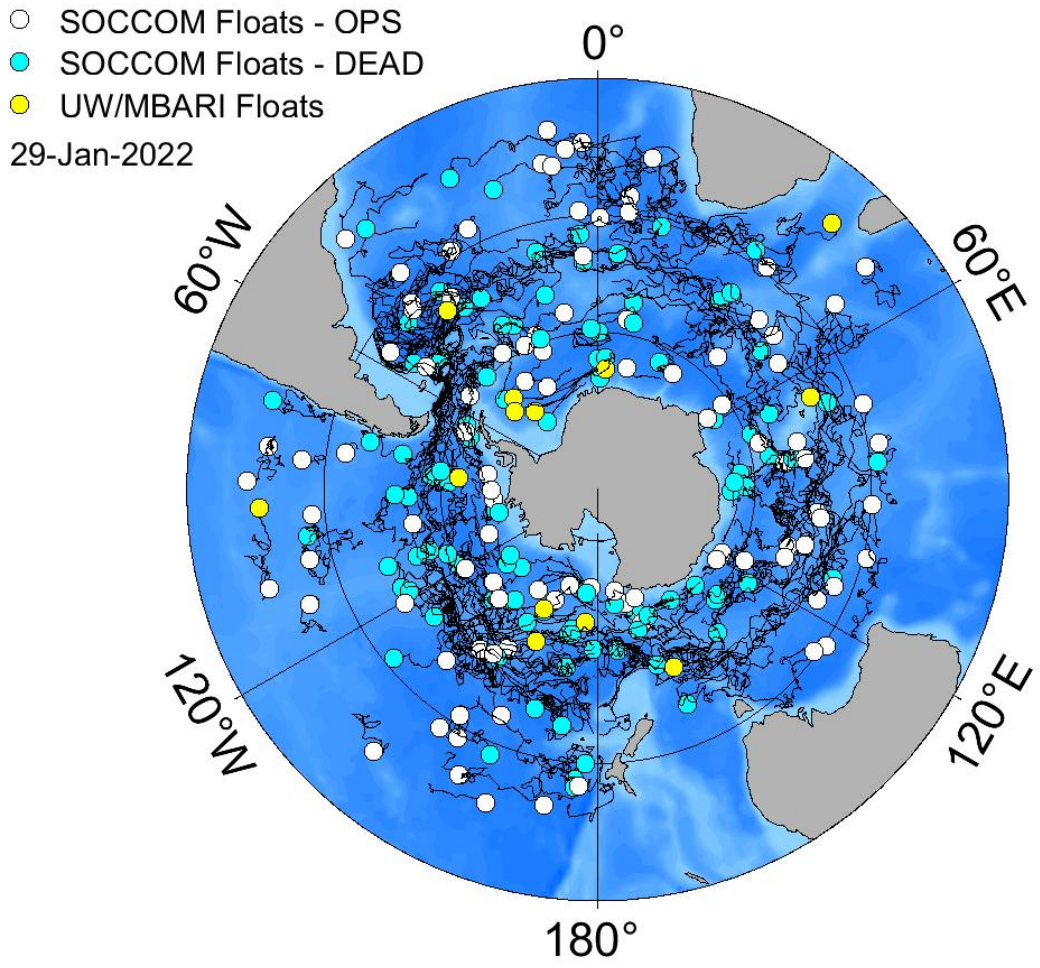

Figure 1.2. Distribution of SOCCOM floats as of January 29, 2022. Figure reproduced from the SOCCOM Map Room.

Chapter 2

Physical drivers of phytoplankton bloom initiation in the Scotia Sea

Abstract

The Scotia Sea is the site of one of the largest spring phytoplankton blooms in the Southern Ocean. Past studies suggest that shelf-iron inputs are responsible for the high productivity in this region, but the physical mechanisms that initiate and sustain the bloom are not well understood. Analysis of profiling float data from 2002 to 2017 shows that the Scotia Sea has an unusually shallow mixed-layer depth during the transition from winter to spring, allowing the region to support a bloom earlier in the season than elsewhere in the Antarctic Circumpolar Current. We compare these results to the mixed-layer depth in the 1/6° data-assimilating Southern Ocean State Estimate (SOSE) and then use SOSE to assess the physical balances governing mixed-layer variability in the region. Results indicate the importance of lateral advection of Weddell Sea surface waters in setting the stratification. A Lagrangian particle release experiment run backward in time suggests that Weddell outflow constitutes 10% of the waters in the upper 200 m of the water column in the bloom region. This dense Weddell water subducts below the surface waters in the Scotia Sea, establishing a sharp subsurface density contrast that cannot be overcome by wintertime convection. Profiling float trajectories are consistent with the formation of Taylor columns over the region's complex bathymetry, which may also contribute to the unique stratification. Furthermore, biogeochemical measurements from 2016 and 2017 bloom

events suggest that vertical exchange associated with this Taylor column enhances productivity by delivering nutrients to the euphotic zone.

2.1 Introduction

The Southern Ocean is typically classified as a high nutrient low chlorophyll environment (HNLC), with phytoplankton growth limited by iron and light (Mitchell et al., 1991; de Baar et al., 1995). The major sources of iron to the Southern Ocean, including shelf sediments, dust deposition, and glacial ice, are highly spatially variable (Lacelot et al., 2009; a. S. J.-B. Tagliabue A. et al., 2014). Satellite data and in situ measurements show that primary productivity in the Antarctic Circumpolar Current (ACC) is also heterogeneous (Sullivan et al., 1993; Sokolov & Rintoul, 2007; Arrigo et al., 2008). Offshore blooms in the Scotia Sea, far north of the sea ice edge, are sustained for the full austral summer and support nearly half the total circumpolar stock of Antarctic krill (Atkinson et al., 2004; Tarling et al., 2012). Blooms here are triggered particularly early in the season (August-September) compared to other open ocean blooms in the ACC (Holm-Hansen et al., 2004; Murphy et al., 2004), and peak by October-November, when blooms in other parts of the ACC are just being initiated (Blain et al., 2007; Mongin et al., 2008). This is evident in the October satellite chlorophyll climatology (Figure 2.1), which shows high chlorophyll in the Scotia Sea (outlined in magenta) while the rest of the Southern Ocean remains low. Therefore, the mechanisms driving bloom initiation in the Scotia Sea have implications for the distribution of Antarctic megafauna as well as carbon export to the ocean interior via the biological pump (Hofmann et al., 1998; Murphy et al., 2004, 2007).

There are two distinct blooms in the Scotia Sea visible in Figure 2.1b, a northern bloom located between the Polar Front (PF) and the Southern ACC Front (SACCF) around 51°S and a southern bloom located between the SACCF and the ACC Southern Boundary (SB) around 59°S. The northern bloom has been linked to iron inputs from the South Georgia Islands (Atkinson et al., 2001; Ward et al., 2002). The southern bloom, which is the focus of this study, has different

dynamics since it is not associated with an island wake. Instead, iron fluxes from the Antarctic Peninsula have been suggested to support the high productivity in this region (Dulaiova et al., 2009; de Jong et al., 2012; Frants et al., 2013; Hatta et al., 2013). A detailed iron budget of the southern Scotia Sea from a regional coupled physical-biogeochemical model shows that shelf-derived iron can meet most of the demand by the phytoplankton in the region, with minimal contributions from dust, icebergs, and other sources (Jiang et al., 2019). The off-shelf transport of iron-rich waters to the bloom region primarily occurs below the mixed-layer and involves multiple processes related to the ACC frontal jets (Frants et al., 2013; Measures et al., 2013; Zhou et al., 2013). For example, horizontal advection and entrainment of shelf waters by the SB were both found to influence iron concentrations in southern Drake Passage (Frants et al., 2013; Measures et al., 2013; Zhou et al., 2013). Further downstream in the Weddell-Scotia confluence, cross-frontal eddy activity at the SACCF was shown to transport nutrients that support phytoplankton growth (Kahru et al., 2007).

The advective pathways hypothesized to deliver iron to the southern Scotia Sea have been examined explicitly using surface drifters (A. F. Thompson & Youngs, 2013; Youngs et al., 2015) and particle release experiments in a coupled sea ice-ocean model (Renner et al., 2012). Results support the connection between high Scotia Sea productivity and water properties off the eastern Antarctic Peninsula. These studies have identified how iron, which supports phytoplankton growth through the full austral summer, is transported from the shelf to the bloom region. However, the mechanisms of bloom initiation are still not well understood. Classical theory, known as the critical depth hypothesis, explains spring blooms through shoaling of the mixed-layer above a critical depth where vertically integrated phytoplankton growth and losses are equal (Sverdrup, 1953). More recently, Sverdrup's critical depth hypothesis has been questioned for several reasons including its failure to distinguish between the hydrographically defined mixed layer and the actively turbulent layer (Behrenfeld, 2010; J. R. Taylor & Ferrari, 2011; Franks, 2015; Carranza et al., 2018). Still, despite the limitations of the critical depth hypothesis, mixed-layer depth (MLD) has been shown to be closely linked to primary productivity

in the Southern Ocean (Mitchell & Holm-Hansen, 1991; Mitchell et al., 1991; Fragoso & Smith, 2012; Carvalho et al., 2017).

In this study, we use float profiles and the eddy-permitting Southern Ocean State Estimate (SOSE) to assess the importance of MLD and other physical factors in initiating and sustaining the southern Scotia Sea bloom. We consider both the climatological hydrographic properties that allow the region to consistently support an early spring bloom as well as the processes that trigger individual bloom events and supply shelf-sourced iron to the euphotic zone. First, we show that year-round shallow mixed layers in the Scotia Sea provide unique conditions conducive to early spring bloom formation. Then we demonstrate the importance of Weddell-Scotia surface exchange in setting this stratification. Finally, we examine spring bloom events in 2016 and 2017 using biogeochemical float data, which allow us to relate changes in bio-optical properties directly to their physical drivers. These observations suggest that strong currents impinging on a seamount in the bloom region support the formation of Taylor columns, which are vertical rotating cylinders of fluid that form when a flow encounters an obstacle (G. I. Taylor, 1923). The anticyclonic circulation, counterclockwise in the Southern Hemisphere, and vertical mixing associated with this flow feature are suggested to enhance productivity by providing phytoplankton access to subsurface iron that is advected from the Antarctic Peninsula.

2.2 Data and Methods

2.2.1 Profiling Float Data

This study uses hydrographic profiles from floats deployed by both the Argo and the Southern Ocean Carbon and Climate Observations and Modeling (SOCCOM) programs. Argo is a global array currently consisting of more than 3,900 autonomous floats that collect temperature and salinity profiles over the top 2,000 m of the water column every 10 days. These data are made freely available by the International Argo Program and the national programs that contribute to it (http://www.argo.ucsd.edu, http://argo.jcommops.org). We analyze 15,615 profiles collected

in the Scotia Sea and surrounding area (48-66°S, 30-76°W) from 2002 to 2017 (Figure 2.3). The delayed-mode quality-controlled data are used and profiles are interpolated onto a regular depth axis with 5 m vertical resolution. Profiles are binned into different geographic regions based on the mean location of the ACC fronts (Figure 2.3a). Zonal boundaries of the grid boxes are defined by mean dynamic height contours corresponding to the Subantarctic Front (SAF), PF, and SACCF from Swart et al. (2008). Constant, evenly spaced meridional boundaries were selected in order to fully contain the chlorophyll peak associated with the bloom in the red starred box. The number of profiles in each grid box by month is shown in Figure 2.3b. The analysis was repeated with several grids in order to test the sensitivity of the results. We varied the longitudinal boundaries of the boxes and the definition of the ACC frontal positions, using isolines of mean dynamic topography based on Sokolov and Rintoul (2009). The analysis was also conducted using a grid of rectangular boxes defined by latitude and longitude only; however, we present results where the grid is based on the ACC fronts as this makes more dynamical sense given the importance of frontal jets in mediating the regional transport.

For each profile, the mixed-layer depth is calculated based on the density criterion following de Boyer Montégut et al. (2004) and using a threshold value of $\Delta\sigma_\theta = 0.03$ kg m^{-3} (Dong et al., 2008). Buoyancy frequency (N^2), a measure of the stratification, is found from the density profiles using the Gibbs seawater package routine (http://www.teos-10.org), which has been validated extensively (e.g. King et al., 2012). This routine calculates N^2 from the difference in potential density between two seawater parcels, $\Delta\rho^\Theta$, separated by a small vertical distance Δz, with the reference pressure taken as the mid-point between the two parcels. This is expressed as

$$N^2 = \frac{g}{\rho}\frac{\Delta\rho^\Theta}{\Delta z}, \tag{2.1}$$

where g is gravitational acceleration, and ρ is the density evaluated at the mid-pressure level. As discussed in King et al. (2012), salinity measurement noise dominates over noise in temperature when calculating buoyancy frequency from CTD data, which can lead to wiggly N^2 profiles.

Therefore, N^2 profiles are smoothed using a 10 m vertical running average as in Graff and Behrenfeld (2018).

SOCCOM is a regional array comprising about 125 autonomous Argo-equivalent floats in the Southern Ocean. In addition to collecting temperature and salinity profiles over the top 2,000 m of the water column, the floats also measure dissolved oxygen, nitrate, pH, fluorescence and backscatter. The data are made freely available by the SOCCOM Project (http://soccom.princeton.edu). The quality-controlled data from the June 7, 2018 SOCCOM snapshot are used in this analysis (http://doi.org/10.17882/42182#58015). In Section 1.3.3 we consider chlorophyll-*a* (chl-*a*) profiles calculated from fluorescence for 2 floats that passed through the southern Scotia Sea during early spring in 2016 and 2017, respectively. Data processing and corrections applied to the chl-*a* fluorometer raw data are described in Johnson et al. (2017a). In order to assess the physical factors responsible for triggering bloom events, we compute MLD and euphotic zone depth (Z_e). As for the Argo floats, MLD is calculated using a density threshold of 0.03 kg m^{-3}. The floats do not directly measure irradiance, so Z_e is calculated from the normalized relationship between euphotic zone depth and chlorophyll column inventory as defined in Morel and Maritorena (2001):

$$\begin{aligned} Z_e &= 912.5\,[\mathrm{Chl_{tot}}]^{-0.839} \quad 10\text{ m} < Z_e < 102\text{ m}, \\ Z_e &= 426.3\,[\mathrm{Chl_{tot}}]^{-0.547} \quad 102\text{ m} < Z_e < 180\text{ m}, \end{aligned} \tag{2.2}$$

where $[\mathrm{Chl_{tot}}]$ is the total chl-*a* concentration vertically integrated over the float profile, which is related to the euphotic zone depth by two possible cases depending on the calculated value of Z_e.

2.2.2 Additional Data

The study also makes use of the 2002-2017 Moderate-Resolution Imaging Spectroradiometer (MODIS) Aqua monthly chlorophyll and photosynthetically available radiation (PAR) climatologies, as well as 8-day MODIS chl-*a* data from spring 2016 and 2017. For both the monthly and the 8-day fields, the Level 3 binned data at 9 km resolution are used.

The AVISO combined mean dynamic topography product for 1993-2012 on a 1/4° × 1/4° grid (http://www.aviso.altimetry.fr/) is used to define the mean ACC frontal positions following Swart et al. (2008) and Sokolov and Rintoul (2009). These fronts are used to define a grid for binning float data as described in Section 2.2.1. We note that there is considerable temporal variability in frontal positions, and sea surface height (SSH) undergoes an annual cycle associated with steric heating and cooling of the ocean. However, our results suggest shallow spring MLDs in the southern Scotia Sea regardless of how the grid is defined and thus mean frontal positions are used for simplicity. This is further discussed in Section 2.3.1. NOAA/NSIDC Climate Data Record of monthly passive microwave sea ice concentration is used to plot the sea ice edge (Version 3 on a 25 km × 25 km grid; https://nsidc.org/data/G02202). Bathymetry from the ETOPO1 1 arc-minute global relief model (Amante & Eakins, 2009) is plotted in several figures and is available online (https://www.ngdc.noaa.gov/mgg/global/). November 2016 surface drifter trajectories from the Global Drifter Program (http://www.aoml.noaa. gov/phod/gdp/index.php) are used to investigate downstream advection of chlorophyll in Section 2.3.3. To this end, we also examine the 1/4° × 1/4° drifter-derived monthly climatology of global near-surface currents (Laurindo et al., 2017). Version 3.03 is used, which is based on data from February 1979 up to July 2018 (http://www.aoml.noaa.gov/phod/gdp/mean_velocity.php).

2.2.3 Southern Ocean State Estimate

The Southern Ocean State Estimate (SOSE) is an eddy-permitting, data assimilative model that uses ocean observations to constrain the MITgcm solution (Mazloff et al., 2010). The configuration used in this analysis has 1/6° horizontal resolution, 42 uneven vertical levels, and runs from January 1, 2005 to December 31, 2010. A full description of the observational constraints is provided in Mazloff et al. (2010), which includes shipboard CTD measurements, Argo float profiles, and instrument-mounted elephant seal profiles. This iteration of the model has been extensively validated (Cerovečki et al., 2011; Cerovečki & Mazloff, 2015; Abernathey et al., 2016) and is publicly available (http://sose.ucsd.edu). In Section 2.3.1, SOSE state variables

are used to calculate buoyancy frequency and MLD. In Section 2.3.2, the bloom region heat and salt budgets are computed from SOSE output to examine the drivers of mixed-layer variability. SOSE diagnoses heat and salt budget terms at each grid point from the model state and outputs them as 5-day averages. The heat budget is computed following Tamsitt et al. (2016), where the temperature evolution is given by the sum of the air-sea heat flux, advective heat transport (separated into geostrophic and ageostrophic components), and three-dimensional diffusive processes:

$$\frac{\partial T}{\partial t} = \frac{Q(z)}{\rho c_p dz} - \mathbf{u}_g \cdot \nabla T - \mathbf{u}_a \cdot \nabla T + \kappa_H \nabla_H^2 T + \kappa_z \frac{\partial^2 T}{\partial z^2} + K_T^{turb}, \tag{2.3}$$

where $\partial T/\partial t$ is the temperature tendency, Q is the net air-sea heat flux, c_p is the specific heat capacity of seawater, dz is the depth in the model over which Q is distributed, $\mathbf{u}_g$ and $\mathbf{u}_a$ are the geostrophic and ageostrophic horizontal velocities, ∇ is the divergence operator, κ_H and κ_v are the horizontal and vertical diffusivities, and K_T^{turb} is the K-profile parameterization (KPP) turbulent vertical diffusion term (Large et al., 1994). As in Tamsitt et al. (2016), geostrophic velocities are calculated from the model hydrostatic pressure, and ageostrophic velocities are taken to be the residual between the model velocity and calculated geostrophic velocity.

The salt budget can be expressed in a similar way, as described by Cerovečki et al. (2019). The key difference from the heat budget is the surface flux term, which is determined by the net effects of evaporation, precipitation, runoff, and freshwater forcing by sea ice processes. The full salt budget is:

$$\frac{\partial S}{\partial t} = \frac{S}{dz}(E - P - R - IO) - \mathbf{u}_g \cdot \nabla S - \mathbf{u}_a \cdot \nabla S + \kappa_H \nabla_H^2 S + \kappa_z \frac{\partial^2 S}{\partial z^2} + K_S^{turb}, \tag{2.4}$$

where $\partial S/\partial t$ is the salinity tendency, E is evaporation, P is precipitation, R is runoff, and IO is the freshwater forcing by sea ice processes. Advection and diffusion terms are defined as in the heat budget but computed using the divergence of salinity rather than temperature.

Also, SOSE daily velocity fields are used to calculate offline Lagrangian particle tra-

jectories using the particle-tracking model Octopus, which is available online. Details of the interpolation scheme have been described by van Sebille et al. (2018) and by Tamsitt et al. (2017, 2018). For the purposes of this study, we seed particles in the southern Scotia Sea and then run trajectories backwards in time by using reversed velocities. This is done in order to determine the bloom region source waters and their relative fractions. In particular, particles were released at three SOSE vertical levels (150, 177.5, and 208.5 m depth) in a rectangular box (evenly spaced horizontally) enclosing the bloom site with boundaries 57.5°-59°S, 43°-47°W (outlined in black in Figure 2.5). This depth range was chosen as it is below the average MLD in the region and roughly the depth at which shelf-sourced iron is advected to the Scotia Sea (150-200 m) (Frants et al., 2013). Particles were run backward in time for a period of 9 months, which was found to be the approximate time necessary for the Lagrangian particles to be advected from the Weddell Sea to the bloom region. In total, 120,000 particles were released in 12 separate runs beginning on the first day of every month in 2010. The runs were partitioned in order to use SOSE velocity fields from different 9-month periods in an attempt to account for any seasonal variability that may impact particle pathways.

2.3 Results

2.3.1 Regional Mixed-Layer Variability

A unique aspect of the southern Scotia Sea bloom is how early in the season it occurs compared to other open ocean blooms in the ACC. Here, bloom events are typically triggered in mid-August to September and peak by November (Murphy et al., 2004; Hewes et al., 2008), whereas blooms in other parts of the ACC are triggered in late October to November (Blain et al., 2007; Mongin et al., 2008). To investigate why bloom initiation is so early in the Scotia Sea, we first examine the physical conditions in the region during early spring. A useful diagnostic to consider is the buoyancy frequency, N^2, which is a measure of the water column stability. Higher N^2 values indicate stronger stratification, which inhibits vertical mixing of the phytoplankton

and thus aids biomass accumulation necessary to bloom development (Brody & Lozier, 2015). The map in Figure 2.2a shows the SOSE subsurface N^2 maximum during the early austral spring period, defined as August 15 to September 15 (composite of all years in the SOSE run). This is compared to Figure 2.2b, which gives the subsurface N^2 maximum calculated at individual Argo profiles from August 15 to September 15 during the SOSE period (2005-2010). The overall spatial pattern of buoyancy frequency is consistent between SOSE and Argo, with higher N^2 values between the PF and SACCF. Note though that 2005-2010 Argo data are assimilated into SOSE. While it may not be particularly surprising then that SOSE shows similar patterns in MLD, it is necessary to establish this fact in order to justify the usefulness of using SOSE to assess the mixed-layer heat and salt budgets in the following section of the paper. Overall, the bloom region has a relatively high buoyancy frequency, signifying a more stably stratified water column that is favorable to bloom development. However, the values are comparable to other locations along the SACCF.

The bloom region is more distinctive when we consider the depth in the water column where the subsurface N^2 maximum occurs, which has been shown to be an ecologically relevant depth corresponding to phytoplankton vertical distribution (Carvalho et al., 2017). This is plotted for SOSE in Figure 2.2c and for individual Argo profiles in Figure 2.2d. Based on the definition of the buoyancy frequency (Equation 2.1), this is the depth with the maximum vertical density gradient, which is similar to the hydrographically defined MLD in many cases. In general, Figures 2.2c and 2.2d show that smaller values of N^2 correspond to deeper N^2 maxima. Compared to other locations, the N^2 maxima in the bloom region occur at shallower depths in the water column. This is particularly apparent in Figure 2.2d if one considers the patch of shallower maximum N^2 depth values between 42°W and 50°W south of the SACCF (red boxes in Figure 2.2c and 2.2d), which corresponds to shallower MLD as well. Overall, the spatial distribution of MLD is similar in structure to Figure 2.2c and 2.2d. In other words, the southern Scotia Sea seems to have a shallower MLD than nearby regions during the bloom initiation period. This is consistent with the classical explanation for spring phytoplankton blooms, which suggests that

shallow mixed layers facilitate rapid bloom development by providing phytoplankton with more access to light and nutrients (Sverdrup, 1953).

To further characterize regional MLD, we bin Argo profiles from the Scotia Sea and surrounding area (48-66°S, 30-76°W) into a grid based on the mean location of the ACC frontal positions and compute a monthly climatology of MLD for all 12 boxes. This is shown in Figure 3c based on Argo profiles (top panel) as well as SOSE (bottom panel). Both Argo and SOSE show that the red starred box (bloom region) has a markedly shallow MLD during the bloom initiation period of August and September (highlighted in gray in Figure 2.3c). This stratification allows the southern Scotia Sea to support phytoplankton growth earlier in the season, since a bloom can occur as soon as spring light levels increase. Results consistently showed shallow MLD in the bloom region, regardless of the choice of grid (not shown). However, the seasonal cycle in the bloom region is not statistically different at the 95% confidence level from the other two regions south of the SACCF (different shades of red in Figure 2.3a). Therefore, MLD alone cannot explain why the bloom occurs at this particular location. Furthermore, how are nutrients supplied to the euphotic zone in the absence of wintertime MLD deepening? These questions are investigated after first examining why the regions south of the SACCF have a shallow year-round MLD.

2.3.2 Weddell-Scotia Surface Exchange

Comparatively shallow MLDs in the southern Scotia Sea allow the region to support an early spring bloom. Here, we assess the physical balances that govern upper-ocean variability in the region. Figure 2.4 shows the 2005-2010 mean SOSE heat and salt budget. The temperature tendency (black in Figure 2.4a) is driven mainly by surface heat fluxes (purple in Figure 2.4a) and geostrophic advection (green in Figure 2.4a). Air-sea heat flux follows the expected seasonal cycle with positive values in summer (i.e. heat entering the ocean) and negative values in winter (heat leaving the ocean. Horizontal geostrophic advection acts to cool the mixed-layer during most of the year. This is consistent with the transport of cold Weddell water to the Scotia Sea,

which has been observed from drifter data (A. F. Thompson & Youngs, 2013; Youngs et al., 2015). Geostrophic advection is also an important driver of the salinity tendency (black in Figure 2.4b). Next, we examine the role of Weddell outflow in setting the bloom region stratification. This influence, for example, could be due to the stratifying effects of freshwater from ice melt. Another possibility is that the Weddell water, which is cold and dense, subducts below the surface waters in the bloom region and creates a stable floor to the base of the mixed layer. These hypotheses are explored through a Lagrangian particle release experiment.

Of the 120,000 particles seeded in the southern Scotia Sea and run backward in time, 100 randomly selected trajectories are plotted in Figure 2.5. In the forthcoming discussion, "initial position" refers to the particle's location away from the bloom region after being run backwards in time for 9 months. Similarly, "final position" refers to the location in the bloom region where the particle was seeded. One can see qualitatively that most of the water in the top 200 m of the bloom region comes from the ACC, with a small fraction originating in the Weddell. Based on all the trajectories, this fraction is equal to 10%, which is quantified by finding the number of particles with an initial position east of 57°W. To test the sensitivity of our results, smaller runs were also conducted using velocity fields from 9-month periods in other years of the SOSE run; SOSE spans only 6 years, so large-scale climate variability is not captured. While precise pathways and rates varied slightly, results regarding the fraction of Weddell-sourced waters in the bloom region were consistent.

Figure 2.6a shows two particular trajectories that were selected to illustrate the major pathways taken by waters to reach the upper 200 m of the bloom region. The orange trajectory represents the 90% of total particles that originate upstream in the ACC, while the blue trajectory represents the 10% of total particles that are advected from the Weddell Sea. These trajectories are then mapped in θ-S space (Figure 2.6b). The Weddell particle is colder and saltier at its initial position (marked by a blue triangle) than it is once it reaches the bloom region (blue square). Furthermore, the particle is initially near the surface and then increases its depth along the trajectory. On average, Weddell-sourced particles increase their depth by 104 m while traveling

to the bloom region. This supports the hypothesis that Weddell water subducts below the surface waters in the ACC, stabilizing the mixed-layer in the bloom region. The ACC particle on the other hand, starts out warmer and lighter (orange triangle) compared to its final position (orange square), and its depth varies much less along the trajectory (standard deviation of 11 m).

To demonstrate that these two particles are representative of the two source waters to the bloom region, we use θ and salinity from the initial positions of all trajectories to calculate a joint probability density function (pdf; Figure 2.7). A red square marks the average θ-S properties of particles at their final location in the Scotia Sea. Figure 2.7 shows two distinct source waters: a broadly defined water mass centered close to the initial position of the ACC particle in Figure 2.6b, and a smaller peak near the initial Weddell particle position in Figure 2.6b. In general, the ACC source water is warmer and lighter than the particle's final θ and salinity (red square), consistent with modification by the 10% of the colder and denser Weddell water.

Given that we have two distinct source waters, along with estimates of their average θ-S properties and relative fractions, it is tempting to add them together in an informal Optimum Multiparameter-type (OMP) analysis (Tomczak & Large, 1989). OMP is an inverse modeling technique that describes observed water properties at a particular location as a mixture of several different source waters. Following this framework, one could take a weighted sum of the two source waters identified from the joint pdf. Doing so certainly shifts the ACC source water closer to the bloom region θ and salinity. However, the OMP method assumes that advection moves water along isopycnals, and Figure 2.6b clearly shows that particle pathways are not strictly adiabatic. While the cold Weddell water likely plays a role in setting the bloom region θ-S properties, some diabatic processes are also necessary along the particle trajectories. This may be due to mixing over the region's rough topography, which has been observed in the Ona Basin, for example (Barré et al., 2008). In the case of the Weddell particles, which are initially near the surface, modification by air-sea fluxes and sea ice processes along the particle pathways is also possible.

2.3.3 Individual Bloom Events

Thus far, we have considered the climatological conditions in the Scotia Sea based on several years of data and SOSE output. In this section we examine 2016 and 2017 bloom events as measured by SOCCOM floats WMO 5904660 and 5904984, respectively. Float 5904660 entered the southern Scotia Sea from the west on September 3, 2016. Starting on September 23, chl-*a* increased rapidly before peaking in early November (see Figure 2.8c). MODIS satellite chlorophyll data from this period confirm that the high chl-*a* measured by the float was the signature of a large-scale bloom (not shown). The MLD (purple) and Z_e (black) deepen just before the bloom begins. Thus, while the stratification in the Scotia Sea makes the region a good candidate for an early spring bloom, mixed-layer shoaling is not necessarily responsible for triggering individual bloom events. What did trigger the bloom then? Increasing spring light levels, as indicated by Z_e deepening, are likely important. We also note that high chlorophyll corresponds to the 5-month period when the float was trapped in an anticyclonic flow over a topographic feature called Pine Bank (Figure 2.8b). Furthermore, the drop in chl-*a* after March 7, 2017 occurred when the float escaped from the rise.

Similarly, high chl-*a* was measured by float 5904984 when it was trapped in an anticyclonic circulation over Pine Bank during the 2017-2018 bloom cycle (Figure 2.8d). The abrupt drop in chl-*a* after March 25, 2018 coincided with the float's escape from the seamount. This indicates that the bathymetry and associated circulation may have important biological implications. In addition to the SOCCOM floats discussed here, examination of the Argo database yields 7 other floats from 2005 to 2016 that circled on top of Pine Bank for several months, suggesting that this is a frequent flow feature. Furthermore, the November satellite chlorophyll climatology (Figure 2.9) shows a plume of high chl-*a* extending away from Pine Bank. The plume is consistent with the pathways suggested by the November drifter-derived climatology of global near-surface currents (arrows) as well as individual surface drifter trajectories from November 2016 (magenta), when SOCCOM float data recorded high chlorophyll over Pine Bank.

This implies that advection may also redistribute the chlorophyll produced there across the wider bloom region.

2.4 Discussion

Biogeochemical float data from both 2016 and 2017 showed high chl-*a* corresponding to the floats being trapped in an anticyclonic circulation over Pine Bank. Closed loops in Argo trajectories over seamounts may indicate the presence of Taylor columns (Meredith et al., 2015). Furthermore, Meredith et al. (2015) mapped the locations most likely to form Taylor columns within the Southern Ocean using regional bathymetry with SOSE velocity fields and stratification. The Scotia Sea, including this particular bank, was among the locations identified. Results of Meredith et al. (2015) are based on a simple dimensional analysis described by (1975) (1975). We follow this calculation here to confirm that Taylor columns can occur over Pine Bank. Taylor column formation requires rotational terms in the equations of motion to dominate, so we first compute the Burger number, $B = NH/fL$, which compares stratification and rotation, where N is the Brunt-Väisälä frequency, H is the local depth away from the bathymetric feature, f is the Coriolis parameter, and L is the horizontal length scale of the feature. Using approximate values $N \approx 5.5 \times 10^{-3}$ s^{-1} (computed as the average from the 2002-2017 bloom region Argo data), $H \approx 3500$ m, $f = 1.25 \times 10^{-4}$ s^{-1} and $L \approx 150$ km, yields $B \approx 1$. Then, we calculate the Rossby number, $Ro = U/fL$, which compares the inertial and rotation terms in the equation of motion, where U is the horizontal velocity scale. For $U \approx 0.2$ m/s (from SOSE velocity fields), and f and L given above, $Ro \approx 0.01$. Finally, we can compute the critical height (h_0/Ro) from the scaled height of the bathymetric feature $h_0 = h/H$, where h is the height of the rise. With $h \approx 1700$ m and H given above, $h_0 \approx 0.49$, which gives a critical height of $h_0/Ro \approx 49$. This value is an order of magnitude larger than the critical value of $\sim$1.3-2 found by Huppert (1975; see their Figure 3, for $B \approx 1$). This indicates that the geometry of Pine Bank favors Taylor column formation, and confirms the results from Meredith et al. (2015).

The role of Taylor columns in enhancing productivity has been recognized at other locations including Cobb seamount in the North Pacific (Dower et al., 1992) and the Prince Edward Plateau in the Indian sector of the Southern Ocean (Perissinotto & Duncombe Rae, 1990). These studies proposed several mechanisms for how Taylor columns impact biological production including buildup of nutrients due to recirculation and retention of local waters, and increased stability of the surface mixed-layer. Both of these processes may be at play in the southern Scotia Sea. Isopycnals often dome in a Taylor column, causing shoaling of the mixed-layer base as was observed at Bruce and Discovery Banks (downstream of Pine Bank) by Meredith et al. (2015). Iron delivery to the euphotic zone via vertical exchanges is also likely important. The off-shelf transport of iron to the Scotia Sea occurs primarily on the $\sigma_\theta = 27.5$ isopycnal (Frants et al., 2013). At the bloom site, downstream of the shelf iron source, the depth of this iron-enriched isopycnal is about 150-200 m during September in SOSE. This may explain why the blooms in 2016 and 2017 were triggered immediately following a deepening of the MLD since phytoplankton would have been able to access the subsurface iron. However, past studies suggest that light limitation is likely more significant than iron limitation for phytoplankton in early spring (Mitchell et al., 1991). Furthermore, MLD varies on timescales shorter than the full bloom cycle, so vertical fluxes of iron across the base of the mixed layer are necessary to sustain the bloom beyond its initial stage.

While the classical Taylor column regime is not associated with vertical velocities, Sévellec et al. (2015) showed theoretically and from moored observations in northern Drake Passage that vertical transports can occur in a stratified Taylor column. This vertical transport compensates for changes in horizontal flow orientation with depth due to stratification (Sévellec et al., 2015). Indeed, SOCCOM profiles of chl-*a*, temperature, salinity and oxygen all indicate vigorous vertical mixing when floats 5904660 and 5904984 came over Pine Bank. This is illustrated by the θ-S diagram of float 5904984 (Figure 2.10). At the point where the float reaches Pine Bank (transition from blues to greens in Figure 2.10), θ-S properties undergo a complete change in character. Temperature, for example, loses both the freezing surface water

and the warmest temperature maximum. We should note that this also corresponds to the crossing of ACC streamlines, and floats may not be sampling the same water mass in progressive profiles. Still, recirculation over Pine Bank retains and mixes waters in the region for months at a time, suggesting that Taylor columns are important to local water mass modification. Furthermore, the recirculation may assist in the transfer of biomass to higher trophic levels, helping explain the region's unusually high abundance of krill, whales, and other megafauna (Hofmann et al., 1998; Atkinson et al., 2004; Murphy et al., 2004, 2007).

In addition to Taylor column effects, the observed mixing over Pine Bank could be related to other flow-topography interactions. For example, diapycnal mixing is typically higher over topographic features due to breaking internal tides, as well as scattering and breaking of remotely generated internal waves. (Polzin et al., 1997; Kunze et al., 2006; Whalen et al., 2012). Submesoscale instabilities in the lee of topography have also been shown to enhance vertical exchange (Rosso et al., 2014, 2015). Observation-based estimates of the diffusivity in the Scotia Sea (Naveira Garabato et al., 2004; Balwada et al., 2016) show mixing rates over rough topography that are two to three magnitudes greater than background values. Furthermore, these high diffusivities extend far above the topography and were shown by Mashayek et al. (2017) to lead to the fast vertical spreading of tracers in a high-resolution ocean model of the Drake Passage region. Another possible explanation for the vertical transports over Pine Bank is upwelling due to Ekman divergence associated with the anticyclonic circulation. Namely, divergence could occur because the northern part of Pine Bank, where winds and surface currents oppose each other, has stronger wind stress; while the southern part of Pine Bank, where winds and currents are aligned, has lower wind stress. In order to better characterize the vertical mixing and its role in driving primary production, a dedicated field campaign including biogeochemical and microstructure measurements would be informative.

2.5 Conclusion

The highly productive southern Scotia Sea bloom system has been the subject of investigation for decades (Hofmann et al., 1998; Holm-Hansen et al., 2004; Murphy et al., 2004; Kahru et al., 2007), yet the mechanisms initiating and sustaining the bloom are not well understood. Using Argo data and SOSE, we show that the climatological mixed-layer in the region is markedly shallow (< 70 m) year-round, which supports early spring bloom formation. We then use SOSE to investigate the processes that set this stratification. Mixed-layer heat and salt budgets indicate the importance of horizontal advection. A backward (in time) particle release experiment is then conducted to determine the source waters that constitute the top 200 m of the water column in the bloom region. We find that 90% of the water comes from upstream in the ACC, while the remaining 10% originates in the Weddell Sea. The Scotia Sea water cannot be defined explicitly as a weighted sum of these two source waters since the particles originating in the Weddell are initially near the surface and therefore subject to significant change through air-sea interaction and sea ice freshwater fluxes. Still, the Weddell outflow is cold and dense enough that it likely modifies the ACC water and contributes to the unique stratification in the bloom region.

While this stratification makes the region prone to early spring bloom development, mixed-layer depth alone cannot explain why the bloom occurs at this particular location since the MLD seasonal cycle in the bloom region is not statistically different from the other regions south of the SACCF. The year-round shallow MLD also raises the question of how nutrients are supplied to the euphotic zone in the absence of winter mixed-layer deepening. Biogeochemical profiling float data suggest that topographic mixing processes are key in determining the bloom location and delivering nutrients to the surface ocean. The highest chl-*a* levels were measured by floats trapped in an anticyclonic circulation over a topographic feature called Pine Bank. Closed loops in float trajectories over seamounts have been shown to indicate the presence of Taylor columns. This is consistent with the results of Meredith et al. (2015), who found that the Scotia Sea, with its complex bathymetry, is one of the regions most likely to form Taylor columns in

the Southern Ocean. Biological impacts of Taylor columns in other locations have been noted in past studies (Perissinotto & Duncombe Rae, 1990; Dower et al., 1992; Meredith et al., 2003). However, this is the first observational evidence of this mechanism in relation to the southern Scotia Sea bloom.

From the limited available data, we cannot unequivocally confirm the existence of a Taylor column or determine if Taylor column formation is necessary to bloom development in this region. Regardless, there is a strong connection between the topography and chlorophyll levels. We propose that the bloom is triggered by increasing spring light levels and then sustained past its initial stages by vertical transports associated with a stratified Taylor column that continue to supply iron to the base of the mixed-layer. Isopycnal doming in the Taylor column and restratification processes associated with Weddell-Scotia surface exchange also likely contribute to bloom development at Pine Bank, as well as proximity to an upstream shelf iron source. Furthermore, satellite chlorophyll data suggest that this localized process affects the wider Scotia Sea bloom region through downstream advection. Therefore, other regions within the Southern Ocean identified by Meredith et al. (2015) as favorable to Taylor column formation (e.g. Kerguelen Plateau, Maud Rise) deserve further examination to assess the role that this circulation plays in driving primary production.

2.6 Acknowledgments

C.J. Prend is supported by a National Science Foundation Graduate Research Fellowship under Grant No. DGE-1650112. S.T. Gille, L. D. Talley, I. Rosso, and M. R. Mazloff were supported by NSF PLR-1425989. S. T. Gille also received support from NSF OCE-1658001. B. G. Mitchell was supported by NSF ANT-0948338. Profiling float data were collected and made freely available the International Argo Program (http://www.argo.ucsd.edu, http://argo.jcommops.org) and by the Southern Ocean Carbon and Climate Observations and Modeling (SOCCOM) Project (http://soccom.princeton.edu) funded by the National Science

Foundation, Division of Polar Programs (NSF PLR-1425989), supplemented by NASA, and by Argo and the NOAA programs that contribute to it. Southern Ocean State Estimate (SOSE) output is publicly available (http://sose.ucsd.edu). Offline Lagrangian particle trajectories were calculated using Octopus (http://github.com/jinbow/Octopus).

Chapter Two, in full, is a reprint of the material as it appears in the Journal of Geophysical Research: Oceans, 2019. Prend, C. J., S. T. Gille, L. D. Talley, B. G. Mitchell, I. Rosso, and M. R. Mazloff (2019), Physical drivers of phytoplankton bloom initiation in the Southern Ocean's Scotia Sea, *Journal of Geophysical Research: Oceans*, 124, 5811-5826. © American Geophysical Union. Used with permission. The dissertation author was the primary investigator and author of this paper.

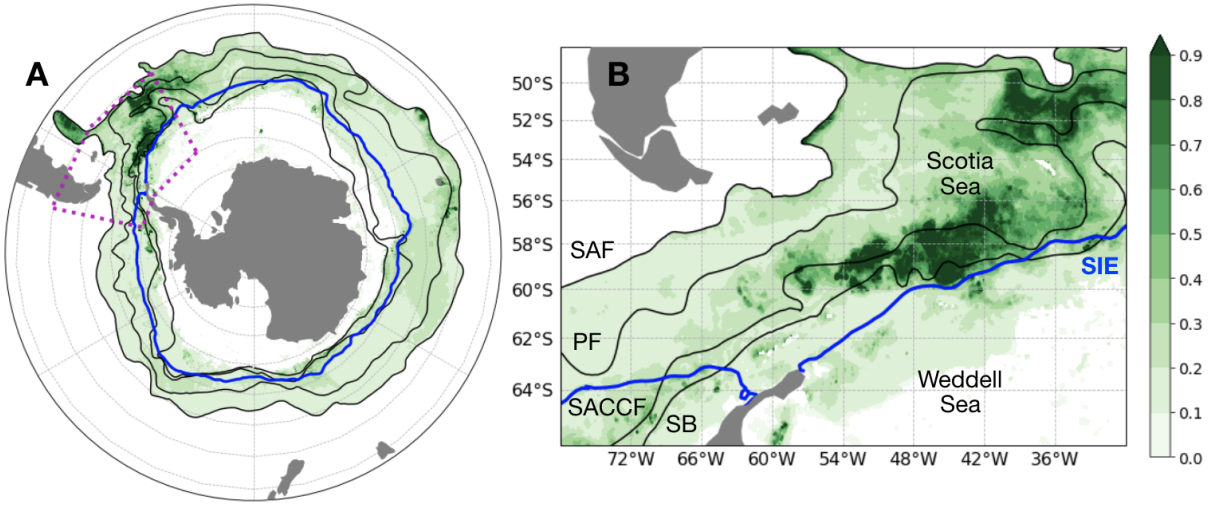

Figure 2.1. MODIS Aqua satellite 2002-2017 October surface chlorophyll composite [mg m^{-3}] with major ACC fronts (SAF: Subantarctic Front, PF: Polar Front, SACCF: Southern ACC Front, SB: ACC Southern Boundary) from Orsi et al. (1995) in black and 2002-2017 October Sea Ice Edge (SIE) from NOAA/NSIDC Climate Data Record in blue for (a) the entire Southern Ocean and (b) zoomed in on the Weddell-Scotia region, marked by a magenta box in (a). Note that the SIE is retreating at this time, so the mean position of the SIE during the month of October can overlap with the chlorophyll climatology, which includes data from the full month.

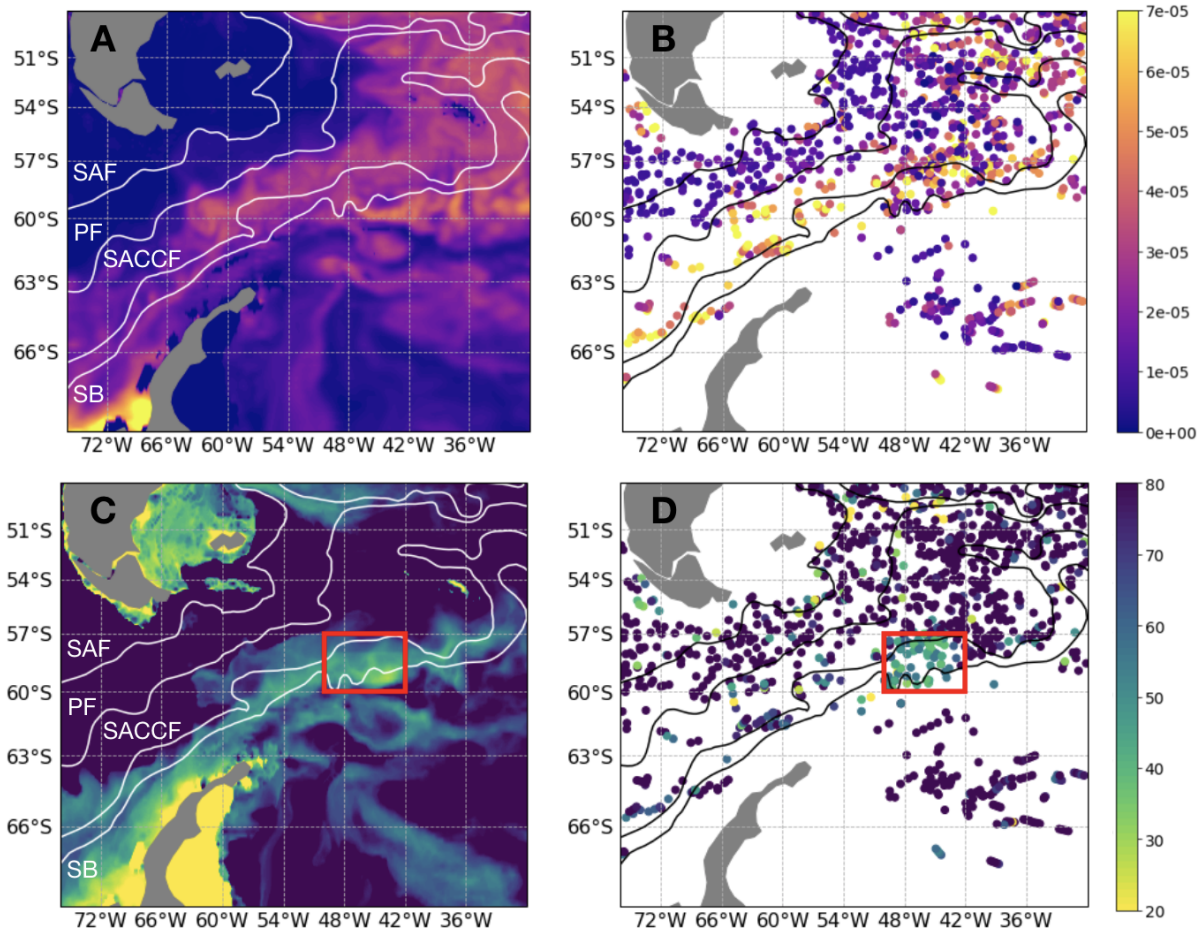

Figure 2.2. (a) Subsurface N^2 maximum [s^{-2}] in SOSE (b) and at individual Argo profiles during the early spring period (August 15-September 15). Also, the depth in the water column [m] where this maximum occurred, roughly the base of the mixed-layer (c) in SOSE and (d) from Argo. The red box in (c) and (d) highlights shallower than average MLD in the bloom region. Orsi et al. (1995) fronts plotted, as in Figure 2.1.

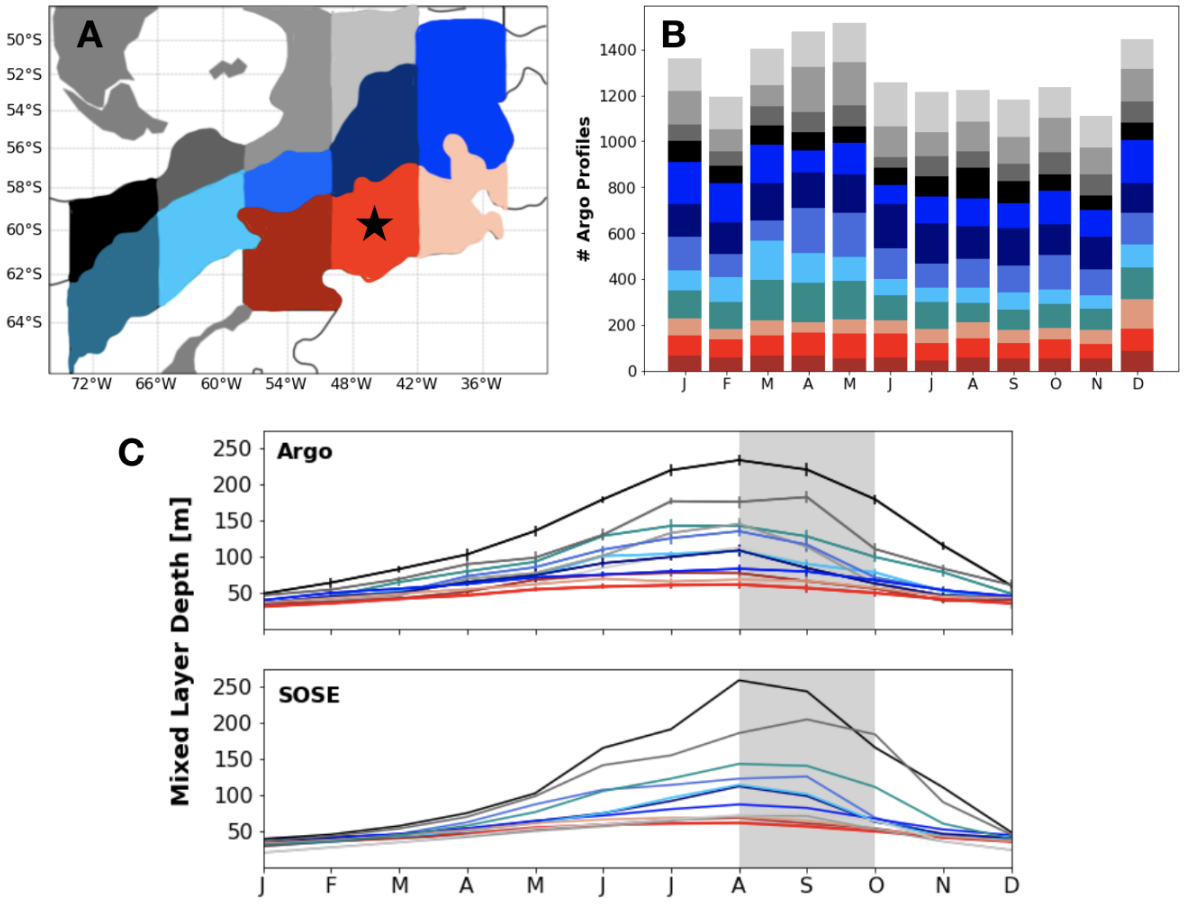

Figure 2.3. (a) Map showing the grid for Argo analysis based on frontal positions defined by mean dynamic topography contours from Swart et al. (2008). A black star marks the box containing the bloom site. (b) Histogram showing the number of Argo profiles located within each grid box by month. In total 15,615 profiles from 2002-2017 were used. (c) Monthly averaged mixed layer depth [m] for each grid box in (a) from Argo profiles (top panel) with error bars marking the 95% confidence interval and SOSE (bottom panel). Gray shading highlights August and September, the typical bloom initiation months.

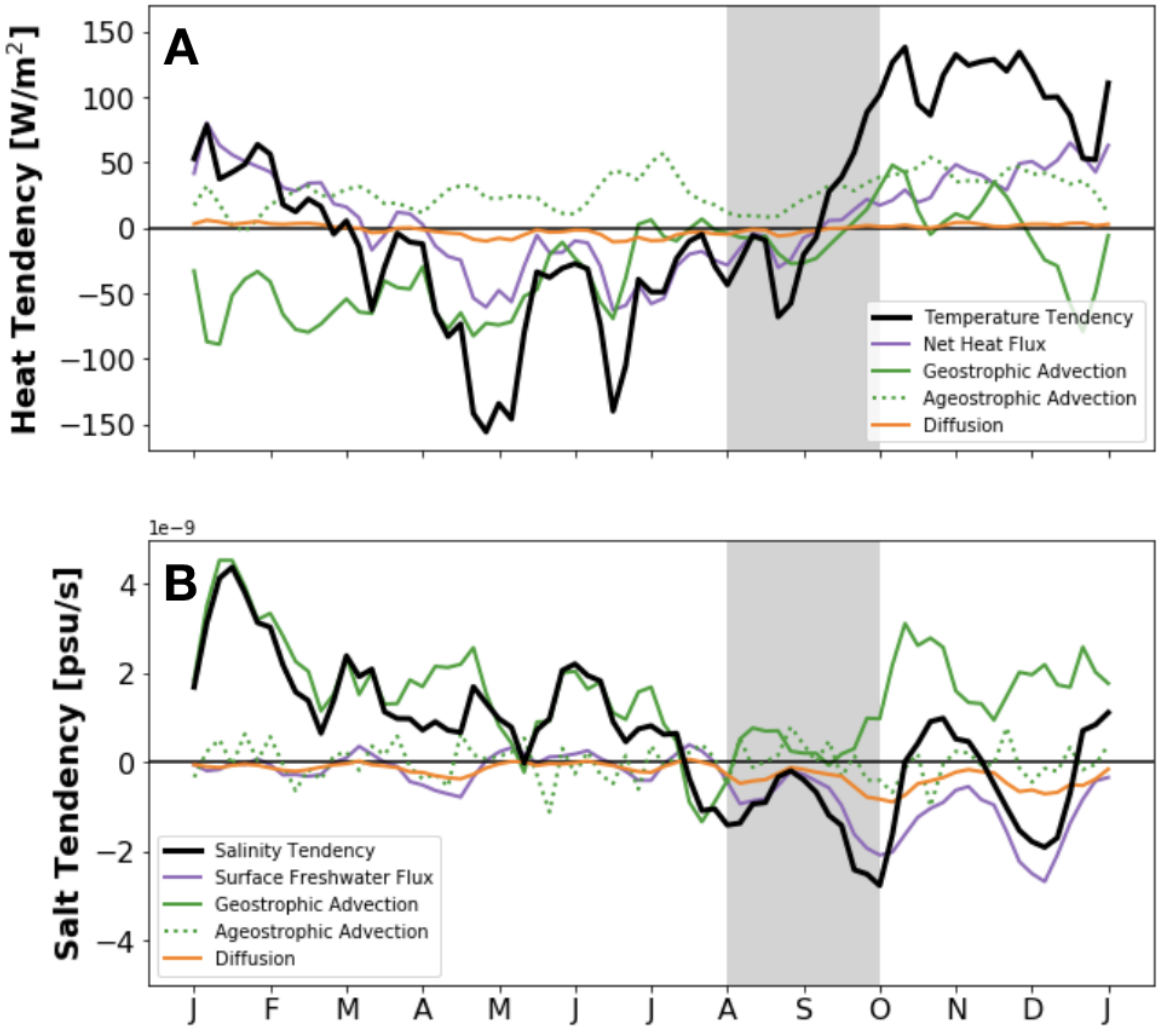

Figure 2.4. 2005-2010 mean SOSE (a) heat budget (positive values signify heating) and (b) salt budget (positive values signify salinification) spatially averaged over the bloom region (red starred box in Fig. 2.2a) and vertically integrated over the top 53 m (SOSE vertical level closest to the average mixed-layer depth). Gray shading highlights August and September, the typical bloom initiation months.

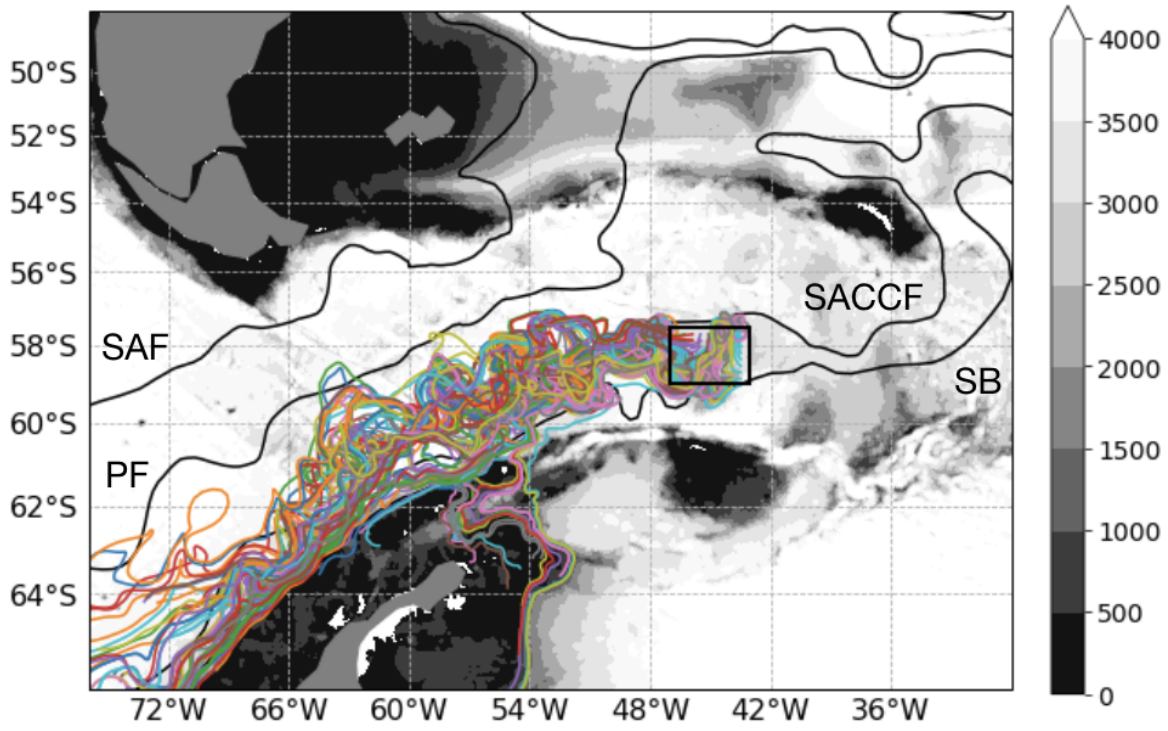

Figure 2.5. ETOPO1 bathymetry (shading [m]) with 100 randomly selected back trajectories from SOSE particle release experiment. Black box marks where particles were seeded. Orsi et al. (1995) fronts plotted in black.

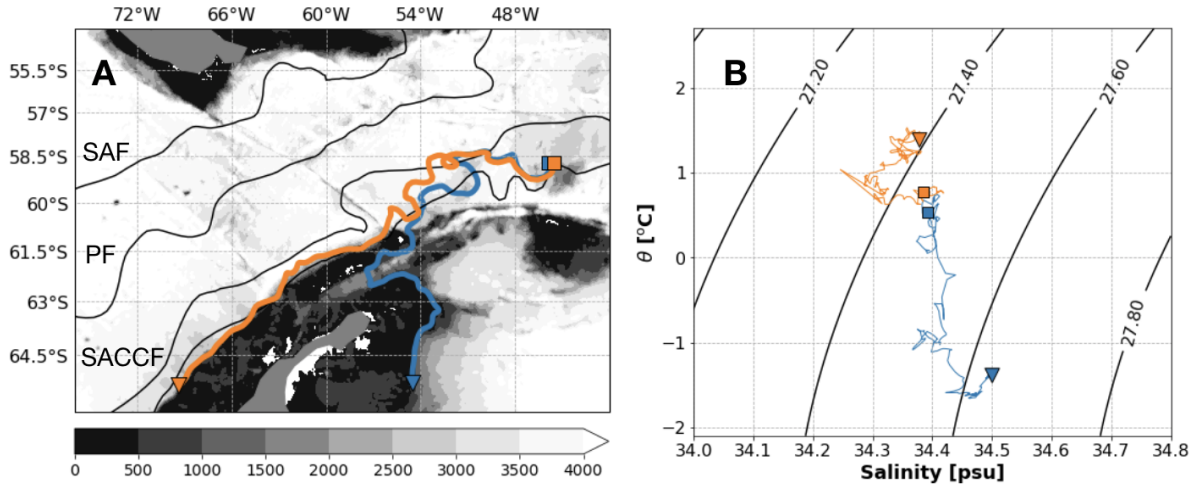

Figure 2.6. (a) ETOPO1 bathymetry (shading [m]) with two modeled particle trajectories representative of the major pathways traveled by waters that reach the bloom region. Orsi et al. (1995) fronts plotted in black. (b) θ-S properties along the trajectories in (a).

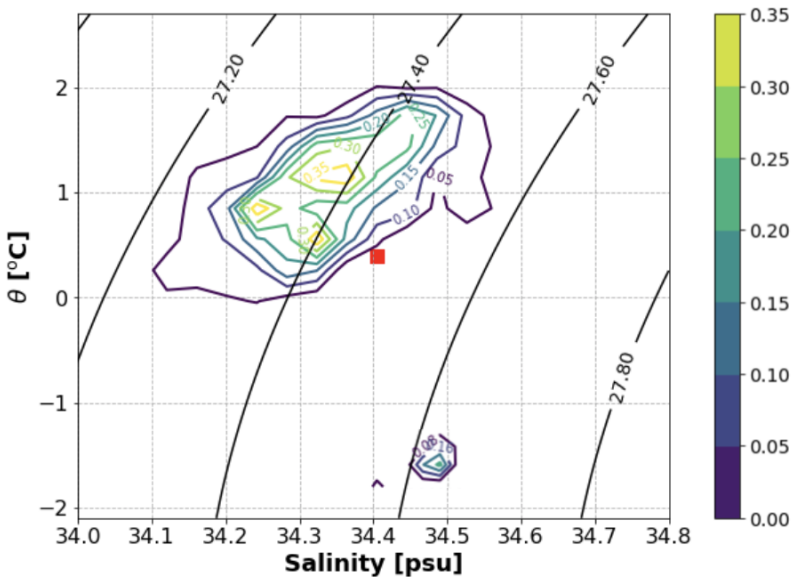

Figure 2.7. Joint probability density function of modeled particle θ [°C] and salinity [psu] at the particle's initial position after being run backward in time for 9 months. Red box marks the average θ-S properties of the modeled particles at their final position in the bloom region.

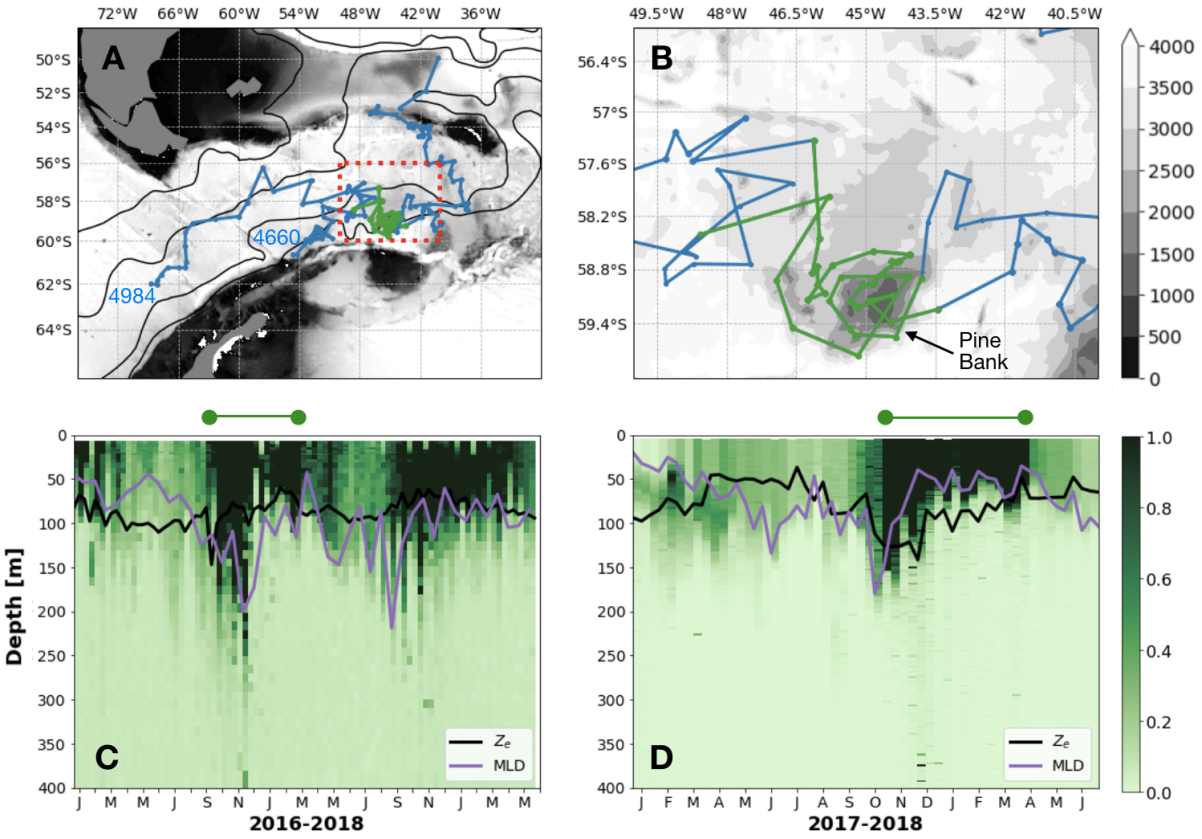

Figure 2.8. (a) ETOPO1 bathymetry (shading [m]) with float 5904660 and 5904984 trajectories and (b) zoomed in on the bloom region and Pine Bank (PB) (c) float 5904660 and (d) float 5904984 chl-*a* [mg m^{-3}] with MLD (purple [m]) and Z_e (black [m]) overlaid. Green portion of the trajectory corresponds to the period of high float chl-*a* (i.e. bloom period).

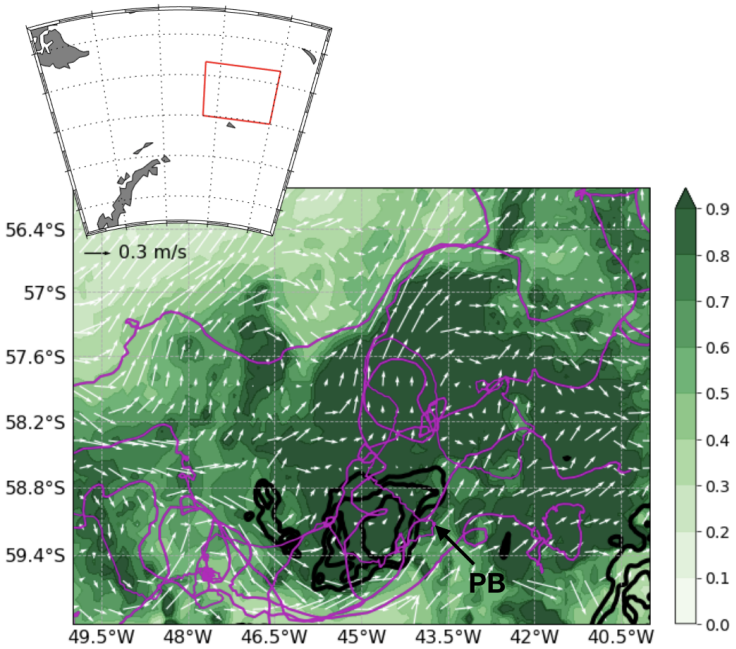

Figure 2.9. MODIS Aqua satellite 2002-2017 November surface chlorophyll composite [mg m^{-3}] for Pine Bank (PB) region, with black contours outlining ETOPO1 bathymetry shallower than 3000 m (500 m intervals). White arrows denote the November drifter-derived climatology of global near-surface currents. Individual surface drifter trajectories from November 2016 are also shown (magenta).

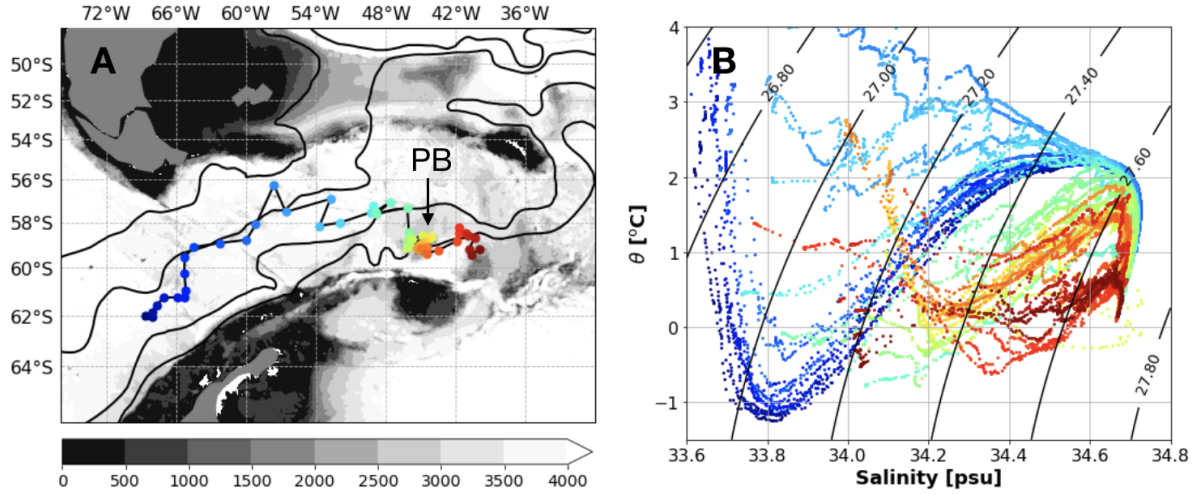

Figure 2.10. (a) ETOPO1 bathymetry (shading [m]) with SOCCOM float 5904984 trajectory; stations where the float took profiles are colored progressively from blue to red. Pine Bank (PB) is marked by an arrow and Orsi et al. (1995) fronts plotted in black. (b) Float θ-S properties colored by the corresponding stations along the trajectory in (a).

2.7 Supplementary Material

The Supplementary Material provides 3 additional figures as well as supporting text that describes a 1-D calculation estimating the magnitude of the air-sea and sea-ice fluxes necessary to modify Weddell water along its path to the Scotia Sea in order to produce the bloom region θ-S properties when mixed with the ACC source water in the proportions suggested by the particle release experiment discussed in Section 2.3.2.

In Section 2.3.2, it was suggested that Weddell outflow may be modified by surface fluxes while traveling to the bloom region. A calculation can be done to estimate the magnitude of these air-sea and sea-ice fluxes necessary to produce the bloom region θ-S properties. For example, we can take a mixture that is made up of 90% ACC source water (with θ_{ACC}) and then calculate the temperature, θ_2, of the additional 10% that would be necessary in order to produce the observed bloom region temperature, θ_{BLOOM} (i.e. $0.9\theta_{\mathrm{ACC}} + 0.1\theta_2 = \theta_{\mathrm{BLOOM}}$). If we then assume that the difference $\Delta\theta$ between θ_2 and the Weddell source water temperature, θ_{WED}, is solely due to air-sea heat fluxes, an approximation of the net heat flux can be found from the 1-D balance:

$$Q_{\mathrm{NET}} = \frac{\Delta\theta}{\Delta t}\rho c_p h, \tag{2.4}$$

where $\Delta\theta$ = θ_2 - θ_{WED} ($\Delta\theta > 0$), and $\Delta t \approx 9$ months is the advective timescale for particles to travel from the Weddell Sea to the bloom region. The approximate values $\rho \approx 1025$ kg m^{-3}, $c_p \approx 4000$ J kg^{-1} °C^{-1}, and $h \approx 100$ m, yield $Q_{\mathrm{NET}} \approx 50$ W/m^2. This value is a crude estimate, but it is consistent in magnitude with the mean air-sea heat flux in the region from multiple reanalysis products (e.g. Cerovečki et al., 2011).

Similarly, for the salinity, take a mixture that is made up of 90% ACC source water (with S_{ACC}) and then calculate the salinity, S_2, of the additional 10% that would be necessary in order to produce the observed bloom region salinity, S_{BLOOM} (i.e. $0.9S_{\mathrm{ACC}} + 0.1S_2 = S_{\mathrm{BLOOM}}$). If we then assume that the difference ΔS between S_2 and the Weddell source water salinity, S_{WED}, is solely due to surface freshwater fluxes, an approximation of the sea ice freshwater forcing can be found from the 1-D balance:

$$IO = E - P - R - \frac{\Delta S}{\Delta t}\frac{h}{S_0}, \tag{2.4}$$

where ΔS = S_2 - S_{WED} ($\Delta S < 0$), and $\Delta t \approx 9$ months. Taking approximate values $S_0 \approx 34.4$ psu, $h \approx 100$ m, E–$P \approx$ -100 cm/yr (estimated for the region from E-P fields in Cerovečki et al., 2011), and $R \approx$ -0.14 m/yr (runoff into the Weddell Sea from model simulation in Kjellsson et al., 2015), yield $IO \approx$ -0.9 m/yr. As for the net heat flux, this is a rough estimate but is similar to values of the net ice-ocean freshwater flux in the region from Haumann et al. (2016). To be clear, our intent is simply to demonstrate that air-sea fluxes and sea ice melt could conceivably modify Weddell water enough to produce the bloom region θ-S properties when mixed with the ACC source water in the proportions suggested by the particle release experiment. However, quantifying these processes more rigorously is beyond the scope of this study.

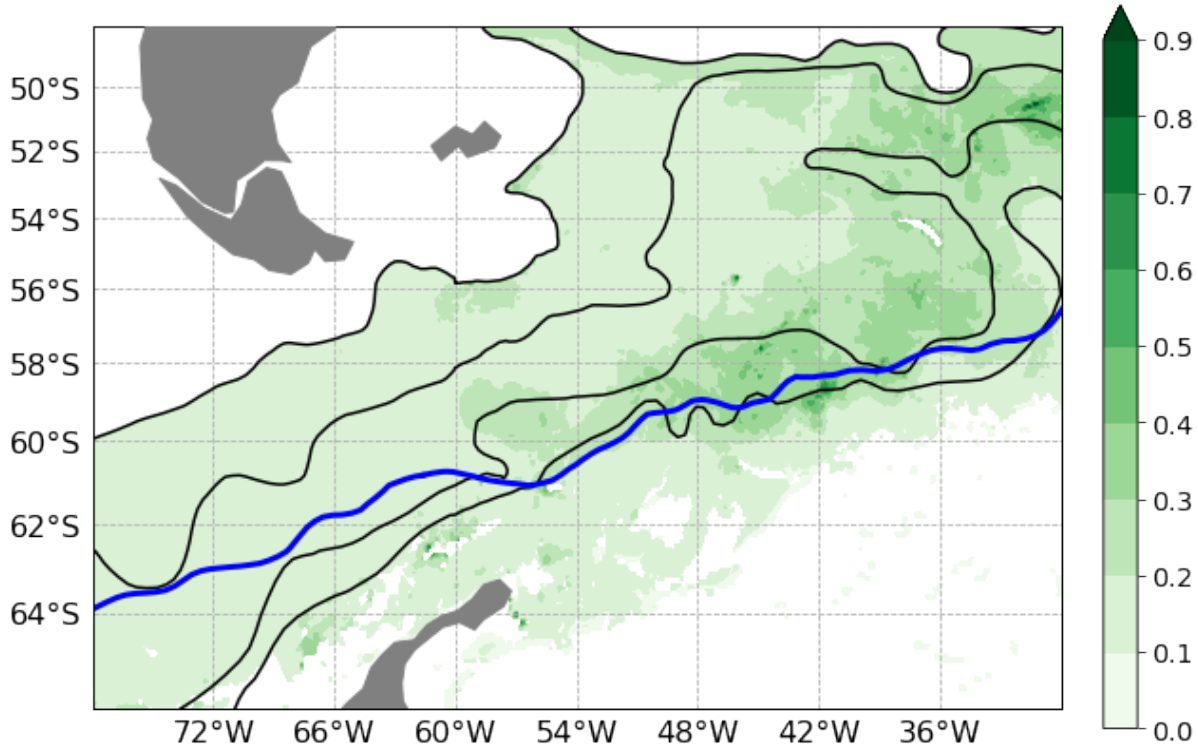

Figure 2.11. MODIS Aqua satellite 2002-2017 September surface chlorophyll composite [mg m^{-3}] with major ACC fronts from Orsi et al. (1995) in black and 2002-2017 September sea ice edge from NOAA/NSIDC Climate Data Record in blue.

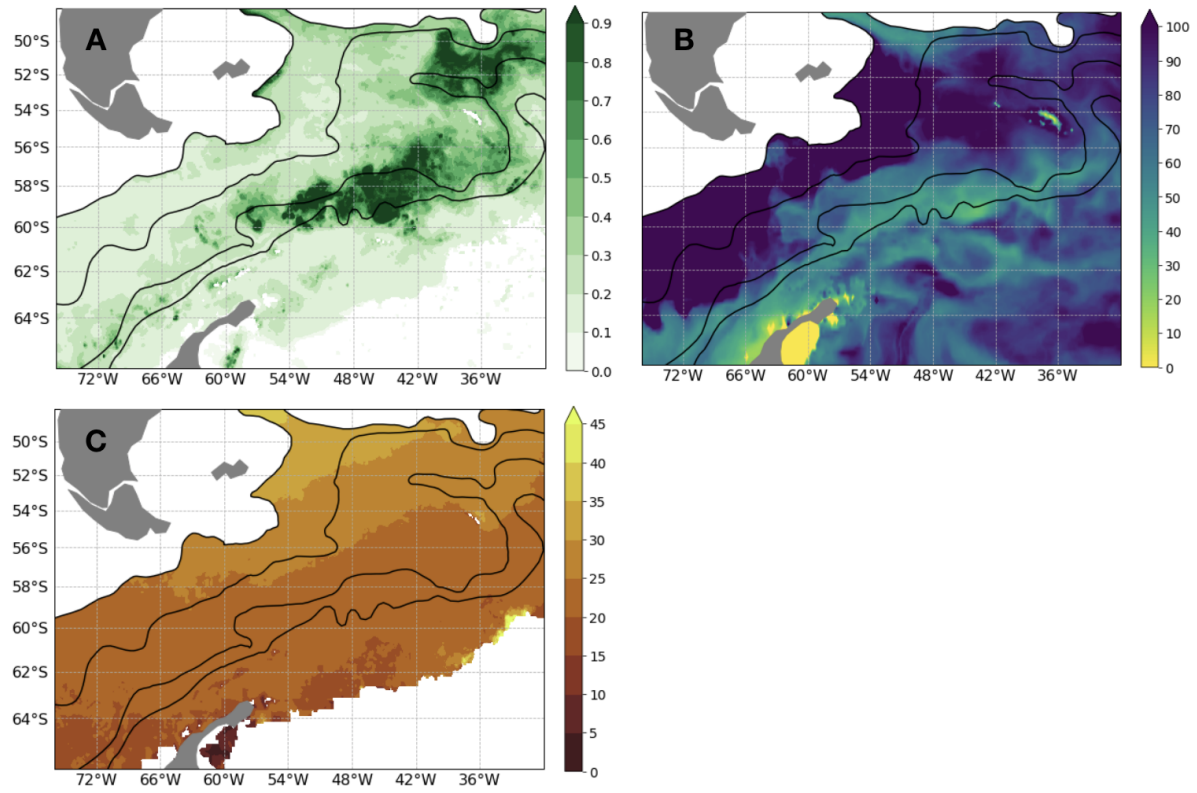

Figure 2.12. (a) MODIS Aqua satellite 2002-2017 October surface chlorophyll climatology [mg m^{-3}] (b) SOSE 2005-2010 October mixed-layer depth climatology [m] (c) MODIS Aqua satellite 2002-2017 October photosynthetically available radiation climatology [μE m^{-2} s^{-1}].

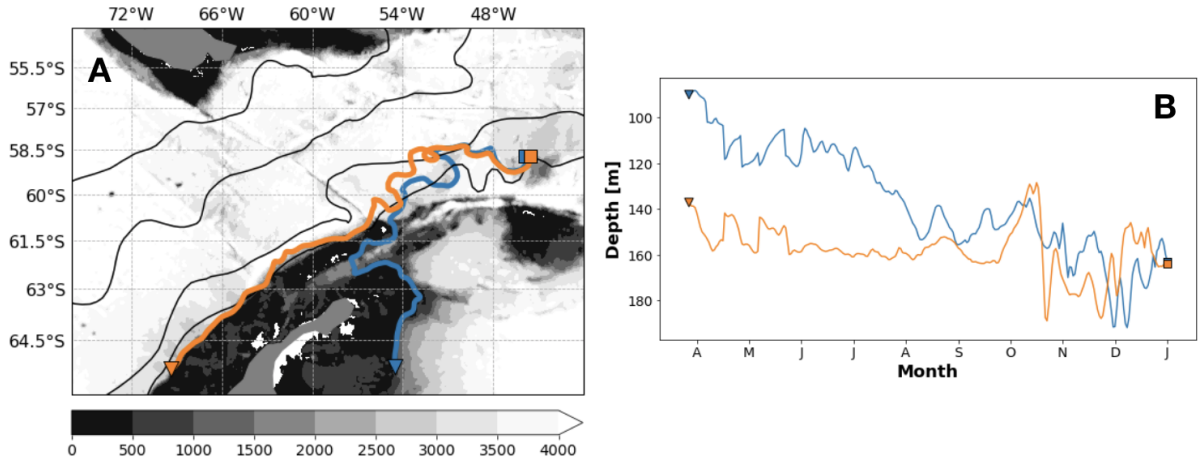

Figure 2.13. (a) ETOPO1 bathymetry (shading [m]) with two modeled particle trajectories representative of the major pathways traveled by waters that reach the bloom region. (b) Change in particle depth [m] along the two pathways shown in (a).

Chapter 3

Parameterizing eddy transport of biogeochemical tracers

Abstract

The distribution of oceanic biogeochemical tracers is fundamentally tied to physical dynamics at and below the mesoscale. Since global climate models rarely resolve those scales, turbulent transport is parameterized in terms of the large-scale gradients in the mean tracer distribution and the physical fields. Here, we demonstrate that this form of the eddy flux is not necessarily appropriate for reactive tracers, such as nutrients and phytoplankton. In an idealized nutrient-phytoplankton system, we show that the eddy flux of one tracer should depend on the gradients of itself and the other. For certain parameter regimes, incorporating cross-diffusion can significantly improve the representation of both phytoplankton and nutrient eddy fluxes. We also show that the efficacy of eddy diffusion parameterizations requires timescale separation between the flow and reactions. This result has ramifications for parameterizing sub-grid scale biogeochemistry in more complex ocean models since many biological processes have comparable timescales to submesoscale motions.

3.1 Introduction

Biogeochemical properties in the ocean, including nutrients and phytoplankton, exhibit patchiness at the mesoscale and submesoscale (Martin et al., 2002; Mahadevan & Campbell,

2002; Lévy & Martin, 2013). This is evident from satellite images of ocean color, a proxy for phytoplankton biomass, which clearly show the expression of eddies, filaments, and other small-scale structure in the flow (Gower et al., 1980). Phytoplankton patchiness is generated by a complex interplay between physical and biogeochemical processes, each with their own range of length and time scales (Flierl & McGillicuddy, 2002; Lévy et al., 2012; McGillicuddy, 2016). This includes the lateral stirring of large-scale gradients by the turbulent flow (Abraham, 1998; Martin, 2003; McKiver et al., 2009) as well as stimulation of phytoplankton growth by (sub-)mesoscale processes delivering nutrients to the euphotic zone (Falkowski et al., 1991; Flierl & Davis, 1993; Lévy et al., 2001; M. A. Freilich & Mahadevan, 2019; Uchida et al., 2020).

The relative importance of stirring, which passively reorganizes existing gradients, versus localized upwelling, which actively forces changes in phytoplankton abundance, must be determined in order to quantify the global significance of (sub-)mesoscale productivity (Lévy et al., 2018). Still, it has been suggested that phytoplankton patchiness impacts large-scale productivity (Jenkins, 1988; Brentnall et al., 2003) and may be important to global biogeochemical budgets (Platt & Sathyendranath, 1988; Falkowski et al., 1991; Doney et al., 2004; Omand et al., 2015). This poses a problem for global climate models, which rarely resolve processes at or below the mesoscale, $\mathcal{O}(100\text{ km})$. Therefore, the tracer transport associated with the unresolved dynamics must be parameterized. This is typically done by assuming that eddy fluxes are proportional to the gradients in the mean field, the so-called gradient-diffusion hypothesis. In this framework, the unresolved turbulent dispersion is represented as an enhanced molecular diffusion:

$$\overline{u'c'} = -K_e \nabla \overline{c}, \tag{3.1}$$

where K_e is an effective diffusivity, c is any arbitrary tracer, the overbar represents an ensemble average and the prime denotes time-dependent fluctuations from the mean. The implicit assumption is that the chaotic random motions associated with turbulence are comparable to Brownian motion. Despite its near-ubiquitous use, limitations of the eddy-diffusion parameterization have

been noted (Lee et al., 1997; Sobel, 1999; Ferrari & Nikurashin, 2010; Manucharyan et al., 2017), particularly for reactive tracers, which have a growth or decay in time that is independent of the flow and thus do not remain constant following a fluid parcel.

Many biogeochemical quantities can be modeled as reactive tracers. For example, phytoplankton growth via nutrient uptake and loss due to zooplankton grazing can be expressed mathematically as reaction terms. The reaction timescale of a tracer is known to impact both the degree of observed patchiness (Mahadevan & Campbell, 2002), as well as the validity of eddy diffusion parameterizations (Pasquero, 2005). Indeed, assessing the ability of the gradient-diffusion hypothesis, Equation (3.1), to accurately represent the transport of both reactive and non-reactive tracers is not a new concept (Mooney & Wilson, 1993; da Silva & Pereira, 2007; Lightstone & Raithby, 2009). However, the past work that approaches this problem in the context of oceanic biogeochemical tracers typically either (a) uses relatively complex biogeochemical models coupled to idealized background flows (Abraham, 1998; Denman, 2003; Tzella & Haynes, 2007) or (b) uses non-reactive tracers in realistic flows (Smith et al., 2016). These approaches, while useful, are computationally expensive and it can be challenging to isolate the fundamental dynamics. Here, we argue that there is still insight to be gained from a system with a simple biogeochemical model *and* flow field. This allows us to investigate the theoretical underpinnings of the physical-biological interactions and examine the system across the full range of parameter space. The results can then inform past and future work that employs more complex models, both physical and biogeochemical.

3.2 Methods and Theory

3.2.1 Biological Model

Nutrient-phytoplankton-zooplankton (NPZ) models have been used in oceanographic research for decades. A standard NPZ model has 5 transfer functions, each with countless possible functional forms (see Franks (2002) for a nice review). The NPZ framework has also

been extended to include the effects of bacteria and detritus, and is similar to the multi-component systems used in the current generation of global climate models (Cushing, 1975; Fasham et al., 1990; Aumont et al., 2015). However, a more complex biogeochemical model is not necessarily a better one for developing process-based understanding (Franks, 2002; Turner et al., 2014). Here, we follow the lead of Hodges and Rudnick (2004), and M. A. Freilich and Mahadevan (2019), and opt to ignore the zooplankton component entirely, selecting basic Lotka-Volterra forms for the remaining transfer functions. The result is the simplest possible model that still captures fundamental aspects of plankton dynamics. Including explicit diffusion (with diffusivity κ) the equations are:

$$\frac{\partial N}{\partial t} + \mathbf{u} \cdot \nabla N - \kappa \nabla^2 N = -\mu NP - \lambda N + \lambda N_D \tag{3.2}$$

$$\frac{\partial P}{\partial t} + \mathbf{u} \cdot \nabla P - \kappa \nabla^2 P = \mu NP - \lambda P, \tag{3.3}$$

where the nutrient (N) and phytoplankton (P) concentration fields have the same units (e.g. moles of nitrogen per unit volume), μ [(mol N m^{-3})$^{-1}$s^{-1}] is the nutrient uptake rate, λ [s^{-1}] is the entrainment rate, and $\mathbf{u}$ is a 2-dimensional velocity field. These equations describe the dynamics of the biology in the upper ocean, where N and P represent average concentrations in the mixed layer, and N_D is the subsurface nutrient concentration. The right-hand side reaction terms in Equation (3.2) correspond to nutrient depletion via uptake by phytoplankton ($-\mu NP$) and detrainment across the mixed-layer base ($-\lambda N$), as well as nutrient resupply by the entrainment of nutrient-rich waters from below (λN_D). Although we suggest that λ can be interpreted as an entrainment rate, it is specified a priori and not related to the velocities. Technically, λ acts like a reaction rate from the perspective of the biological system. Analogous reaction terms are present in Equation (3.3), with the exception that entrainment only decreases P (since it is assumed that subsurface waters below the mixed layer are also below the euphotic zone and thus devoid of phytoplankton). This system can be non-dimensionalized in terms of the following

dimensionless variables:

$$x^* = \frac{x}{L},\ y^* = \frac{y}{L},\ \mathbf{u}^* = \frac{\mathbf{u}}{U},\ t^* = t\mu\tilde{N}_D,\ N^* = \frac{N}{\tilde{N}_D},\ P^* = \frac{P}{\tilde{N}_D}, \tag{3.4}$$

where $\tilde{N}_D$ is some characteristic N value, for example $\langle N_D \rangle$ where $\langle \cdot \rangle$ denotes a spatial average. The diffusive terms in Equations (3.2) and (3.3) scale inversely with the Péclet number, $Pe = UL/\kappa$. The entire right-hand side of both equations scale with the Damköhler number, $Da = \mu\tilde{N}_D L/U$, which is the ratio of advective (L/U) and reactive $(1/\mu\tilde{N}_D)$ timescales. The entrainment terms are further scaled by the ratio of reaction rates $(\lambda/\mu\tilde{N}_D)$.

Our motivation in choosing this simplified set of equations is to avoid introducing extraneous nonlinearity, for example, from poorly constrained transfer functions associated with the zooplankton component in NPZ models. Certainly, we note that this system does not capture all of the relevant processes controlling phytoplankton biomass. By neglecting zooplankton, our model does not capture top-down controls, which have been shown to be important in determining phytoplankton abundance (Behrenfeld & Boss, 2014); these predator-prey interactions are also thought to be influenced by the dominant scales of motion in the flow (Srokosz et al., 2003; Richards & Brentnall, 2006; Taniguchi et al., 2014). The advantage of our idealized formulation, Equations (3.2 - 3.3), is that it is a tractable system which can be probed to understand the sensitivity to various parameters. Our reduced NPZ form allows us, for example, to conduct a multiple scale analysis, which provides theoretical insight into the appropriate form of reactive tracer eddy fluxes.

The concept of an eddy diffusivity introduced by G. I. Taylor (1921) is related to the Lagrangian velocity experienced by particles. However, this framework can be extended to the spreading of tracers in an Eulerian context. Papanicolaou and Pironneau (1981) showed that by assuming a scale separation between the eddies and mean flow, Equation (3.1) can be derived via a multiple scale analysis of the advection-diffusion equation for a passive tracer. Here, we apply a similar technique to Equations (3.2) and (3.3) to illustrate how additional reaction terms

influence the form of the eddy flux. As in the passive tracer case, we assume a scale separation between the turbulent eddies (ℓ) and the large-scale circulation (L). This suggests a perturbation expansion in terms of the small parameter $\varepsilon \equiv \ell/L$, where slow time and space variables are defined as $T = \varepsilon t$ and $\mathbf{X} = \varepsilon \mathbf{x}$, respectively. The velocity is also decomposed into mean and eddy components, $\mathbf{u} = \mathbf{U}(\mathbf{X},T) + \mathbf{u}'(\mathbf{x},t;\mathbf{X},T)$. Solutions for N and P then take the form:

$$N = N_0(\mathbf{X},T) + \varepsilon N_1(\mathbf{x},t;\mathbf{X},T) + \mathscr{O}(\varepsilon^2) \tag{3.5}$$

$$P = P_0(\mathbf{X},T) + \varepsilon P_1(\mathbf{x},t;\mathbf{X},T) + \mathscr{O}(\varepsilon^2). \tag{3.6}$$

Note that the mean flow and leading order biological behavior are both taken to be functions of the large scales only. We substitute the expansions, Equations (3.5 - 3.6), into the advection-diffusion-reaction system, Equations (3.2 - 3.3). At each order of ε, averaging over the small and fast scales yields a solvability condition. The evolution equations for the large-scale, long-time, averaged tracer concentrations, $\overline{N}$ and $\overline{P}$, are then obtained by summing the solvability conditions up to $\mathscr{O}(\varepsilon^2)$. The results imply that the eddy fluxes of N and P have the form:

$$\overline{u'N'} = -K_{NP}\nabla\overline{P} - K_{NN}\nabla\overline{N}, \tag{3.7}$$

$$\overline{u'P'} = -K_{PP}\nabla\overline{P} - K_{PN}\nabla\overline{N}, \tag{3.8}$$

where K_{NP}, K_{NN}, K_{PP}, are K_{PN} are effective diffusivities that can be expressed in terms of μ, λ, and $\overline{P}$. Equations (3.7) and (3.8) have the eddy fluxes (i.e. the magnitude of the vectors $|\langle \mathbf{u}'P' \rangle|$ and $|\langle \mathbf{u}'N' \rangle|$) depending on the large-scale, mean tracer gradients ($|\nabla\langle P \rangle|$ and $|\nabla\langle N \rangle|$), as in the traditional gradient-diffusion result. However, unlike in the passive tracer case, we find that the fluxes of N and P depend on the large-scale gradients of *both* tracers. There may be cases, for example, where the eddy flux of phytoplankton is controlled by the gradient in the mean nutrient concentration (rather than by gradients in $\overline{P}$). This phenomenon is known as cross-diffusion (Vanag & Epstein, 2009) and is due to the coupling between Equations (3.2) and (3.3) that results

from the nonlinear nutrient uptake term, μNP.

To understand cross-diffusion physically, consider a case where $\langle N \rangle$ increases to the north. A parcel of fluid moving south will have a positive N'; as a result P' will increase. When it arrives at some latitude, it will have positive P' and negative v'. Likewise, a parcel coming from the south will arrive at the same latitude with negative P' and positive v'. Thus, the flux $\langle v'P' \rangle$ is negative, corresponding to a P flux down the gradient of $\langle N \rangle$. There can, of course, also be contributions from the gradient of $\langle P \rangle$, but, for linearized perturbation equations, the two contributions can be treated separately and added to get the net flux. The diffusive coefficients associated with the cross terms can also be negative. For example, consider an infinitesimal wave on a background with uniform μ, λ and no gradient in nutrients. Flows away from high subsurface nutrients carry excess phytoplankton, which draws down nutrients producing a negative anomaly, while flow the other way has a positive anomaly. In other words, although there is no background gradient in nutrients, there is a nutrient flux up the gradient of phytoplankton.

3.2.2 Physical Model

With the results from the multiple scale analysis in mind, we now investigate the dynamics of the nutrient-phytoplankton model in a simple flow field. The dimensional equations (3.2) and (3.3) are coupled to a 2-D stirring flow adapted from the clever "renovating wave" model in Pierrehumbert (1994). The velocity fields are generated by a streamfunction of the form:

$$\Psi = \sum_{n=1}^{4} U_n \cos(k_{1n}x + k_{2n}y + \theta_n), \tag{3.9}$$

where the wavenumbers k_{1n} and k_{2n} and amplitude U_n are selected so that the kinetic energy spectrum is consistent with scaling laws of turbulence (i.e. $k^{-5/3}$ slope) and θ_n is a random-walking phase shift. In other words, sinusoidal shear flows are periodically "renovated" by a random phase shift at each time step ($dt = 1/32$ to satisfy a Courant-Friedrichs-Lewy condition) to generate a flow that is zero-mean in time and has qualitative similarities to 2-D turbulence.

We tested multiple spectra, including a non-local k^{-3} spectrum, but opted for a flow with more small-scale energy, since this is common in surface quasi-geostrophic turbulence characteristic of the upper ocean. The exact choice of spectrum does not affect the existence of the cross-fluxes or the dependence on the relative time scales. Similar models have been used in the study of phytoplankton patchiness (Young et al., 2001; Hodges & Rudnick, 2006). The model domain is $4\pi \times 4\pi$ and doubly-periodic. N and P transport is represented by a first-order upwind advection scheme to maintain positivity. The flow is homogeneous by construction and nearly isotropic (it is not exactly isotropic due to the double periodicity), so it can be represented by a single constant diffusivity.

3.2.3 Model Parameters

In principle, μ, λ, and N_D could all be spatially variable. Here, we describe simulations in which μ is modeled as a sinusoid, $\mu_0 + \mu_1 \cos(y/2)$. This form is chosen to maintain periodicity. The N_D and initial distribution of total nitrogen in the system ($S = N + P$) are also selected to be sinusoidal, although with east-west gradients to distinguish from gradients in μ; λ is chosen to be a constant. The motivation for selecting μ and N_D to be orthogonal is to create gradients in N and P which are distinctly different, allowing us to more easily investigate the cross fluxes. The initial P distribution is determined from the leading order P solution found in the multiple scale analysis ($P_0 = N_D - \lambda/\mu$). The initial N distribution is determined by subtracting P_0 from the initialized S ($N_0 = S_0 - P_0$). Eddies and filaments in the N and P fields quickly form, and are maintained, in many cases, through biological reactions. Figure 3.1 shows snapshots of the nutrient and phytoplankton concentration fields (a,b) and nutrient and phytoplankton eddy fluxes (c,d) for two different simulations after reaching equilibrium. The patchy, filamentary distributions in Figure 3.1a are representative of many oceanic regimes. The simulations have the same flow field and initial conditions but varied reaction rates, namely $Da = 1$ for Figure 3.1a,c and $Da = 0.1$ for Figure 3.1b,d.

3.3 Results

The long-time behavior of the model is greatly affected by the presence of reaction terms as well as the the reaction timescales. To illustrate this, several simulations were run with different values of λ and $\langle\mu\rangle$. Figure 3.2 shows time series of phytoplankton concentration and variance for different values of Da, which is diagnosed from the dimensional model using the spatial averages $\langle\mu\rangle$, $\langle N_D\rangle$, and $\sqrt{\langle u^2\rangle}$. For a non-reactive tracer (i.e. $Da = 0$) the mean tracer concentration over the domain stays constant and the variance decays exponentially to zero as the stirring smooths out the gradients associated with the initial conditions (Pierrehumbert, 2000; Hodges & Rudnick, 2006). Biological reaction terms introduce a chaotic time dependence. After an initial transient period, the mean tracer concentration fluctuates randomly in time around an equilibrium level which depends on the relative rates of phytoplankton growth and losses. When the ratio of phytoplankton detrainment to growth, $\lambda/\langle\mu\rangle$, is held constant, the equilibrium concentration value is fixed. Fluctuations are also seen in the tracer variance, which never decays to zero. The amplitude of the changes in $\langle P\rangle$ depends on the ratio of reaction and flow timescales, Da. The fluctuations (and consequently the variance) are largest for $Da = 1$ and $Da = 10$ due to the interaction between stirring and growth. This can be seen from the snapshots of N and P in Figure 3.1; the tracers are well-mixed in 3.1b ($Da = 0.1$) compared to 3.1a ($Da = 1$).

The presence of biological reactions impacts the appropriate value of the effective diffusivity (Figure 3.3), as well as the validity of the gradient-diffusion hypothesis. Since the time-mean of the velocity field is zero, the tracer fluxes from the model advection scheme are equal to the eddy fluxes $\overline{u'P'}$ and $\overline{u'N'}$, taken to be the magnitude of the vectors $|\langle\mathbf{u}'P'\rangle|$ and $|\langle\mathbf{u}'N'\rangle|$. Note that here, eddy flux refers to the advective transport of tracers by the fluctuating component of the velocity field, rather than the biological fluxes (i.e. $N'P'$ terms), often called eddy reactions. While eddy reactions also affect the distribution of biogeochemical tracers, their magnitude depends inherently on the mathematical form of the reaction terms. For our highly simplified model, the eddy reactions are much smaller than the eddy transports, although this is

not necessarily the case in more complex biological models (Lévy & Martin, 2013).

Since we are focused on transport by the time-fluctuating velocity, the advective fluxes diagnosed directly from the model are referred to as the "true" eddy flux. These are depicted, for example, at a single time step in Figure 3.1c,d. An effective diffusivity, K_e can be computed by regressing the true eddy flux onto the tracer gradients, $|\nabla\langle P\rangle|$ and $|\nabla\langle N\rangle|$, calculated at each grid cell from the mean N and P distributions after the simulation reaches equilibrium ($t = 1000$) to the end of the run ($t = 5000$). It is then possible to compare the true eddy flux with $-K_e\nabla\overline{c}$ at each grid point. Figure 3.4 gives examples of this for two simulations with the same initial conditions, one with biological reaction terms (Figure 3.4a) and one without (Figure 3.4b). Deviations from the black 1:1 line indicate a breakdown of the standard gradient-diffusion hypothesis.

Figure 3.4 suggests that, for the same initial conditions and velocity field, reactive tracer transport is poorly represented in terms of an eddy diffusion when compared to the non-reactive tracer case. Naturally, however, the specifics will depend on the model parameters. To illustrate this, we calculate the R^2 value, which measures the goodness of fit, to quantify the validity of $\overline{u'c'} = -K_e\nabla\overline{c}$ for different values of Da. R^2 values near 1 suggest that the gradient-diffusion hypothesis is a good assumption, whereas smaller R^2 values indicate that it breaks down. The results in Section 3.2.1 point to the possible importance of cross-diffusion, so we also compute K_{NP}, K_{NN}, K_{PP}, and K_{PN} by regressing the true eddy fluxes onto both $\nabla\overline{P}$ and $\nabla\overline{N}$, rather than regressing $\overline{u'P'}$ onto $\nabla\overline{P}$ only (and $\overline{u'N'}$ onto $\nabla\overline{N}$ only). Adding additional predictors to a regression model can lead to spurious increases in R^2, so adjusted R^2 values (Cramer, 1987) are calculated for the multiple regression.

R^2 is found to vary strongly with Da (Figure 3.5). Since reaction terms scale with Da in the non-dimensionalized N and P equations, they are negligible in the limit of slow reaction rates relative to stirring, $Da \ll 1$. Consequently, in these regimes, N and P can be treated as non-reactive tracers and have high R^2 values (> 0.7), both for $\overline{u'P'} = -K_e\nabla\overline{P}$ (blue in Figure 3.5) and $\overline{u'P'} = -K_{PP}\nabla\overline{P} - K_{PN}\nabla\overline{N}$ (orange in Figure 3.5). Still, even passive tracer transport is

not perfectly described by an eddy diffusion, which may be related to non-local effects (Lee et al., 1997; Sobel, 1999; Manucharyan et al., 2017). When the reaction and flow timescales are of the same order, $Da \sim \mathcal{O}(1)$, R^2 values are much lower (< 0.3), suggesting a breakdown of the gradient-diffusion hypothesis. We note that this is true even when cross-diffusion terms are included. Recall that the derivation of (3.7) and (3.8) required space and time scale separation between the turbulent eddies and reactions. This assumption is violated, by definition, when $Da \sim \mathcal{O}(1)$. In other words, mimicking turbulent transport as an enhanced diffusion is only valid when there is a timescale separation between the reaction and eddies. We also find that when $Da \sim \mathcal{O}(1)$, fluctuations in N and P persist over the scales of variation of $\bar{P}, \bar{N}, \mu$, and N_D, and tend to be out of phase with the flow, which likely contribute to the breakdown of the parameterization.

In the limit of fast reaction rates relative to stirring, $Da \gg 1$, the R^2 values are significantly increased by including cross-diffusion (Figure 3.5). This suggests that there are parameter regimes where the mean nutrient gradient is a better predictor of the phytoplankton eddy fluxes than the mean phytoplankton gradient. The importance of cross-diffusion can be examined through K_{PP}/K_{PN}, the ratio of effective diffusivities from (3.8), which depends on the ratio of reaction rates, $\lambda/\mu N_D$. $\lambda/\mu N_D$ also scales the entrainment terms in the nondimensionalized N and P equations. When $\lambda/\mu N_D \ll 1$, K_{PN} is larger than K_{PP}, i.e. the phytoplankton eddy flux is controlled by the mean nutrient gradient. This corresponds to cases where the leading order biological behavior is governed solely by the nonlinear growth term, which explicitly couples N and P. While the specifics of this result depends on the mathematical representation of the biological reaction terms, cross-diffusion in more complex biogeochemical models deserves further examination.

3.4 Discussion and Conclusions

It is well known that mesoscale and submesoscale processes impact phytoplankton variability (Flierl & McGillicuddy, 2002; Lévy et al., 2012; Mahadevan, 2016; McGillicuddy, 2016; Lévy et al., 2018). However, these scales are not resolved in most global climate models. While significant progress has been made in the parameterization of turbulent fluxes for ocean models (Gent et al., 1995; Visbeck et al., 1997; Fox-Kemper et al., 2008; D'Asaro et al., 2014), many sub-grid scale processes are still poorly represented (Hamlington et al., 2014; Smith et al., 2016; Fox-Kemper et al., 2019; Q. Li et al., 2019). Biogeochemical tracers pose an added challenge due to nonlinear reactions, which impact their distribution in addition to advection by the flow (Wallhead et al., 2013). Our goal in this study has been to examine the theoretical limitations of eddy diffusion parameterizations for reactive tracers such as nutrients and phytoplankton. Note that in the context of our simulations, eddy flux refers to the advective transport by the time fluctuating velocity rather than a parameterization of sub-grid scale processes. However, the multiple scale analysis from Section 3.2.1 is more general, and implies that cross-diffusion will also exist in the ensemble and coarse-grained problems.

We find that the efficacy of the parameterized eddy fluxes depends strongly on the ratio of biological and physical timescales, the Damköhler number. At low Da, gradient-diffusion is accurate since the reaction rates are slow enough that the scalar is approximately non-reactive. At high Da, the scalar is reacting faster than diffusion can act on it, so the gradient seen by the turbulence is small. The tracer evolution is primarily governed by the biological reactions, which explicitly couple N and P. Consequently, cross-diffusion can be important in these regimes. At intermediate Da, the tracers are reacting on the same timescales as the background flow, so changes in tracer concentration result from a complex combination of stirring and growth. As a result, the covariance of u' and P', which determines the phytoplankton flux, is not well represented in terms of the mean fields. The parameterization fails in these regimes, regardless of whether cross-diffusion is included. This is not surprising, since $Da \sim \mathcal{O}(1)$ violates the

timescale separation condition needed to derive (3.7) and (3.8)

Previous studies have proposed an effective diffusivity that varies as a function of the reaction rate (Plumb, 1979; Pasquero, 2005). However, even simple biogeochemical models, such as the one used in this study, can have multiple reaction timescales whose relative magnitudes affect the equilibrium behavior. Furthermore, the reaction-dependent effective diffusivity in Pasquero (2005) was found to be least accurate when $Da \sim \mathcal{O}(1)$. We suggest this is due to the lack of timescale separation rendering the flux-gradient formulation invalid. When the flow and reaction timescales are similar, it may be difficult to improve the accuracy of parameterized fluxes within the eddy diffusion framework, even if modified to account for the reaction timescale as in Pasquero (2005). This result has implications for coarse resolution climate models, since $Da \sim \mathcal{O}(1)$ approximately applies to phytoplankton growth and loss processes at the submesoscale (Smith, 2017). Therefore, there may be large errors associated with applying gradient diffusion to parameterize eddy fluxes of phytoplankton at the submesoscale.

In large *Da* regimes, we find that the eddy fluxes of *P* can depend strongly on gradients in *N* due to the coupling between the phytoplankton and nutrient evolution equations via biological reaction terms. Incorporating cross-diffusion in our idealized simulations greatly increased the accuracy of the parameterized fluxes when $Da \gg 1$. This is significant since $Da \sim \mathcal{O}(10^2)$ roughly applies to phytoplankton processes at the mesoscale (Smith, 2017). Therefore, including cross-terms in complex models may provide a way to improve the parameterized fluxes of phytoplankton at the mesoscale using information about the large scales only. We note though that any eddy parameterization which assumes locality in space and time is missing fundamental physical effects. As was shown in Manucharyan et al. (2017), the large-scale eddy field has a finite memory of past ocean states. Recent efforts have also incorporated non-local effects into eddy parameterizations using an effective diffusivity kernel that depends on the statistics of the flow field (Bhamidipati et al., 2020). Extending these frameworks to reactive tracers is worth investigation given the key role of phytoplankton in marine ecosystems and the global carbon cycle.

3.5 Acknowledgments

Thanks to Dhruv Balwada, Anand Gnanadesikan and an anonymous reviewer for helpful comments. Thanks also to Mara Freilich for useful conversations. This work was conducted, in part, at the 2019 Geophysical Fluid Dynamics Program at Woods Hole Oceanographic Institution, which is supported by the National Science Foundation and Office of Naval Research. C.J. Prend was also supported by a NSF Graduate Research Fellowship under Grant DGE-1650112. G. R. Flierl was supported by NSF grant OCE-1459702. K. M. Smith was supported by the European Research Council under the European Union's Horizon 2020 research and innovation Grant 742480. A. K. Kaminski was supported by NSF grant OCE-1657676. The code to run the coupled physical-biological model used in this study can be found at `http://doi.org/10.5281/zenodo.4067095`.

Chapter Three, in full, is a reprint of the material as it appears in Geophysical Research Letters, 2021. Prend, C. J., G. R. Flierl, K. M. Smith, and A. K. Kaminski (2021), Parameterizing eddy transport of biogeochemical tracers, *Geophysical Research Letters*, 48, e2021GL094405.
 The dissertation author was the primary investigator and author of this paper.

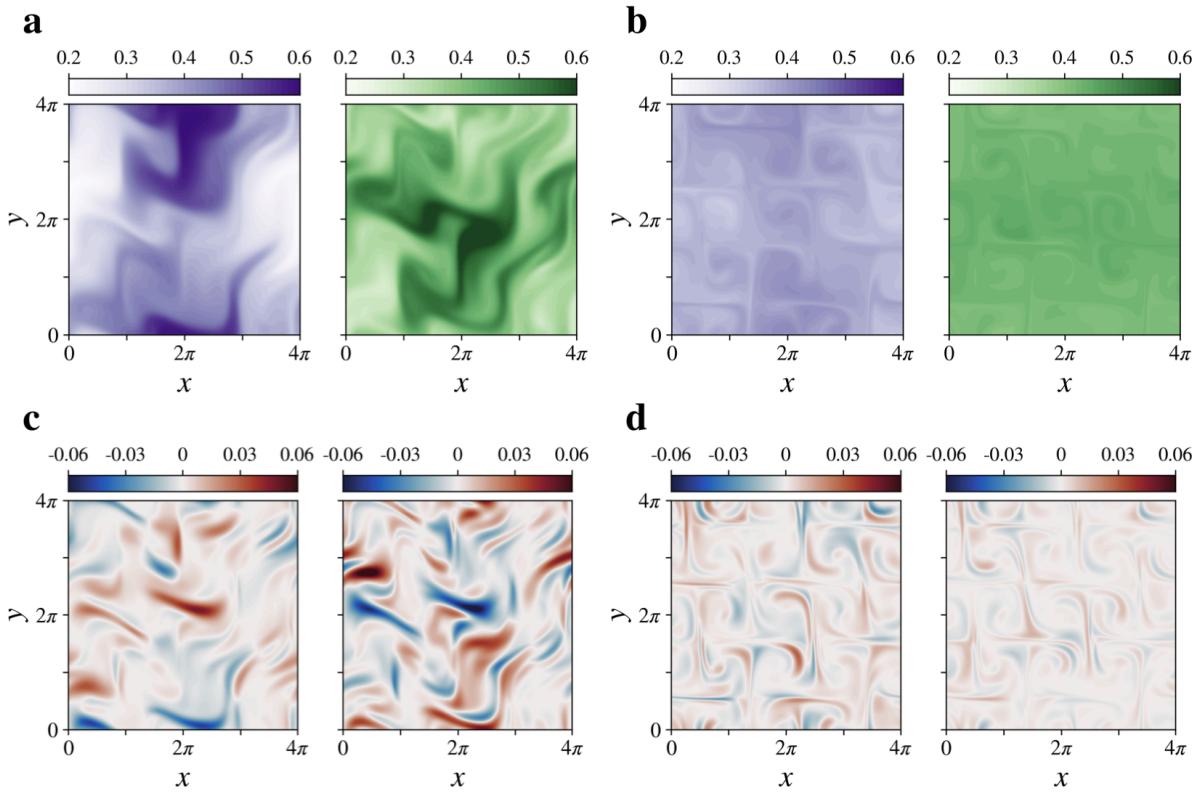

Figure 3.1. Snapshot at t=1000 of nutrient (purples) and phytoplankton (greens) concentrations (a,b) as well as nutrient (left) and phytoplankton (right) eddy fluxes (c,d) for two simulations with the same flow field but varied reaction rates, (a,c) λ=0.03, $\langle\mu\rangle$=0.08, Da=1 and (b,d) λ=0.003, $\langle\mu\rangle$=0.008, Da=0.1.

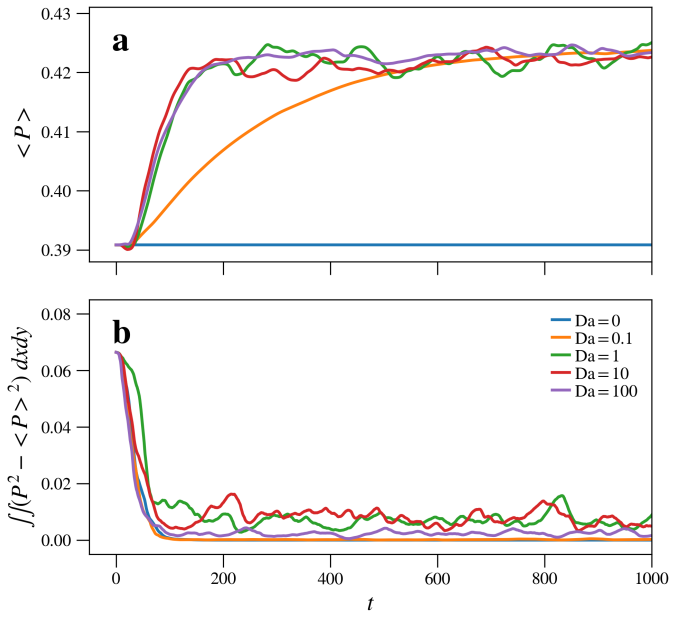

Figure 3.2. Time series of (a) mean phytoplankton concentration, and (b) phytoplankton concentration variance integrated over the domain. Plotted for five simulations with the same initial conditions and flow field but varied Da.

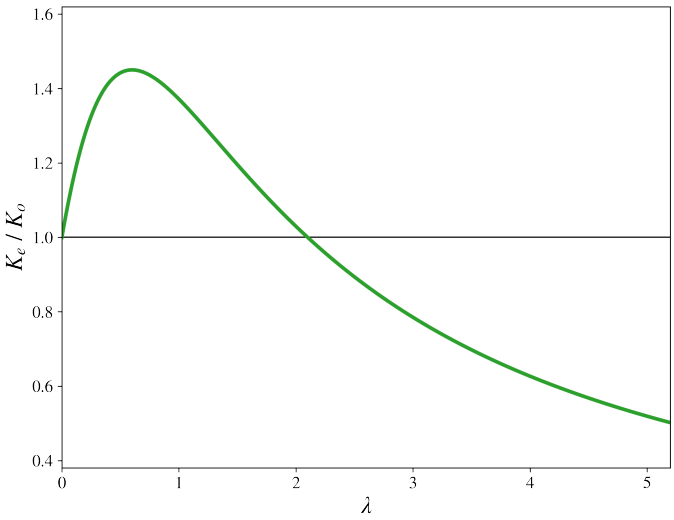

Figure 3.3. Effective diffusivity, K_e, for reactive tracer S ($S = N + P$) normalized by the effective diffusivity of a passive tracer subject to the same flow field, K_0, and plotted as a function of the entrainment rate, λ.

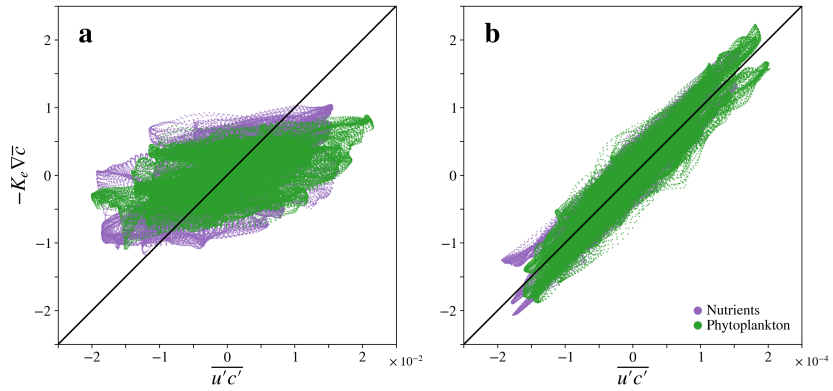

Figure 3.4. (a) Calculated eddy fluxes of N (purple) and P (green) from $\nabla\overline{c}$ and least squares fitted K_e versus the diagnosed eddy fluxes at each grid cell for a simulation with biological reaction terms (λ=0.03, $\langle\mu\rangle$=0.08), and (b) for the same initial conditions but with reaction rates λ and $\langle\mu\rangle$ set to 0 (i.e. N and P are non-reactive tracers).

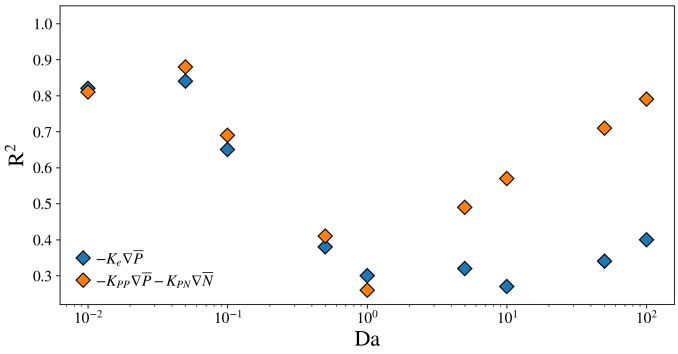

Figure 3.5. R^2 of the parameterized eddy flux and true eddy flux as a function of Da assuming $\overline{u'P'}=-K_e\nabla\overline{P}$ (blue) and $\overline{u'P'}=-K_{PP}\nabla\overline{P}-K_{PN}\nabla\overline{N}$ (orange).

3.6 Supplementary Material

The Supplementary Material provides details of the multiple scale analysis discussed in Section 3.2.1 of the main text (Section 3.6.1). We also discuss the dependence of the effective diffusivity on the reaction rate (Section 3.6.2) and further describe the relationship K_{PP}/K_{PN} (Section 3.6.3) mentioned in Section 3.3 of the main text.

3.6.1 Multiple Scale Analysis

As described in the main text, the perturbation expansions (3.5 - 3.6), are substituted into the advection-diffusion-reaction equations governing the nutrient (3.2) and phytoplankton (3.3) concentration fields. The zeroth order solution is given by:

$$\mathscr{O}(1): P_{0t} + (\mathbf{U}+\mathbf{u}')\cdot\nabla_{\mathbf{x}}P_0 - \kappa\nabla_{\mathbf{x}}^2 P_0 = \mu P_0 N_0 - \lambda P_0, \tag{3.10}$$

$$\mathscr{O}(1): N_{0t} + (\mathbf{U}+\mathbf{u}')\cdot\nabla_{\mathbf{x}}N_0 - \kappa\nabla_{\mathbf{x}}^2 N_0 = -\mu P_0 N_0 - \lambda N_0 + \lambda N_D. \tag{3.11}$$

Averaging over small and fast scales gives $0 = \mu P_0 N_0 - \lambda P_0$ for (3.2), which implies that $N_0 = \lambda/\mu$ and thus $P_0 = N_D - \lambda/\mu$ by (3.3).

The first order solution is:

$$\mathscr{O}(\varepsilon): P_{1t} + (\mathbf{U}+\mathbf{u}')\cdot\nabla_{\mathbf{x}}P_1 - \kappa\nabla_{\mathbf{x}}^2 P_1 + P_{0T} + (\mathbf{U}+\mathbf{u}')\cdot\nabla_{\mathbf{X}}P_0 = \mu P_0 N_1 + \mu P_1 N_0 - \lambda P_1, \tag{3.12}$$

$$\mathscr{O}(\varepsilon): N_{1t} + (\mathbf{U}+\mathbf{u}')\cdot\nabla_{\mathbf{x}}N_1 - \kappa\nabla_{\mathbf{x}}^2 N_1 + N_{0T} + (\mathbf{U}+\mathbf{u}')\cdot\nabla_{\mathbf{X}}N_0 = -\mu P_0 N_1 - \mu P_1 N_0 - \lambda N_1. \tag{3.13}$$

We now decompose P_1 and N_1 into mean and fluctuating components where the mean is a function of slow time and space variables only, i.e. $P_1 = \overline{P}_1(\mathbf{X},T) + P_1'(\mathbf{x},t,\mathbf{X},T)$. Averaging

over small and fast scales gives:

$$P_{0T} + \mathbf{U} \cdot \nabla_{\mathbf{X}} P_0 = \mu P_0 \overline{N}_1 + \mu \overline{P}_1 N_0 - \lambda \overline{P}_1 \tag{3.14}$$

Subtracting (3.12) from (3.10) gives an expression for the fluctuating parts, P_1' and N_1'.

$$(\partial_t + (\mathbf{U} + \mathbf{u}') \cdot \nabla_{\mathbf{x}} - \kappa \nabla_{\mathbf{x}}^2) \begin{bmatrix} P_1' \\ N_1' \end{bmatrix} - \mathscr{B} \begin{bmatrix} P_1' \\ N_1' \end{bmatrix} = -\mathbf{u}' \cdot \nabla_{\mathbf{X}} \begin{bmatrix} P_0 \\ N_0 \end{bmatrix}, \tag{3.15}$$

where $\mathscr{B}$ is $\begin{bmatrix} \mu N_0 - \lambda & \mu P_0 \\ -\mu N_0 & -\mu P_0 - \lambda \end{bmatrix}$. Solutions to (3.13) can be written in the form:

$$\begin{bmatrix} P_1' \\ N_1' \end{bmatrix} = -\int dt' \mathrm{e}^{-\mathscr{B}(t-t')} (\xi \cdot \nabla_{\mathbf{X}}) \begin{bmatrix} P_0 \\ N_0 \end{bmatrix}, \tag{3.16}$$

where $\xi(\mathbf{x}, t)$ resembles a particle displacement and satisfies the equation

$$\xi_t + (\mathbf{U} + \mathbf{u}') \cdot \nabla_{\mathbf{x}} \xi - \kappa \nabla_{\mathbf{x}}^2 \xi = \mathbf{u}' \delta(t - t') \tag{3.17}$$

The second order solution is:

$$\mathscr{O}(\varepsilon^2) : P_{2t} + (\mathbf{U} + \mathbf{u}') \cdot \nabla_{\mathbf{x}} P_2 - \kappa \nabla_{\mathbf{x}}^2 P_2 + P_{1T} + (\mathbf{U} + \mathbf{u}') \cdot \nabla_{\mathbf{X}} P_1 - 2\kappa \nabla_{\mathbf{x}} \cdot \nabla_{\mathbf{X}} P_1 - \kappa \nabla_{\mathbf{X}}^2 P_0 = \mu P_0 N_2 + \mu P_2 N_0 - \lambda P_2 + \mu P_1 N_1 \tag{3.18}$$

$$\mathscr{O}(\varepsilon^2) : N_{2t} + (\mathbf{U} + \mathbf{u}') \cdot \nabla_{\mathbf{x}} N_2 - \kappa \nabla_{\mathbf{x}}^2 N_2 + N_{1T} + (\mathbf{U} + \mathbf{u}') \cdot \nabla_{\mathbf{X}} N_1 - 2\kappa \nabla_{\mathbf{x}} \cdot \nabla_{\mathbf{X}} N_1 - \kappa \nabla_{\mathbf{X}}^2 N_0 = -\mu P_0 N_2 - \mu P_2 N_0 - \lambda P_2 - \mu P_1 N_1 \tag{3.19}$$

Averaging over small and fast scales gives the solvability condition:

$$\overline{P}_{1T} + (\mathbf{U} + \mathbf{u}') \cdot \nabla_{\mathbf{X}} \overline{P}_1 - \kappa \nabla^2_{\mathbf{X}} P_0 = \mu P_0 \overline{N}_2 + \mu \overline{P}_2 N_0 - \lambda \overline{P}_2 + \mu \overline{P_1 N_1} \tag{3.20}$$

Summing over our results at $\mathscr{O}(1)$, $\mathscr{O}(\varepsilon)$, and $\mathscr{O}(\varepsilon^2)$ gives:

$$\overline{P}_T + \mathbf{U} \cdot \nabla_{\mathbf{X}} \overline{P} - \kappa \cdot \nabla^2_{\mathbf{X}} \overline{P} + \overline{\mathbf{u}' \cdot \nabla_{\mathbf{X}} P'} = \mu \overline{P} \overline{N} - \lambda \overline{P} + \overline{\mu P' N'} \tag{3.21}$$

We can see that the evolution of the mean tracer concentration depends on the divergence of the eddy flux. Furthermore, (3.14) suggests that the eddy fluxes can be expressed as:

$$\overline{u'c'} = -\int d\mathbf{x}' dt' \; \mathrm{e}^{-\mathscr{B}(t-t')} \overline{u'(\mathbf{x},t) \xi(\mathbf{x}',t')} \nabla_{\mathbf{X}} \begin{bmatrix} \overline{P} \\ \overline{N} \end{bmatrix} \tag{3.22}$$

where c is the set of reactive tracers N and P. Note that the eddy fluxes of N and P depend on the large-scale gradients in both tracers, implying the form (3.7) and (3.8) given in the main text.

If we assume that there are no gradients in the nutrients, and let $u', P, N' = \hat{u}, \hat{P}, \hat{N} \cdot \mathrm{e}^{i\omega t}$, then the first order solution gives

$$i\omega \hat{P} - \mu \left(N_D - \frac{\lambda}{\mu} \right) \hat{N} = -\hat{u} \frac{\partial P_0}{\partial x} \tag{3.23}$$

$$-\lambda \hat{P} = (i\omega + \mu N_D) \hat{N} \rightarrow \hat{P} = -\frac{i\omega + \mu N_D}{\lambda} \hat{N} \tag{3.24}$$

so for N'

$$i\omega \hat{P} - \mu \left(N_D - \frac{\lambda}{\mu} \right) \hat{N} = -\hat{u} \frac{\partial N_D}{\partial x} \tag{3.25}$$

$$\left(\frac{-\omega^2 + i\omega \mu N_D}{\lambda} - \mu \left(N_D - \frac{\lambda}{\mu} \right) \right) \hat{N} = -\hat{u} \frac{\partial P_0}{\partial x} \tag{3.26}$$

$$\hat{N} = \frac{\hat{u}}{\frac{\omega^2}{\lambda} + \mu N_D - \lambda + i\omega\mu\frac{N_D}{\lambda}} \frac{\partial P_0}{\partial x} \tag{3.27}$$

When ω is either much bigger or much less than the reaction rates, the perturbation terms tend to be more in phase with the current. This likely explains, in part, the breakdown of the parameterization when $Da = 1$.

3.6.2 Effective Diffusivity

Given the impact of biological reactions on the equilibrium behavior of N and P, we might anticipate that they also affect the eddy diffusion coefficient. To demonstrate this simply, we can consider the total nitrogen in the system ($S = N + P$), whose evolution equation is found by summing together (3.2) and (3.3). The tracer S has the advantage of being governed by a single reaction rate, λ, since the opposite signed nutrient uptake terms in the N and P equations cancel. In a periodic flow field, the effective diffusivity for S, K_e, can be expressed as a function of λ. This is shown in Figure 3.3, after being scaled by the eddy diffusivity for a passive tracer subject to the same flow field (K_0). For most values of λ, the effective diffusivity of a reactive tracer is smaller than that for a passive tracer. This is because for large λ, the tracer decays faster than diffusion can act on it so the gradient seen by the turbulence is small. However, this result should not be generalized; for some small λ values in Figure 3.3, K_e is larger than K_0. Ultimately, K_e/K_0 depends on the form of the biological reaction terms, as well as the reaction rates and flow.

3.6.3 Ratio of Cross Fluxes

We can solve for the effective diffusivities in (3.7- 3.8) by exploiting the eddy flux of $S = N + P$, which is simpler since it has no nonlinear reaction terms.

$$\overline{u'S'} = -K^{\lambda}\nabla\bar{S} \tag{3.28}$$

$$\overline{u'P'} + \overline{u'N'} = -K^{\lambda}(\nabla\bar{P} + \nabla\bar{N}) \tag{3.29}$$

We find that

$$\overline{u'P'} = -\underbrace{\frac{\mu\bar{P}K^{\lambda} - \lambda K^{\mu\bar{P}}}{\mu\bar{P} - \lambda}}_{K_{PP}}\nabla\bar{P} - \underbrace{\frac{\mu\bar{P}(K^{\lambda} - K^{\mu\bar{P}})}{\mu\bar{P} - \lambda}}_{K_{PN}}\nabla\bar{N} \tag{3.30}$$

$$\overline{u'N'} = -\underbrace{\frac{\lambda(K^{\mu\bar{P}} - K^{\lambda})}{\mu\bar{P} - \lambda}}_{K_{NP}}\nabla\bar{P} - \underbrace{\frac{\mu\bar{P}K^{\mu\bar{P}} - \lambda K^{\lambda}}{\mu\bar{P} - \lambda}}_{K_{NN}}\nabla\bar{N} \tag{3.31}$$

Using these expressions for the diffusivities we can take the ratio K_{PP}/K_{PN}, whose magnitude is determined by the nondimensional parameter $\lambda/\mu\bar{P}$. This parameter can be related to the ratio of reaction rates by substituting the leading order solution for P from the multiple scale analysis ($P_0 = N_D - \lambda/\mu$). We find that,

$$\frac{K_{PP}}{K_{PN}} \propto \frac{\lambda}{\mu\bar{P}} \sim \frac{1}{\frac{\mu N_D}{\lambda} - 1}. \tag{3.32}$$

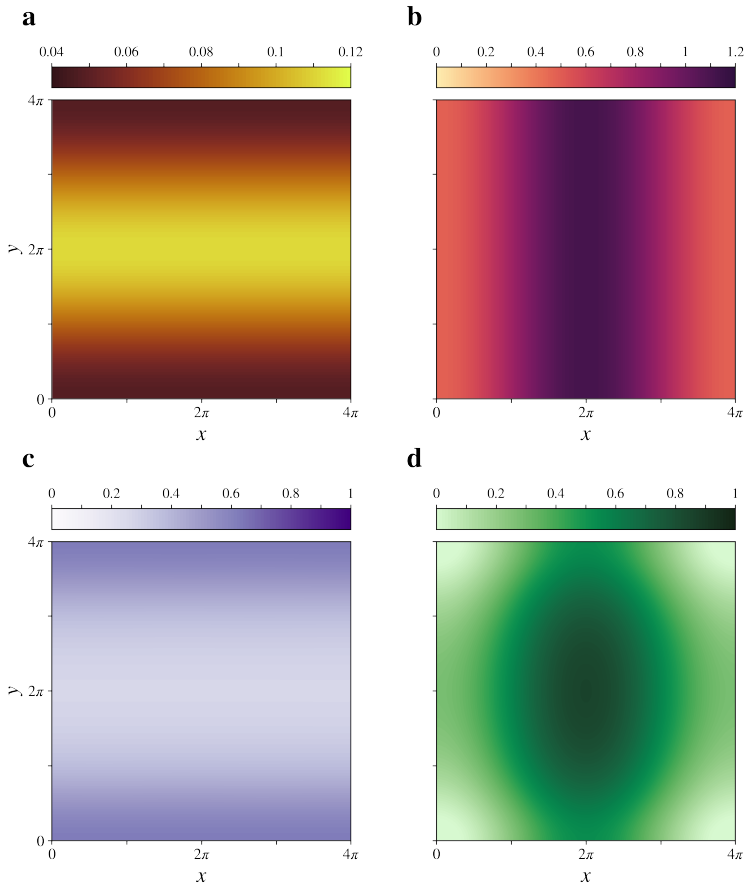

Figure 3.6. (a) μ distribution, modeled as $\mu_0 + \mu_1 \cos(y/2)$ (b) Initial condition for total nitrogen ($S = N + P$), modeled as $S_0 + S_1 \cos(x/2)$ (c) Initial condition for N, taken to be $S_i - P_i$ (d) Initial condition for P, taken to be $N_D - \lambda/\mu$, from the leading order solution for P in the multiple scale analysis.

Chapter 4

Indo-Pacific sector dominates Southern Ocean carbon outgassing

Abstract

The Southern Ocean modulates the climate system by exchanging heat and carbon dioxide (CO_2) between the atmosphere and deep ocean. While this region plays an outsized role in the global oceanic anthropogenic carbon uptake, CO_2 is also released into the atmosphere across large swaths of the Antarctic Circumpolar Current (ACC). Southern Ocean outgassing has long been attributed to remineralized carbon from upwelled deep water, but the precise mechanisms by which this water reaches the surface are not well constrained from observations. Using data from a novel array of autonomous biogeochemical profiling floats, we estimate Southern Ocean air–sea CO_2 fluxes at unprecedented spatial resolution and determine the pathways that transfer carbon from the ocean interior into the mixed layer where air–sea exchange occurs. Float-based flux estimates suggest that carbon outgassing occurs predominantly in the Indo-Pacific sector of the ACC due to variations in the mean surface ocean partial pressure of CO_2 (pCO_2). We show that this zonal asymmetry in surface pCO_2 and consequently air–sea carbon fluxes stems primarily from regional variability in the mixed-layer entrainment of upwelled carbon-rich deep water. These results suggest that long-term trends of the Southern Ocean carbon sink inferred from sparse shipboard data may depend on the fraction of measurements from each basin in a given year. Furthermore, sampling these different air–sea flux regimes is necessary to monitor

future changes in oceanic carbon release and uptake.

4.1 Introduction

The Southern Ocean accounts for a disproportionately large percentage of the total oceanic anthropogenic carbon uptake, which results from the region's unique role in the global overturning circulation (Khatiwala et al., 2009; Frölicher et al., 2015). In the southern portion of the Antarctic Circumpolar Current (ACC), deep water returns to the upper ocean via wind-driven upwelling and is transformed into northward-flowing intermediate and bottom waters (J. Marshall & Speer, 2012). These upwelled deep waters have been isolated from the atmosphere since pre-industrial times, and thus are poised to both absorb anthropogenic CO_2 and release natural carbon that has accumulated over centuries through the remineralization of organic matter (Lovenduski et al., 2008). The net air–sea carbon exchange in the Southern Ocean is, therefore, a balance between these opposing processes (DeVries et al., 2017; Gruber et al., 2019).

Both uptake of anthropogenic CO_2 and outgassing of natural carbon are fundamentally tied to the physical transport of water between the surface mixed layer and ocean interior. While the circulation of the Southern Ocean has often been described in a zonally-averaged framework (J. Marshall & Speer, 2012), recent work has highlighted significant regional differences in upwelling, mixed-layer dynamics, and their response to climate variability (Sallée et al., 2010; Viglione & Thompson, 2016; Tamsitt et al., 2017; Rintoul, 2018). These zonal variations in the circulation and surface forcing, in turn, impact air–sea heat and carbon exchange (Tamsitt et al., 2016; Keppler & Landschützer, 2019). For example, observation-based estimates and modeling studies suggest that subduction and storage of anthropogenic carbon are highly localized (Sallée et al., 2012; Bopp et al., 2015). Less attention has been paid to the zonal structure of carbon outgassing, in part, because it occurs primarily in winter when observations are difficult to obtain (Gray et al., 2018).

Starting in 2014, autonomous biogeochemical profiling floats have been deployed as part

of the Southern Ocean Carbon and Climate Observations and Modeling (SOCCOM) project (Talley et al., 2019). The SOCCOM float array was developed to increase the number and distribution of year-round subsurface biogeochemical measurements because of the known importance of the Southern Ocean to the global carbon cycle and the weaknesses of Earth System Models (ESMs) in this region (Frölicher et al., 2015; Russell et al., 2018; Beadling et al., 2020). In situ observations provide an important constraint on climate models, which disagree significantly on the magnitude and variability of Southern Ocean air–sea carbon fluxes (F_{CO_2}) (Anav et al., 2013; Mongwe et al., 2018). Indeed, the net Southern Ocean carbon uptake is a major source of uncertainty in the global carbon budget (Le Quéré et al., 2013; Friedlingstein et al., 2020), and current observation-based estimates rely mainly on sparse surface pCO_2 measurements, which are extended using innovative mapping techniques (Rödenbeck et al., 2013; Landschützer et al., 2015; Keppler & Landschützer, 2019).

Based on the first several years of limited SOCCOM data, Gray et al. (2018) showed a surprisingly large outgassing signal in the southern ACC. Bushinsky et al. (2019) used the growing float record to directly compare SOCCOM-derived fluxes with ship-based fluxes mapped using a neural network (Landschützer et al., 2015) and the Jena CarboScope method (Rödenbeck et al., 2013), as well as the Biogeochemical Southern Ocean State Estimate (B-SOSE) (Verdy & Mazloff, 2017) and an ESM. Bushinsky et al. (2019) similarly showed a higher outgassing in the ACC with the inclusion of SOCCOM float data, in part due to the seasonal bias in ship-based products. These previous analyses have focused on the net Southern Ocean carbon uptake and zonally-averaged fluxes, but significant spatial variability in F_{CO_2} has begun to emerge with increasing float coverage. Here, we use data from nearly 200 SOCCOM floats to extend the float-based F_{CO_2} time series and investigate zonal variations in air-sea carbon exchange as well as the subsurface processes that contribute to these patterns.

We show that carbon outgassing within the ACC occurs preferentially in the Indo-Pacific sector due to a higher annual mean surface ocean pCO_2. This basin asymmetry could potentially result from regional variability in deep water carbon content, mixed-layer entrainment, wind

forcing, and/or biological productivity. We assess the relative importance of these mechanisms using the subsurface float data, in combination with several other observational datasets. We find that the inter-basin variation in surface ocean pCO_2 is primarily driven by patterns in obduction of carbon-rich deep water. Namely, we show that zonal asymmetry in the mixed-layer depth (MLD) distribution leads to systematic differences between basins in the fraction of upwelled carbon-rich water that is entrained into the surface mixed layer. Variations in the flux of carbon across the mixed-layer base alone could explain the observed asymmetry in CO_2 outgassing. While MLD is used as a predictor variable in many air–sea carbon flux products (Rödenbeck et al., 2013; Bushinsky et al., 2019), our results provide a direct observational link between the spatial patterns of MLD and F_{CO_2} in the Southern Ocean, which can inform future work investigating model biases.

4.2 Data and Methods

4.2.1 Observational Datasets

This study uses in situ data from autonomous biogeochemical floats deployed by the SOCCOM project. SOCCOM floats measure temperature, salinity, pressure, dissolved oxygen, nitrate, pH, fluorescence, and backscatter over the top 2,000 m of the water column every 10 days (Riser et al., 2018). The quality-controlled data from the August 30, 2020 SOCCOM snapshot are used in this analysis and are publicly available (http://doi.org/10.6075/J0BK19W5). Floats sample unevenly in the vertical, so all profiles are linearly interpolated onto a regular depth axis with 5 m resolution in the upper 500 m, 10 m resolution from 500-1000 m, 50 m resolution from 1000-1500 m, and 100 m resolution 1500-2000 m. The SOCCOM snapshots include estimates of total alkalinity (TA) from a locally-interpolated alkalinity regression (Carter et al., 2017) and pCO_2 calculated from the alkalinity and in situ pH (Williams et al., 2017). We also compute the potential pCO_2 (PCO_2), which is the pCO_2 a water parcel would have if it were raised to the surface adiabatically (Broecker & Peng, 1982; Skinner et al., 2010; Chen et al., submitted), from

alkalinity and pH, as well as temperature, salinity, and pressure using the CO_2 System Calculator (CO2SYS) (Humphreys et al., 2020).

Additionally, we use data from the full Argo array (Roemmich et al., 2019) up to August 30, 2020 to calculate mixed-layer depth using a 0.03 kg/m^3 density threshold (Dong et al., 2008). A monthly MLD climatology is developed by mapping all available Argo MLD estimates onto a $1^\circ \times 1^\circ$ grid using Gaussian process regression (Kuusela & Stein, 2018). Monthly composites of wind stress from the ERA5 reanalysis product (Hersbach et al., 2020) and absolute geostrophic velocity derived from Argo data (Gray & Riser, 2014) are interpolated onto the same grid to calculate the components of the entrainment rate at monthly resolution (described further in Section 4.2.3 below). Finally, the mean ACC frontal positions from Kim and Orsi (2014) are used to sort profiles into the Polar Frontal Zone (PFZ) and Antarctic Southern Zone (ASZ). Results are not sensitive to the precise frontal definitions, which were tested by repeating the analysis with fronts determined from the Orsi et al. (1995) temperature and salinity criteria (Gray et al., 2018) and with zones sorted by an unsupervised machine learning classification method (Rosso et al., 2020). We also repeated the analysis using MLD defined by a hybrid algorithm (Holte & Talley, 2009), which did not change the results significantly (not shown).

4.2.2 Air–sea Carbon Flux Estimates

Air–sea carbon fluxes are estimated from the profiling float data using the bulk formula (Wanninkhof, 2014; Gray et al., 2018)

$$\mathrm{F}_{\mathrm{CO}_2} = kK_0(p\mathrm{CO}_2^{\mathrm{ocn}} - p\mathrm{CO}_2^{\mathrm{atm}})(1 - \mathrm{SIC}), \tag{4.1}$$

where k is the gas transfer velocity, which is parameterized in terms of the wind speed (Ho et al., 2006; Wanninkhof, 2014) and calculated from ERA5 winds (Hersbach et al., 2020). K_0, the solubility of CO_2 in seawater, depends on temperature and salinity (Weiss, 1974). The surface ocean $p\mathrm{CO}_2$ ($p\mathrm{CO}_2^{\mathrm{ocn}}$) is derived from float pH and empirically estimated alkalinity, as described

previously. Measurements of the mole fraction of CO_2 in dry air taken at Cape Grim Observatory (http://www.csiro.au/greenhouse-gases) are utilized to estimate atmospheric pCO_2 (pCO_2^{atm}) using the sea level pressure at the float locations from ERA5 and correcting for water vapor pressure (Zeebe & Wolf-Gladrow, 2001). In principle, atmospheric data from Baring Head or South Pole stations could be used to estimate pCO_2^{atm} for the Southern Ocean. However, from 2014-2020, the average monthly difference in mole fraction of CO_2 is 0.10 ppm between Cape Grim and Baring Head stations, and 0.25 ppm between Cape Grim and South Pole stations. These differences are small compared to the uncertainty associated with estimating surface ocean pCO_2 from in situ pH (Williams et al., 2017). The sea ice concentration (SIC) along each float trajectory is found from daily satellite sea ice extent (Meier et al., 2017). The uncertainty in F_{CO_2} for each float is derived from the uncertainties in each term of Equation 4.1 using a Monte Carlo simulation. Further details of the air–sea flux calculation and uncertainty estimates are provided in a past study (Gray et al., 2018).

4.2.3 Obduction Calculation

To assess the mechanisms that transport subsurface carbon from the permanent pycnocline into the mixed-layer, we calculate the obduction fluxes of PCO_2. First, we note that transfer of fluid into and out of the mixed layer is controlled by changes in the MLD with time, vertical Ekman pumping, and lateral induction (Qiu & Huang, 1995). The instantaneous entrainment rate (E) is the sum of these processes

$$E = \frac{\partial h}{\partial t} + \mathbf{u}_h \cdot \nabla_H h + w_h, \tag{4.2}$$

where h is the mixed-layer depth, $\mathbf{u}_h$ and w_h are the lateral and vertical velocities at the base of the mixed layer, respectively, and ∇_H is the horizontal divergence operator (Qiu & Huang, 1995). The terms represent from left to right, the temporal MLD variability, lateral induction associated with horizontal advection of the MLD, and vertical advection. Here we estimate the entrainment

components at monthly resolution using mapped Argo MLD to calculate the temporal and lateral MLD gradients using a central finite difference method. For lateral induction, the horizontal velocity is taken to be the absolute geostrophic velocity (from an Argo-based data product described in Section 4.2.1) at the depth level closest to the MLD at a given location and month. Vertical velocity is assumed to be dominated by the wind-driven Ekman pumping velocity (Liu & Huang, 2012), which is calculated from monthly composites of ERA5 wind stress.

Given the strong seasonal cycle of MLD, entrainment occurs during the months when the mixed layer deepens. For much of this time, water is entrained from the seasonal pycnocline, which was in contact with the atmosphere in the previous year. The entrainment of water from the permanent pycnocline, which occurs only in late winter near the end of the mixed-layer deepening period, is referred to as obduction (Qiu & Huang, 1995). Water in the permanent pycnocline has been isolated from the atmosphere on long timescales, so obduction is responsible for the transport of upwelled carbon-rich deep water into the mixed layer where it can outgas. The annual mean obduction rate is defined as the instantaneous entrainment rate integrated over the obduction period (Liu & Huang, 2012), taken here to be the 2 months before the maximum winter MLD is reached at a given location (D. Marshall & Marshall, 1995).

To determine the carbon transport associated with each component of obduction, consider the tracer evolution equation integrated over the surface mixed layer,

$$\frac{\partial C_m}{\partial t} = -\mathbf{u}_m \cdot \nabla_H C_m + \kappa_H \nabla_H^2 C_m - \frac{\kappa_z}{h} \frac{\partial C}{\partial z}\bigg|_{z=h} + \left(\frac{C_h - C_m}{h}\right)\left(\frac{\partial h}{\partial t} + \mathbf{u}_h \cdot \nabla_H h + w_h\right) + S_m, \quad (4.3)$$

where the subscript m represents averaged quantities in the mixed layer, while the subscript h represents the value of a quantity at the mixed-layer base; $\mathbf{u}$ is the horizontal velocity; κ_H and κ_z are the lateral and vertical diffusivities, respectively; and S represents the sources and sinks of carbon such as air–sea fluxes and biological processes. Changes in the mixed-layer carbon

content, C_m, are driven by the terms on the right-hand side of the equation. These are from left to right, lateral advection, lateral diffusion, vertical diffusion, entrainment, and the sum of the sources and sinks.

Mixed-layer carbon budgets are typically computed for dissolved inorganic carbon (DIC). However, DIC variability is only one component of surface ocean pCO_2 (Takahashi et al., 2002), which is the quantity relevant to air–sea fluxes. A budget for PCO_2 can be constructed by incorporating terms representing the dependence of surface pCO_2 on temperature, salinity, DIC, and TA. Here, we do not attempt to close a full budget, which is difficult from observations alone. Instead, our goal is to assess the relative size of vertical diffusion and the individual entrainment components, which are the only terms associated with physical transport of fluid from the ocean interior into the mixed layer. Framing the analysis in terms of PCO_2 allows us to directly quantify the impact of obduction on surface pCO_2. However, the calculation was repeated with DIC to ensure the conclusions remained unchanged.

For both PCO_2 and DIC, vertical diffusion is orders of magnitude smaller than entrainment across a range of diffusivities (10^{-4} to 10^{-5} m^2/s). While diffusion does not directly drive the changes in mixed-layer pCO_2, it still plays an important role in setting the vertical PCO_2 structure. To determine the annual mean change in mixed-layer pCO_2 due to obduction of subsurface PCO_2, we multiply the entrainment rate integrated over the obduction period by $(C_h - C_m)/h$, or the average PCO_2 difference between the mixed layer and 10 m below the MLD, computed for each float profile and then averaged over the obduction period. This isolates the surface pCO_2 variability due solely to the transfer of high PCO_2 water from the permanent pycnocline into the mixed layer, in other words, the signal related to the outcropping of upwelled deep water. The total uncertainty in the annual mean PCO_2 obduction flux was determined from the uncertainties in each component associated with obduction in Equation 4.3 using a Monte Carlo simulation with 5000 iterations for each frontal zone and basin. We also tested the sensitivity of the results to the length of the obduction period.

4.3 Results

4.3.1 Air–sea carbon flux variability

Float-based air–sea CO_2 flux estimates (Figure 4.1a) demonstrate significant spatial variability. Carbon outgassing, positive F_{CO_2} in this study, is widespread within the core of the ACC but occurs mostly in the Indian and Pacific sectors, between Kerguelen Plateau and Drake Passage. This basin asymmetry is also visible in the annual mean F_{CO_2} derived from an independent set of pCO_2 measurements (Figure 4.1b) (Landschützer et al., 2015). While the gas transfer velocity can greatly modify the flux magnitude, the sign is set only by the ΔpCO_2 (Equation 4.1). Atmospheric CO_2 in the Southern Hemisphere is well-mixed compared to oceanic pCO_2 (Takahashi et al., 1997). Therefore, the distribution of carbon uptake and outgassing is controlled by the surface ocean pCO_2, which in turn varies with temperature, salinity, DIC, and TA (Takahashi et al., 2014).

The components of surface pCO_2 variability exhibit complex spatial patterns, but distinct physical and biogeochemical regimes have been shown to coincide with the ACC frontal zones (Gray et al., 2018; Williams et al., 2018; Chapman et al., 2020). Here we sort float profiles based on the mean position of the ACC fronts (Kim & Orsi, 2014) (Figure 4.2a). Throughout the high-latitude Southern Ocean, south of the Subantarctic Front, pCO_2 seasonality is in phase with surface DIC changes (Takahashi et al., 2014). The seasonal cycle of F_{CO_2}, consequently, shows maximum outgassing in winter when DIC is highest due to respiration and entrainment of subsurface carbon during deep wintertime mixing (Gray et al., 2018; Williams et al., 2018). Most of the outgassing occurs within the PFZ and ASZ (Gray et al., 2018). However, the fluxes vary strongly with longitude. Monthly climatologies of F_{CO_2} for the PFZ and ASZ indicate significant differences between basins (Figure 4.2b,c). In the PFZ, outgassing in the Indian and Pacific is compensated by an almost equal magnitude carbon uptake in the Atlantic. Similarly, in the ASZ, outgassing per unit area is significantly higher in the Indo-Pacific compared to the Atlantic.

The variations in F_{CO_2} between basins within the ACC result from large disparities in

surface ocean pCO_2. The annual mean pCO_2 is higher in the Indo-Pacific than in the Atlantic by 36.7 ± 11.8 μatm in the PFZ and by 17.7 ± 11.1 μatm in the ASZ, where these uncertainties reflect both the variability within each region and the error associated with estimating pCO_2 from in situ pH (Williams et al., 2017). Although the mean pCO_2 differs substantially between basins, particularly in the PFZ, the amplitude of the seasonal cycle as well as the thermal and non-thermal components of pCO_2 variability are equivalent across sectors within each frontal zone. Thus, preferential outgassing in the Indo-Pacific must result from the processes that set the mean surface pCO_2 value, namely, the balance between physical transport of carbon to the mixed layer and biological drawdown (Bronselaer et al., 2018).

Ocean color data demonstrate that patterns of Southern Ocean primary productivity are complex (Figure 4.2a), and high production in the Atlantic sector likely contributes to the lower pCO_2 values (Arrigo et al., 2008). But while biology can be important locally, its effect is diminished when integrated over an entire basin; at large scales, physical transfers of carbon typically dominate over biological processes (Lévy & Martin, 2013). Estimates of annual net community production derived from float nitrate drawdown (Johnson et al., 2017a; von Berg et al., 2020) suggest that export production is higher in the Atlantic by 0.7 ± 1.4 mol C/m^2/yr in the PFZ and 0.4 ± 1.1 mol C/m^2/yr in the ASZ. This difference alone can only account for about 25% of the observed zonal asymmetry of F_{CO_2} within these frontal zones (3.1 and 1.6 mol C/m^2/yr in the PFZ and ASZ, respectively). Therefore, the distribution of mean pCO_2, and thus F_{CO_2}, is most likely related to regional variability in the vertical supply of carbon to the surface ocean.

4.3.2 Driving Mechanisms

Outgassing in the ACC is associated with Ekman-driven upwelling of carbon-rich deep waters (Lovenduski et al., 2008). However, the transfer of upwelled water into the mixed layer is not as well understood. While past studies have examined surface-to-interior exchange pathways of DIC in models (Lévy & Martin, 2013), many models poorly represent the Southern Ocean

MLD (Sallée et al., 2013). Consequently, the detailed mechanisms of carbon transport into the Southern Ocean mixed layer are not well constrained, particularly from observations. Recent work has shown that the subsurface PCO_2 maximum tracks closely with upwelling deep water isopycnal surfaces, providing the source for deep ocean CO_2 release (Chen et al., submitted). To isolate the impact of upwelled deep water on surface pCO_2, we consider the obduction flux of PCO_2, which quantifies the carbon entering the mixed layer from the permanent pycnocline and depends on the obduction rate (Figure 4.3) as well as the subsurface carbon content. PCO_2 values immediately below the mixed layer (Figure 4.4d-f) are largest in the Indian and Pacific sectors due to the comparatively older age of Indo-Pacific Deep Water, which allows for greater accumulation of remineralized carbon (Heinze et al., 2015; Keppler et al., 2020; Chen et al., submitted). This difference in deep water carbon content could contribute to the zonal asymmetry in surface pCO_2 when the water is entrained into the mixed layer. However, within the PFZ and ASZ, the inter-basin variation in PCO_2 at the mixed-layer base results primarily from the deeper winter MLDs in the Indo-Pacific, rather than the background PCO_2 profiles (Figure 4.5b,c). Therefore, connectivity between the surface and interior oceans likely varies between basins.

Indeed, there is significant zonal asymmetry in the annual mean obduction rate (Figure 4.3a), which is dominated by temporal changes in the MLD. Thus, regions of significant obduction (Figure 4.5a) correspond to locations with the deepest maximum MLDs (Figure 4.1c). Winter MLDs in the PFZ are roughly 100 m deeper in the Indo-Pacific compared to the Atlantic (Figure 4.4a-c). This difference in the MLD seasonal cycle amplitude leads to a larger MLD tendency and higher PCO_2 at the mixed-layer base during the obduction period in the Indo-Pacific. Both of these induce greater fluxes of PCO_2 into the mixed layer, as the entrainment flux depends on the obduction rate as well as the PCO_2 value of the water being entrained. This is why the strongest outgassing does not correspond to the highest obduction rates and deepest winter mixed layers, which occur in the Subantarctic Zone where carbon-rich isopycnals are too deep to be accessed by wintertime mixing. It should be noted that high-frequency entrainment events are not captured in this analysis, which uses a monthly climatology to calculate the temporal MLD

variability. Resolving shorter timescales across the entire Southern Ocean, although not possible from the current Argo data coverage, would likely increase the obduction fluxes of carbon in all basins (M. Freilich & Mahadevan, 2021). However, high-frequency processes, while important locally, may contribute less to the mean basin-scale differences that we focus on here (Lévy & Martin, 2013; Resplandy et al., 2019).

Ekman pumping accounts for only about 5-10% of the annual mean obduction rate, but it reinforces the zonal asymmetry in obduction fluxes of carbon (Figure 4.5d,e). Within the PFZ, there are systematic inter-basin variations in Ekman pumping resulting from a shift in the mean latitude range of the frontal zones due to topographic steering (Figure 4.4a-c). The meridional excursion of the flow downstream of Drake Passage causes ACC streamlines to be furthest north in the Atlantic and to spiral southward across the Indo-Pacific. Therefore, in the PFZ, the mean Ekman pumping velocity (Figure 4.1d) drives downwelling in the Atlantic and upwelling in the Indian and Pacific. While the Ekman pumping contribution to obduction is small relative to temporal changes in MLD, it plays an important role in setting the PCO_2 value below the MLD. In an abiotic ocean, the vertical PCO_2 structure in the interior results from a balance between the vertical velocity and diffusion (Ito & Follows, 2003). Ekman pumping and diffusion, therefore, increase the proximity of carbon-rich water to the base of the mixed layer, which is necessary for obduction to actually alter the surface pCO_2 value.

The final component of the obduction rate is lateral induction, which is associated with advection across horizontal MLD gradients. This term varies on small scales (Figure 4.3d). As found in previous studies, lateral induction leads to alternating hotspots of obduction and subduction along the path of the ACC that tend to compensate over large areas (Sallée et al., 2010; Lévy & Martin, 2013). Because of this compensation effect, the PCO_2 fluxes due to lateral induction are relatively small when averaged over an entire frontal zone and basin (Figure 4.5d,e). While lateral induction can be important on smaller scales and has been suggested to control the locations of anthropogenic carbon subduction (Sallée et al., 2012), its relationship to outgassing is less clear given the long air–sea equilibration timescale for CO_2, which is on the order of 6

months to a year (Jones et al., 2014).

Together, the components of obduction drive an annual change in mixed-layer pCO_2 in the PFZ of approximately 60.6 $\pm$ 18.1 μatm in the Indo-Pacific sector and 26.1 $\pm$ 13.0 μatm in the Atlantic sector (Figure 5d). The difference between these is roughly equal to the observed difference in annual mean surface pCO_2 between basins in the PFZ (36.7 μatm). In the ASZ, the annual change in mixed-layer pCO_2 due to obduction of subsurface PCO_2 is approximately 44.5 $\pm$ 15.7 μatm in the Indo-Pacific and 24.0 $\pm$ 14.2 μatm in the Atlantic (Figure 4.5e). Again, the difference between the basins is similar to the observed difference in mean surface pCO_2 in the ASZ (17.7 μatm). In other words, the inter-basin difference in pCO_2 can be explained almost entirely by regional variability in obduction, although the absolute pCO_2 values will also depend on biological processes and surface heat fluxes. This finding is supported by independent estimates of obduction rates (Liu & Huang, 2012) and Lagrangian mixed-layer outcropping events (Viglione & Thompson, 2016), which show the greatest interior-to-surface exchange in the Pacific sector of the Southern Ocean. Mixed-layer entrainment has been proposed to play a leading role in interannual variability of Southern Ocean carbon fluxes (Verdy et al., 2007), and here we suggest that it is also a key control on the zonal structure of F_{CO_2}.

4.4 Discussion and Conclusions

High carbon uptake in the temperate latitudes of the Southern Ocean is partially offset by outgassing of remineralized carbon from upwelled deep waters (Anderson et al., 2009). Future changes in the strength of the Southern Ocean carbon sink will depend on the trends in both anthropogenic carbon uptake and natural air–sea carbon exchange (Sarmiento et al., 1998; Gruber et al., 2019), which are not necessarily governed by the same mechanisms (Lovenduski et al., 2008; Ito et al., 2010). Here, we have used novel measurements from autonomous biogeochemical floats to estimate the distribution of Southern Ocean carbon uptake and outgassing. We find persistent differences in the surface ocean pCO_2 and air–sea carbon fluxes between basins within

the ACC. The preponderance of outgassing in the Indian and Pacific sectors of the Southern Ocean is linked primarily to zonal variations in the transport of upwelled deep water into the mixed layer. The obduction fluxes of carbon alone could generate the observed differences in mean surface pCO_2 between basins in both the PFZ and ASZ. These fluxes across the mixed-layer base depend on the obduction rate itself as well as the carbon content of the subsurface waters.

While autonomous floats have significantly increased the spatial and temporal coverage of biogeochemical data in the Southern Ocean, air–sea carbon fluxes exhibit variability across a wide range of scales (Gruber et al., 2019). The magnitude of net air–sea CO_2 exchange across the whole Southern Ocean is likely under-constrained by present-day float data (Monteiro et al., 2015; Bushinsky et al., 2019). Interannual variability is not well resolved either, since the SOCCOM float record only extends back to 2014. However, results do not seem to be influenced by seasonal biases in sampling within a given sector or by having observations heavily skewed towards one year in a particular basin. Furthermore, our aim here is not to investigate interannual variability, but rather the drivers of the basin-scale differences in mean pCO_2 and F_{CO_2}, which are also seen in observation-based products derived from independent, multi-decadal datasets (Takahashi et al., 2002; Landschützer et al., 2015). But as the number of float measurements increases, it will be possible to examine a range of timescales not considered in this analysis.

The inter-basin variation of Southern Ocean air–sea carbon fluxes suggests that decadal trends based on sparse shipboard data (Landschützer et al., 2015) must be interpreted within the context of measurement locations. Although upscaled ship-based F_{CO_2} products (Landschützer et al., 2015) exhibit zonal asymmetry in outgassing, the magnitude of net air–sea CO_2 exchange may still be strongly modified depending whether data were collected in the Indo-Pacific or in the Atlantic in a given year. Furthermore, the heterogeneity of obduction could lead to fundamental differences in how the sectors respond to climate variability. Historical observations from the Southern Ocean are biased to the Atlantic, which has the highest uptake per unit area (Keppler & Landschützer, 2019). Lack of wintertime measurements and limited spatial sampling in the

Pacific sector of the ACC likely both lead to an underestimate of carbon outgassing.

Previous observational studies on the Southern Ocean carbon sink have relied primarily on surface pCO_2 measurements (Landschützer et al., 2015) or atmospheric inversions (Le Quéré et al., 2007). While a number of studies have used mixed-layer budgets to investigate air–sea carbon exchange (Sallée et al., 2012; Lévy & Martin, 2013; Rödenbeck et al., 2013; Bushinsky et al., 2019), the present work is the first to highlight and to mechanistically explain the inter-basin differences in Southern Ocean outgassing. Developing this mechanistic understanding requires information about the seasonal cycle and biogeochemical properties in the ocean interior, which is provided by unique year-round and subsurface data from autonomous floats. Our results suggest that obduction plays a leading role in the regional patterns of Southern Ocean air–sea carbon fluxes. However, many Earth System Models poorly represent the seasonal cycle of Southern Ocean MLD (Sallée et al., 2013), which likely leads to errors in the obduction fluxes of carbon. These inconsistencies in MLD may partly explain the large spread in modeled Southern Ocean carbon sink variability, although biases in F_{CO_2} can result from many factors (Mongwe et al., 2018). Greater knowledge of these processes through increased observations is necessary to improve the representation of the carbon cycle in models and predict the response of the ocean to climate change.

4.5 Acknowledgments

C. J. Prend was supported by a National Science Foundation Graduate Research Fellowship under Grant DGE-1650112. A. R. Gray, L. D. Talley, S. T. Gille, F. A. Haumann, K. S. Johnson, S. C. Riser, I. Rosso, J. Sauvé, and J. L. Sarmiento were supported by NSF PLR-1425989 and OPP-1936222. A. R. Gray acknowledges additional support through NSF award OCE-1756882. F. A. Haumann was also supported by the SNSF grant numbers P2EZP2_175162 and P400P2_186681. Biogeochemical profiling float data were collected and made freely available by the Southern Ocean Carbon and Climate Observations and Modeling (SOCCOM) Project

(http://soccom.princeton.edu) funded by the National Science Foundation, Division of Polar Programs (NSF PLR-1425989), by NASA (NNX14AP49B), and by Argo and the NOAA programs that contribute to it. Data from the full Argo array were also used (http://argo.ucsd.edu/), as well as absolute geostrophic velocities derived from Argo data (http://alisonrgray.com/agva/), wind stress and sea level pressure from the ERA5 reanalysis product (http://www.ecmwf.int/en/forecasts/dataset/ecmwf-reanalysis-v5), and atmospheric CO_2 measurements from Cape Grim Observatory (http://www.csiro.au/greenhouse-gases).

Chapter Four, in full, has been submitted to Global Biogeochemical Cycles. Prend, C. J., A. R. Gray, L. D. Talley, S. T. Gille, F. A. Haumann, K. S. Johnson, S. C. Riser, I. Rosso, J. Sauvé, and J. L. Sarmiento (submitted), Indo-Pacific sector dominates Southern Ocean carbon outgassing, *Global Biogeochemical Cycles*. The dissertation author was the primary investigator and author of this paper.

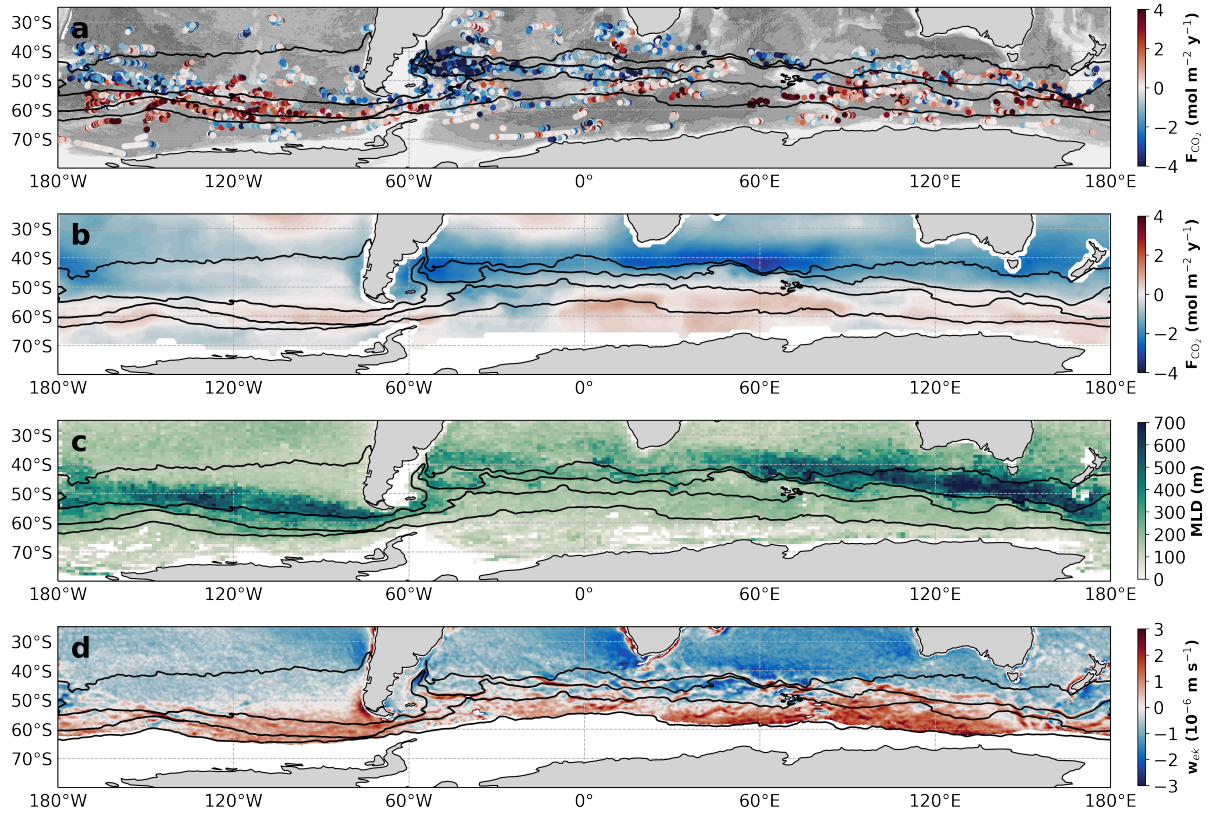

Figure 4.1. (a) Air–sea CO_2 flux (mol C/m^2/yr) estimated from autonomous biogeochemical float profiles (circles), 2014-2020. Positive flux indicates carbon outgassing from the ocean to the atmosphere. Gray shading marks bathymetry and black lines denote the mean position of the Antarctic Circumpolar Current fronts, which are from north to south: Subtropical front, Subantarctic front, Polar front, and Sea Ice Edge. (b) Annual mean air–sea CO_2 flux (mol C/m^2/yr) from the Landschützer et al. (2015) climatology, 1982-2015. (c) Maximum mixed-layer depth (m) in $1^\circ \times 1^\circ$ bins from Argo data, 2000-2020. (d) Annual mean Ekman pumping velocity (10^{-6} m/s) calculated from a scatterometer wind-stress curl climatology (Risien et al., 2008), 1999-2009, where positive velocities denote Ekman upwelling.

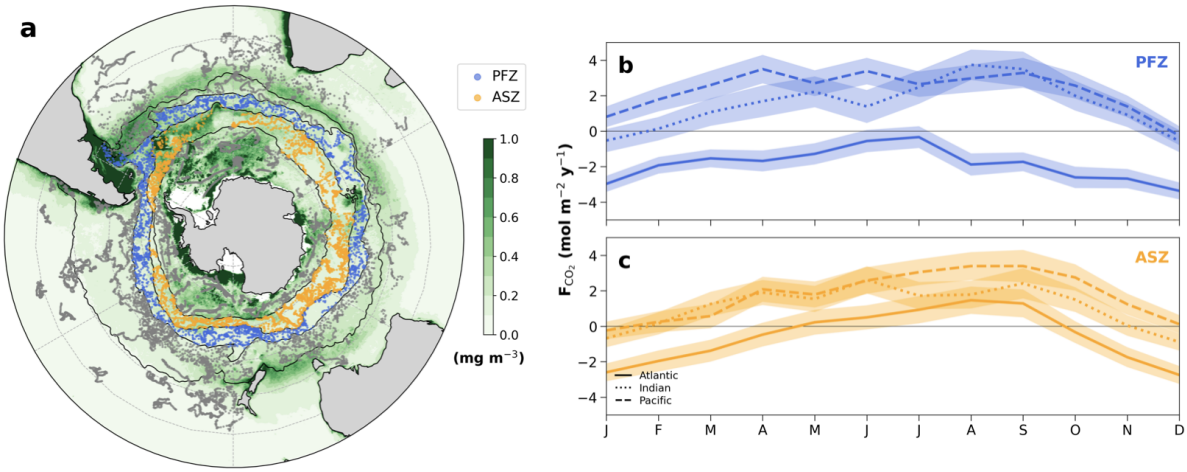

Figure 4.2. (a) Autonomous biogeochemical float profile locations sorted by frontal zone (PFZ: Polar Frontal Zone, ASZ: Antarctic Southern Zone). Background shading shows austral summer surface chlorophyll (mg/m^3) from a 2002-2019 satellite ocean color climatology. (b) Monthly climatology of air–sea CO_2 flux (mol C/m^2/yr) in the PFZ from float profiles in the Atlantic, 65°W-25°E (solid line), Indian, 25°E-150°E (dotted line), and Pacific, 150°E-65°W (dashed line) sectors. (c) Same as (b) but for the ASZ.

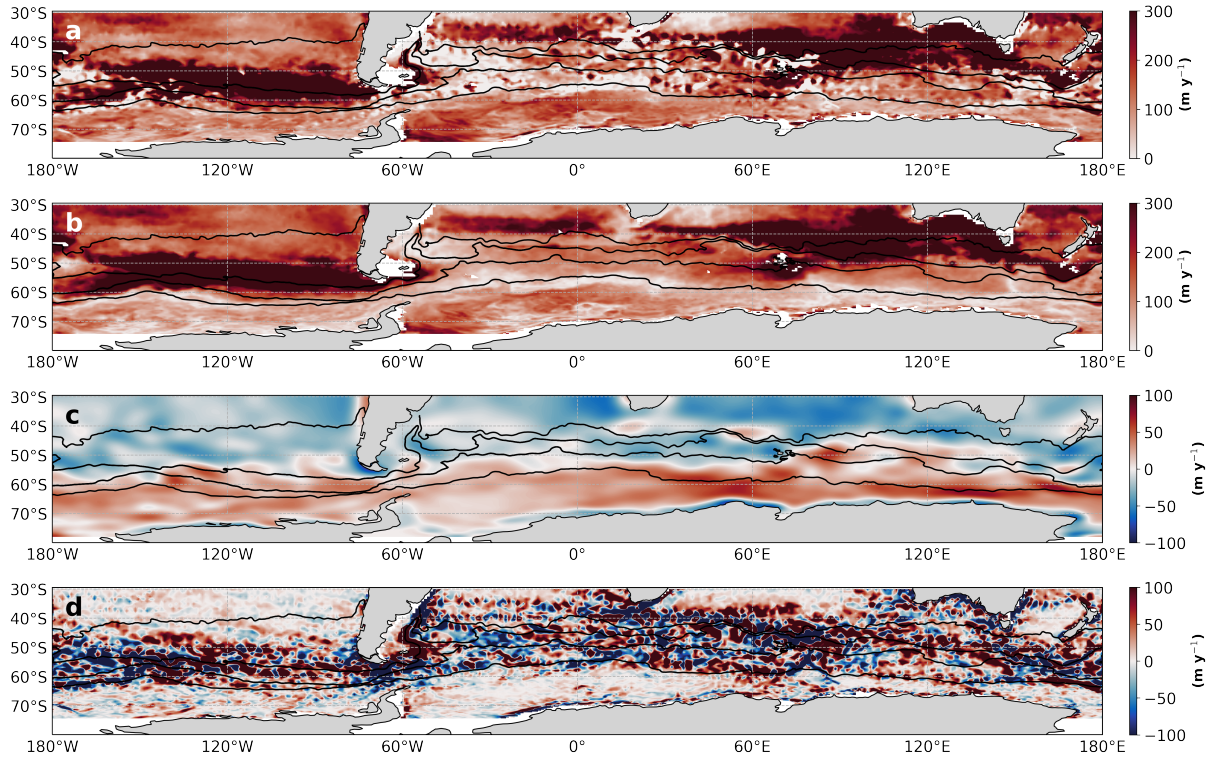

Figure 4.3. (a) Annual mean obduction rate (m/yr) and contributions due to (b) mixed-layer tendency, (c) Ekman pumping velocity, and (d) lateral induction. See Section 4.2.3 for details of the calculation.

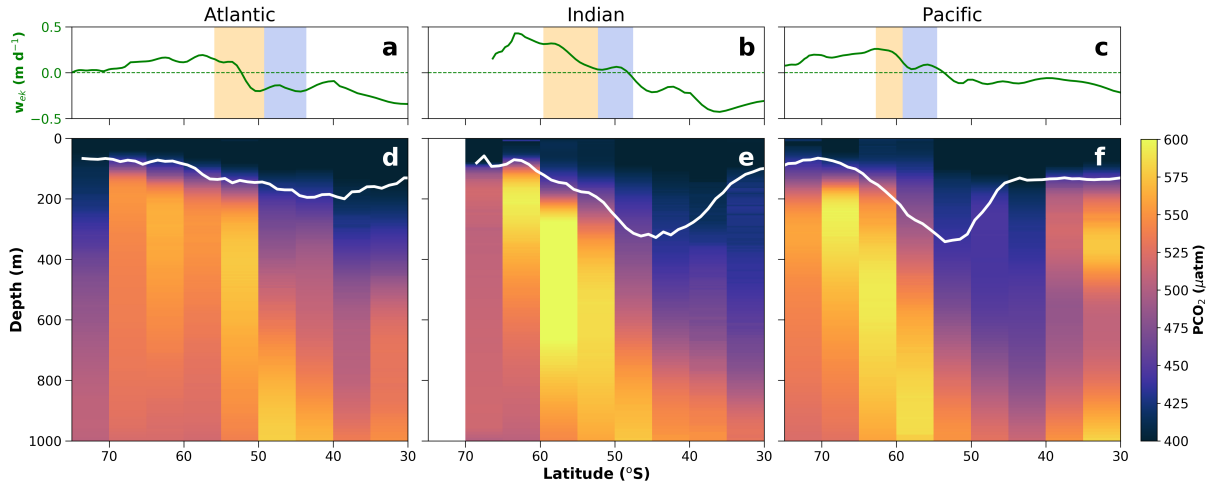

Figure 4.4. (a-c) Zonally averaged annual mean Ekman pumping velocity (m/d). Shading indicates the mean latitude range of the PFZ (blue) and ASZ (orange). (d-f) Annual mean PCO_2 (μatm) from autonomous float data zonally averaged in 5° latitude bands with annual maximum mixed-layer depth overlaid in white. Averages are calculated separately for the (a,d) Atlantic, 65°W-25°E, (b,e) Indian, 25°E-150°E, and (c,f) Pacific, 150°E-65°W, sectors of the Southern Ocean.

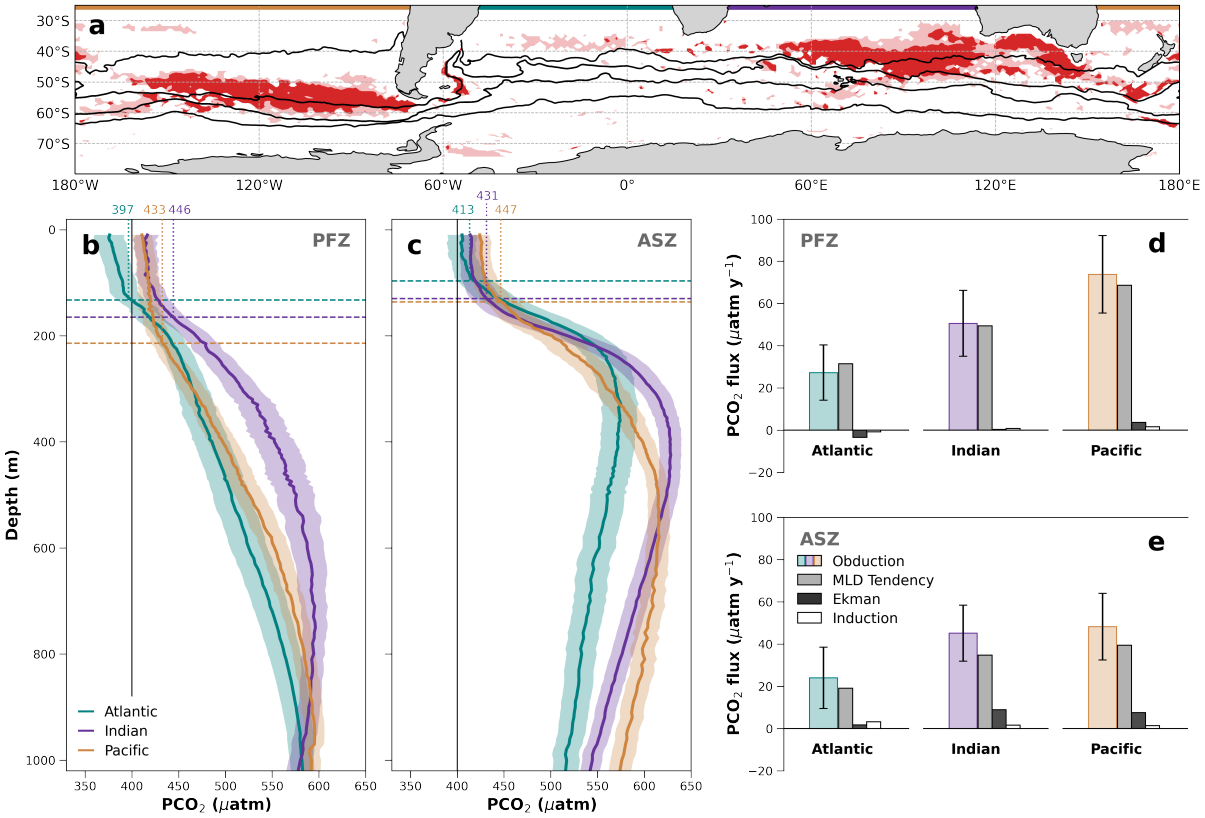

Figure 4.5. (a) Regions with the largest annual mean obduction rates (200 and 300 m/yr contours plotted in pink and red). (b) Mean vertical profiles of PCO_2 during the obduction period in the Atlantic (teal), Indian (purple), and Pacific (brown) PFZ. Horizontal lines mark the mean MLD in each basin at that time and dotted lines indicate the PCO_2 value at the mean mixed-layer base (values given in raised labels). A black vertical line designates PCO_2 of 400 μatm, the approximate atmospheric value in 2015. (c) Same as (b) for the ASZ. (d) Annual mean PCO_2 obduction fluxes (teal, purple, and brown bars) in the PFZ for each basin, and decomposed into contributions from the mixed-layer tendency (gray), Ekman pumping (black) and lateral induction (white). (e) Same as (d) for the ASZ.

4.6 Supplementary Material

The Supplementary Material gives details on the uncertainty analysis for the PCO_2 obduction fluxes (4.6.1) and additional analysis to test whether results were influenced by the data distribution (4.6.2). Figure 4.6 shows the float-based air-sea CO_2 flux climatologies for the other frontal zones. Figures 4.7 and 4.8 show the number of float profiles by month and by year for each sector in the PFZ and ASZ.

4.6.1 Uncertainty Analysis

The total uncertainty in the annual mean PCO_2 obduction flux was determined from the uncertainties in each component associated with obduction in Equation 4.3 using a Monte Carlo simulation with 5000 iterations for each frontal zone and basin. The uncertainties in the MLD tendency and lateral MLD gradients were found from the Gaussian process regression mapping errors (Kuusela & Stein, 2018). Note that this does not incorporate the error associated with failing to resolve high-frequency MLD deepening events. The reported error accompanying the velocity product (Gray & Riser, 2014) is used for the induction uncertainty estimate. For the reanalysis winds, we use the uncertainty estimation based on a 10-member ensemble of data assimilations system (Hersbach et al., 2020). Finally, the uncertainty for the vertical PCO_2 gradient is computed based on both the variability within the region and the error associated with estimating pCO_2 from in situ pH (Williams et al., 2017).

The total uncertainty in the annual mean PCO_2 obduction flux is of the order 15-25 μatm/y. While this is a significant percentage of the total obduction flux, the difference between the fluxes in the Atlantic and Pacific PFZ is statistically significant. In the ASZ, the inter-basin difference is not statistically significant due to the large error bars. However, we assessed other possible mechanisms that could drive the basin asymmetry such as diffusion and Annual Net Community Production, and only obduction could account for the full magnitude of the observed asymmetry in surface pCO_2. Furthermore, independent studies (Liu & Huang, 2012; Viglione &

Thompson, 2016) have also shown higher obduction rates in the Indo-Pacific, suggesting that the mechanisms discussed in the main text are robust.

We also tested the sensitivity of the results to the choice of integration period by repeating the calculation using several different lengths of time for obduction. While the absolute magnitude of the PCO_2 obduction flux does vary depending on how the obduction period is defined, our focus here is on the difference between the obduction fluxes in the Atlantic and Indo-Pacific, which is similar regardless of the precise obduction period used for the integration. It is also possible that the length of the obduction period varies between sectors, although this is difficult to meaningfully assess from the monthly MLD climatology due to the coarse temporal resolution. However, the obduction period is typically longer in locations with greater Ekman upwelling (Qiu & Huang, 1995). This implies a prolonged obduction period in the Indo-Pacific PFZ and ASZ compared to the Atlantic, which would reinforce the asymmetry in obduction flux of PCO_2.

4.6.2 Assessing Sampling Bias

To examine whether results were influenced by seasonal biases in sampling within a given sector or by having observations heavily skewed towards one year in a particular basin, the data distribution was examined in several ways. Figure 4.7 shows the number of profiles by month for each sector of the Polar Frontal Zone (PFZ) and Antarctic Southern Zone (ASZ). Given that the areal extent of the frontal zones varies significantly between basins, the profile numbers in the Indian and Atlantic were normalized to the area of the Pacific to more easily compare the data coverage across sectors. The data distribution is similar for all basins and there is no significant seasonal bias in any sector. We also assess the interannual variability in sampling. For all basins and frontal zones, the number of profiles per year has typically increased through time as more floats have been deployed. Still, in a given year, the number of profiles is similar for all basins within the PFZ and ASZ after normalizing to account for the areal differences between sectors (Figure 4.8). This is also significant because of the long-term increase in both

atmospheric and surface ocean pCO_2 due to climate change. Our goal in this study is to explain the difference between basins, rather than the absolute pCO_2 value. Because the data distribution is similar in a given year across sectors, the long-term trend should be removed when we take the difference between basins.

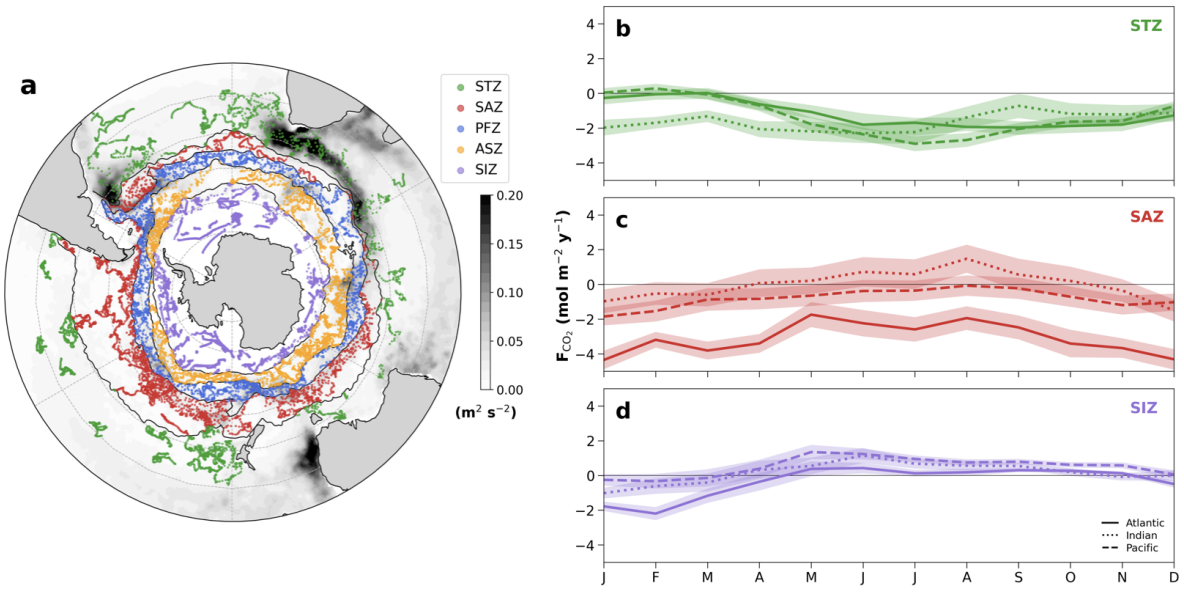

Figure 4.6. (a) Autonomous biogeochemical float profile locations sorted by frontal zone (STZ: Subtropical Zone, SAZ: Subantarctic Zone, PFZ: Polar Frontal Zone, ASZ: Antarctic Southern Zone, SIZ: Seasonal Ice Zone). Background contours show the mean eddy kinetic energy (m^2/s^2) from surface drifters (Laurindo et al., 2017). (b) Monthly climatology of air-sea CO_2 flux in the STZ from float profiles in the in the Atlantic, 65°W-25°E (solid line), Indian, 25°E-150°E (dotted line), and Pacific, 150°E-65°W (dashed line) sectors. (c) Same as (b) but for the SAZ. (d) Same as (b) but for the SIZ.

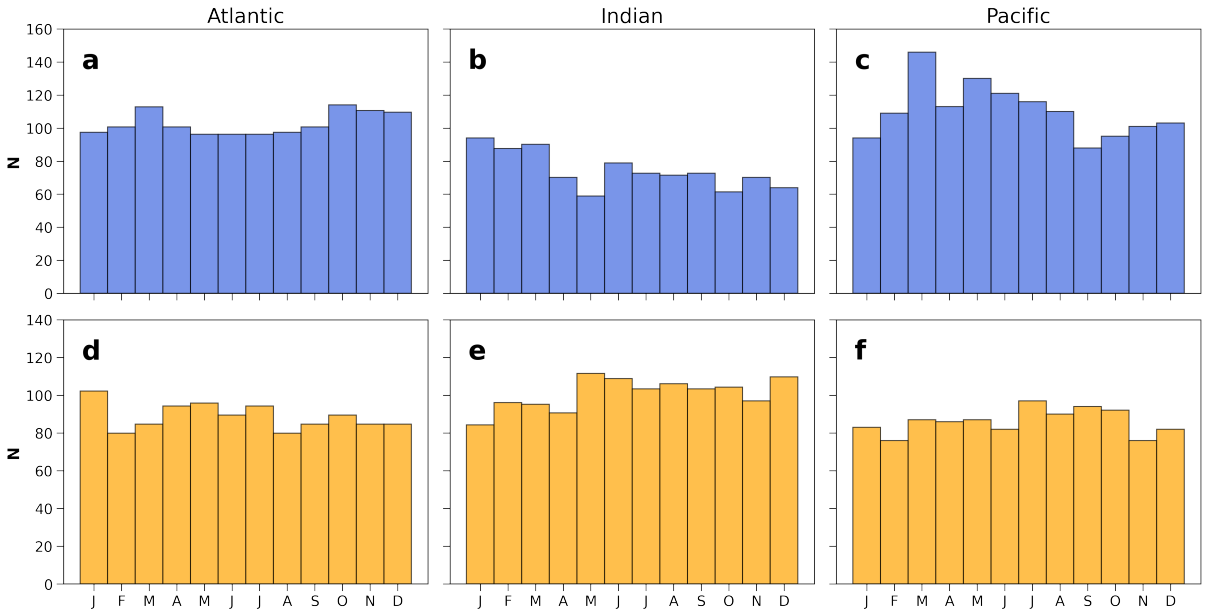

Figure 4.7. Number of float profiles (N) by month in each sector of the PFZ (a)-(c) and ASZ (d)-(f). Given that the areal extent of the frontal zones varies significantly between basins, the profile numbers in the Indian and Atlantic were normalized to the area of the Pacific to more easily compare the data coverage across sectors.

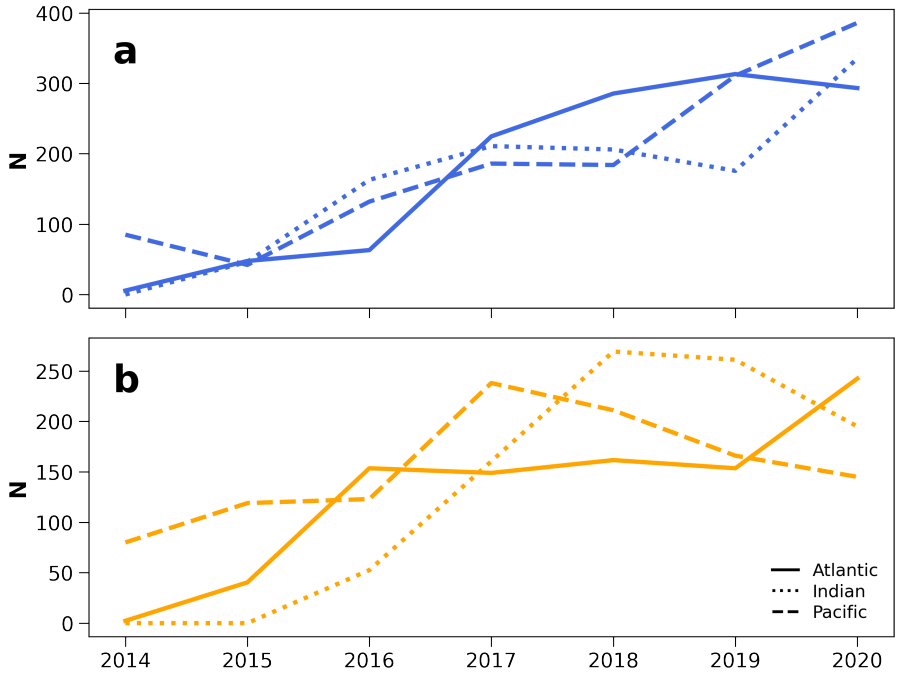

Figure 4.8. Number of float profiles (N) in the PFZ by year for the Atlantic (solid line), Indian (dotted line), and Pacific (dashed line) sectors. Given that the areal extent of the frontal zones varies significantly between basins, the profile numbers in the Indian and Atlantic were normalized to the area of the Pacific to more easily compare the data coverage across sectors. (b) Same as (a) but for the ASZ.

Chapter 5

Sub-seasonal forcing drives year-to-year variations of Southern Ocean primary productivity

Abstract

Primary productivity in the Southern Ocean plays a key role in global biogeochemical cycles. While much focus has been placed on phytoplankton seasonality, non-seasonal fluctuations exceed the amplitude of the seasonal cycle across large swaths of the Antarctic Circumpolar Current. This non-seasonal variability comprises a broad range of timescales from sub-seasonal to multi-annual, all of which can project onto the annual mean value. However, year-to-year variations of surface chlorophyll (SChl), a proxy for phytoplankton biomass, are typically attributed to ocean circulation changes associated with the Southern Annular Mode (SAM), which implicitly assumes that sub-seasonal variability averages to near-zero over long timescales. Here, we test this assumption by applying a timeseries decomposition method to satellite-derived SChl in order to separate the low-frequency and high-frequency contributions to the non-seasonal variability. We find that throughout most of the Southern Ocean, year-to-year SChl variations are dominated by the sub-seasonal component, which is not strongly correlated with the SAM. The multi-annual component, while correlated with the SAM, only accounts for about 10% of the total SChl variance. This suggests that changes in annual mean SChl are related to intermittent forcing at small scales, rather than low-frequency climate variability, and

thus do not remain correlated over large regions.

5.1 Introduction

The Southern Ocean is a high-nutrient low-chlorophyll environment where phytoplankton growth is limited primarily by iron and light (Mitchell et al., 1991; de Baar et al., 1995). Physical processes in the ocean impact these controls, subsequently affecting the distribution of phytoplankton across a wide range of space and time scales (Lévy et al., 2012; Rousseaux & Gregg, 2014; Ardyna et al., 2017; Rohr et al., 2017; Z. Li et al., 2021). Indeed, phytoplankton biomass, inferred from satellite-derived surface chlorophyll (SChl), exhibits variability from sub-seasonal to multi-annual timescales (Arrigo et al., 2008; Thomalla et al., 2011; Frenger et al., 2018; Keerthi et al., 2020). Untangling these disparate scales is necessary to identify long-term trends associated with climate change, which are currently eclipsed by natural year-to-year variations in most regions (Behrenfeld et al., 2006; Martinez et al., 2009; Henson et al., 2010; Gregg & Rousseaux, 2019).

In the Southern Ocean, changes in annual mean SChl are often linked to the Southern Annular Mode (SAM), the leading mode of atmospheric variability in the Southern Hemisphere (D. W. J. Thompson & Wallace, 2000). SAM influences the ocean circulation and stratification in the region, which in turn impacts primary productivity by modulating nutrient and light availability (Lovenduski & Gruber, 2005; Boyd et al., 2008; Sallée et al., 2010). For example, Lovenduski and Gruber (2005) regressed non-seasonal satellite chlorophyll anomalies onto the SAM index; their results suggest that SChl is positively correlated with the SAM south of the Polar Front (PF) due to increased iron supply by anomalous upwelling, and negatively correlated with the SAM north of the PF due to stronger light limitation stemming from deeper mixed layers.

While this type of analysis has helped discern mechanisms of non-seasonal SChl variability, there are limitations to this approach. First, using the SAM index as a measure of climate

variability neglects significant regional differences in Southern Ocean winds, air-sea heat fluxes, mixed-layer depth (MLD) and its response to forcing (Sallée et al., 2010; Tamsitt et al., 2016; Rintoul, 2018; Keppler & Landschützer, 2019). Second, relating non-seasonal SChl variations to low-frequency climate modes presumes that the effects of high-frequency variability are negligible at annual and longer timescales. However, recent work suggests that sub-seasonal events dominate the total non-seasonal SChl signal at the global scale, even explaining more variance than the seasonal cycle in some places (Keerthi et al., submitted). One such region, identified in Keerthi et al. (submitted), is the Southern Ocean. Therefore, here we further investigate the processes that drive year-to-year variations of Southern Ocean primary productivity.

Following Keerthi et al. (2020; submitted), we decompose satellite-derived SChl into three frequency ranges: sub-seasonal ($\sim$0.5-3 months), seasonal ($\sim$3-12 months), and multi-annual ($>$12 months). We show that in the Southern Ocean, non-seasonal SChl variability primarily reflect sub-seasonal fluctuations, which occur over small spatial scales ($\sim$50-150 km) and are not strongly correlated with the SAM. The multi-annual component of SChl, by contrast, is correlated with the SAM, but only explains about 10% of the total SChl variance across most of the Antarctic Circumpolar Current (ACC). This suggests that year-to-year variations in annual mean SChl are related to intermittency, possibly resulting from the non-Gaussianity of chlorophyll as well as localized forcing from storms and eddies, rather than low-frequency climate modes (Lévy et al., 2014). Consequently, the spatial scales associated with consistent variations in the annual mean are small ($\sim$100-300 km), which implies that SChl should not be averaged over large regions to investigate year-to-year changes.

Complementary to satellite ocean color data, recent advances in autonomous observing platforms have dramatically increased the number of subsurface biogeochemical measurements in the Southern Ocean (Johnson et al., 2017b; Talley et al., 2019). Fluorescence measurements from autonomous floats have shown good agreement with satellite-derived SChl products, and provide data under clouds and during polar night (Haëntjens et al., 2017). However, given the complex vertical structure of phytoplankton biomass in the Southern Ocean (Carranza et al.,

2018; Uchida et al., 2019), fluctuations in SChl do not necessarily reflect changes in the vertically integrated chlorophyll column inventory ([Chl_{tot}]). Therefore, we also apply the same timeseries decomposition to float SChl and [Chl_{tot}] to show that strong sub-seasonal variability in SChl is representative of the integrated signal. These results highlight the importance of small-scale processes in determining the annual mean SChl and its variability.

5.2 Data and Methods

5.2.1 Observational Datasets

In this study, we use a merged SChl data product from the European Space Agency Ocean Color Climate Change Initative (ESA OC-CCI) that combines data from multiple ocean color satellites (Sathyendranath et al., 2017) including Moderate Resolution Imaging Spectroradiometer (MODIS), Sea-Viewing Wide Field-of-View Sensor (SeaWiFS), MEdium Resolution Imaging Spectrometer (MERIS) and Visible Infrared Imaging Radiometer Suite (VIIRS). We use the Level 3 Mapped 25×25 km version at 8-day temporal resolution, which spans 20 years from January 1999 to December 2018 and is publicly available (http://www.oceancolour.org/). This merged data product captures a longer time period than any individual satellite, and thus is well-suited for investigations of year-to-year variability. However, as with all ocean color products, there are many data gaps in the Southern Ocean due to cloudiness, ice cover and low sun angles (Arrigo et al., 2008). Locations with less than 50% data coverage are masked out in this analysis, although we note that most of the missing data are from austral winter when SChl levels are near-zero due to light limitation.

To evaluate the relationship between SChl and [Chl_{tot}] temporal variability, we also use in situ data from autonomous biogeochemical floats deployed by the Southern Ocean and Climate Field Studies with Innovative Tools (SOCLIM) project. SOCLIM floats measure temperature, salinity, pressure, dissolved oxygen, nitrate, fluorescence, backscatter, and photosynthetically available radiation (Pellichero et al., 2020). Here, we analyze quality-controlled data from 3

SOCLIM floats (float IDs: 6902735, 6902736, 6902737) that sampled in the Kerguelen Plateau region for three years, from September 2016 to September 2019 (http://soclim.com/). These floats were selected since they have higher resolution in time and depth than the standard biogeochemical Argo float. Data processing and corrections applied to the raw fluorometer data are described by Roesler et al. (2017). Floats sampled unevenly in the vertical, so all profiles are linearly interpolated onto a regular depth axis with 5 m resolution. SChl is taken to be the average chlorophyll over the top 20 m, while [Chl_{tot}] is calculated as the vertical integral over the top 200 m of the water column (Grenier et al., 2015; von Berg et al., 2020). Floats also sampled unevenly in time, with profiles taken daily, every 2 days, and every 4 days at different points during the float lifetime. Here, we average the float data in time to match the 8-day temporal resolution of the satellite SChl product.

Wind data from the Cross-Calibrated Multi Platform (CCMP) product are used to examine some of the forcings that drive SChl variability. CCMP combines wind data from several satellite scatterometers, moored buoys, and a reanalysis product (Atlas et al., 2011). CCMP winds have been shown to be more reliable at high frequencies than any single scatterometer, and have higher correlations with MLD than other wind products (Atlas et al., 2011; Carranza & Gille, 2015). The merged wind product is available on the same 25×25 km horizontal grid as the SChl data from ESA OC-CCI. Here, we take 8-day averages of the daily winds from 1999 to 2018 (i.e. the ESA OC-CCI period) to correspond directly with the ocean color data. The daily Antarctic Oscillation index (i.e. SAM index) from the NOAA/NCEP Climate Prediction Center during 1999 to 2018 (http://www.cpc.ncep.noaa.gov/) was also averaged into 8-day periods to calculate correlations of different fields with the SAM. Finally, several figures include the mean position of the ACC fronts from Kim and Orsi (2014), and Figure 5.1c shows mean eddy kinetic energy (EKE) derived from a surface drifter climatology (Laurindo et al., 2017).

5.2.2 Decomposition Method

Here, we decompose SChl timeseries at each grid point into three frequency bands following the method in Keerthi et al. (2020; submitted), which is based on the Census X11 iterative algorithm (Vantrepotte & Mélin, 2009). This decomposition uses a series of filters to separate the full SChl signal (X_t) into seasonal (S_t), multi-annual (T_t) and sub-seasonal (I_t) components such that $X_t = S_t + T_t + I_t$. The seasonal component, S_t, captures variability with a period of $\sim$3-12 months and is isolated by taking multiple weighted running means over three consecutive timesteps and then applying an 88-day (i.e. approximately 3 months given the temporal resolution of the data) low-pass filter. To account for year-to-year variations in the seasonal cycle, this decomposition method does not assume an annually repeating S_t. The multi-annual component, T_t, is determined by a centered annual running mean and a Henderson filter of weight representing one year. The sub-seasonal component, I_t, is found by applying a bandpass filter of 8-88 days. Finally, the residual is attributed to the sub-seasonal component, such that the timeseries is exactly decomposed into the sum of the three components. Note that this method does not have sharp frequency cut-offs in order to allow for variations in the dominant period of the seasonal cycle and multiple harmonics in S_t. Further details of the decomposition method are provided in Keerthi et al. (2020). Figure 5.2 illustrates the timeseries decomposition at three grid points whose locations are marked in Figure 5.1.

The total SChl variance is partitioned into the sum of the variance in the seasonal, multi-annual and sub-seasonal components, as well as the covariance between the three: var(X_t)=var(S_t) +var(T_t)+var(I_t)+2cov(S_t, T_t, I_t). The covariance term is small (explaining only a few percent of the total variance), so examining the individual variances of S_t, T_t, and I_t directly quantifies the contribution of each frequency band to the total SChl variance. This is shown in Figure 5.3. We also estimate the spatial scales associated with each component of SChl variability by cross-correlating S_t, T_t, and I_t at a given grid cell with the corresponding components at all other grid cells. From the number of cells where the correlation coefficient exceeds a threshold of

0.8, we then compute the area over which each signal remains consistent. This threshold value was chosen following Keerthi et al. (2020), although the length scales are similar for a range of threshold values from 0.5 to 0.9 (not shown).

5.2.3 Synthetic Data

In order to probe the statistical nature of the results, we also produced two synthetic timeseries with different probability distributions. Both artificial variables have red spectra, which are common for geophysical quantities, weighted toward low frequencies without a preferred period (Torrence & Compo, 1998; Maraun et al., 2007; Schulte et al., 2015). We generated red noise using an auto-regressive process with a lag-1 autocorrelation coefficient of 0.85, following Allen and Smith (1996). The first artificial variable is zero-mean with a Gaussian distribution (Figure 5.5a), which is representative of many normally distributed oceanic tracers. SChl, however, has been observed to follow a log-normal distribution; this is presumably because bio-optical properties in the ocean can be represented as the product of light attenuation coefficients, which would imply that SChl obeys the law of proportionate effect (Campbell, 1995). Therefore, our second artificial variable is taken to be the exponential of the first (Figure 5.5b), meaning that it is positive-valued and log-normally distributed, like SChl. We then apply the same decomposition method to the synthetic timeseries, although the three components simply represent high, mid, and low frequency bands since the timesteps are essentially arbitrary (i.e. the red noise cannot be interpreted as having sub-seasonal, seasonal, and multi-annual components).

5.3 Results

5.3.1 Satellite Analysis

Southern Ocean primary productivity is heterogeneous in space and time. Still, distinct bloom phenology regimes have been identified from satellite SChl, as well as large-scale patterns

in the mean (Thomalla et al., 2011; Sallée et al., 2015; Ardyna et al., 2017). Namely, higher annual mean SChl (Figure 5.1a) is observed in boundary current regions, near fronts, and downstream of islands or topographic features in the path of the ACC (Sokolov & Rintoul, 2007; Meredith et al., 2003; Rosso et al., 2016; Prend et al., 2019). These patterns are related to inhomogeneities in iron sources and the pathways that supply iron to the euphotic zone (Lacelot et al., 2009; A. Tagliabue et al., 2012; Graham et al., 2015). There is also significant spatial variability in the standard deviation of the annual mean (Figure 5.1b). Year-to-year variations of SChl are larger within the ACC and in energetic boundary currents with high EKE (Figure 5.1c). The subtropics, by contrast, have low SChl values and less variability between years, which coincides with weaker eddy activity and winds (Figure 5.1d).

Temporal SChl variability also demonstrates major regional differences, which is illustrated by the timeseries in Figure 5.2. In the subtropics (Figure 5.2a), SChl resembles a sinusoidal seasonal cycle with little change in amplitude between years, whereas in the open ACC (Figure 5.2b), SChl fluctuations occurring on weekly timescales greatly exceed the amplitude of the seasonal cycle. Finally, in boundary current regions such as the Brazil-Malvinas confluence (Figure 5.2c), the seasonal cycle is more prominent than in the open ACC (Figure 5.2b) but is punctuated by sub-seasonal pulses that significantly increase the magnitude of the annual maximum. These regional patterns in the dominant timescale of SChl variability lead to a fundamentally different interpretation of the annual mean SChl value itself. For example, in the subtropics, where SChl is driven by seasonal variability, annual mean SChl reflects the integrated seasonal bloom. In contrast, in the open ACC, where sub-seasonal variability dominates, annual mean SChl is manifested through the sum of transient bursts that take place throughout spring and summer.

To demonstrate that the stations plotted in Figure 5.2 are representative of larger regional regimes, Figure 5.3 shows the percentage of total SChl variance explained by each frequency range. Throughout the subtropics, the seasonal component explains $>$70% of the total variance (Figure 5.3b), consistent with the timeseries in Figure 5.2a. Moving southward into the ACC,

sub-seasonal variability is significantly stronger (Figure 5.3c), exceeding even the variance explained by the seasonal cycle in many locations, such as the station shown in Figure 5.2b. Across the entire Southern Ocean, the multi-annual component is weak except in a narrow band spanning the Subantarctic Mode Water formation sites in the Pacific, where the deepest winter mixed layers in the entire Southern Ocean are found. The comparatively large share of SChl variance explained by the multi-annual component in this region may be due to the substantial variations in maximum winter MLD observed there, which have been linked to the SAM (Meijers et al., 2019) and could influence nutrient supply to the euphotic zone.

Figure 5.3 clearly indicates that non-seasonal SChl variability in the Southern Ocean is dominated by high-frequency rather than low-frequency fluctuations. Averaged across the entire ACC, sub-seasonal variations constitute 47% of the total SChl variance, and 81% of the non-seasonal SChl variance. This helps explain the relatively modest correlations between non-seasonal chlorophyll anomalies and the SAM index (Lovenduski & Gruber, 2005). To further explore this, Figure 5.4 shows the correlation coefficients between the SAM index and each individual component of the SChl decomposition. The seasonal and sub-seasonal components of SChl are not strongly correlated with the SAM (Figure 5.4c,d). The multi-annual component, while much more highly correlated with the SAM (Figure 5.4b), only accounts for about 10% of the total SChl variance (Figure 5.3a). In other words, it is difficult to extract a relationship between satellite SChl and the SAM because the low-frequency SChl variability associated with SAM forcing is overwhelmed by the much larger SChl fluctuations occurring at high frequencies.

5.3.2 Synthetic Data Analysis

The large contribution of high frequencies to the total SChl variance could be a statistical result, since log-normally distributed variables (such as chlorophyll) are known to be heavy tailed (Campbell, 1995). Therefore, synthetic timeseries (Figure 5.5) with varied probability distributions were used to assess this. The insets in Figure 5.5 show the percent variance explained by high, mid, and low frequency bands. The zero-mean, Gaussian red noise has its

variance evenly divided between the three components of the decomposition (inset in Figure 5.5a), whereas the positive-valued, log-normal red noise has a greater portion of its variance, 46%, explained by the high frequency component (inset in Figure 5.5b). In other words, the large magnitude of sub-seasonal SChl variability seen in the satellite data is connected, in part, to its probability distribution, which lends more weight to extreme events due to its heavy tail. Still, the partitioning of variance from the satellite SChl data does not appear to be a purely statistical result, given that the same decomposition method applied to log(SChl) also indicates a disproportionate importance of sub-seasonal variability (not shown). Therefore, intermittent processes must help explain the outsized impact of sub-seasonal fluctuations on the total SChl variance, and thus their role in determining year-to-year variations.

5.3.3 Float Analysis

Given the sparsity of historical measurements in the Southern Ocean, remote sensing is an invaluable tool to study the region. However, satellite algorithms have been shown to underestimate SChl in the Southern Ocean compared to in situ measurements (Kahru & Mitchell, 2010). Furthermore, changes in SChl do not necessarily reflect changes in the integrated biomass (Carranza et al., 2018; Uchida et al., 2019). It is possible, for example, that sub-seasonal SChl variability is simply due to dilution or enhancement of the surface signal by episodic mixing, rather than high-frequency changes in phytoplankton biomass. To assess this, we analyze subsurface data from 3 autonomous floats deployed near Kerguelen Plateau by the SOCLIM project (Pellichero et al., 2020). Figure 5.6 shows the vertical chlorophyll section from float 6902735, as well as the comparison of SChl and [Chl_{tot}] timeseries.

Figure 5.6 illustrates that much of the chlorophyll signal is subsurface. However, the SChl and [Chl_{tot}] timeseries are reasonably well correlated (R=0.81), although less so at sub-seasonal timescales (R=0.66). This was found by applying the same decomposition method outlined in Section 5.2.2 to float SChl and [Chl_{tot}] (Figure 5.7). For SChl, the percentages of variance explained by the multi-annual, seasonal, and sub-seasonal components are 9%, 46%, and

44%, respectively, while for [Chl_{tot}], the percentages of variance explained by the multi-annual, seasonal, and sub-seasonal components are 8%, 55%, and 36%, respectively. In other words, sub-seasonal variability is stronger for SChl compared to [Chl_{tot}], which implies that at least part of the sub-seasonal signal at the surface reflects dilution and mixing processes rather than changes in total biomass. However, sub-seasonal [Chl_{tot}] variability still contributes a large share to the total variance and exceeds the multi-annual component. The same conclusion was drawn from the other two SOCLIM floats analyzed (floats IDs: 6902736 and 6902737). This suggests that the results based on satellite SChl data (Section 5.3.1) are relevant to the vertically integrated chlorophyll, although possibly slightly overestimating the contribution of sub-seasonal timescales.

5.4 Discussion and Conclusions

Satellite data and autonomous float measurements analyzed here show that sub-seasonal SChl variability exceeds multi-annual variability in the Southern Ocean. As a result, year-to-year variations of annual mean SChl primarily reflect high-frequency events rather than low-frequency variability. This is because, within the ACC, the annual mean SChl value itself results from the sum of intermittent pulses occurring at weekly timescales. Therefore, the annual mean SChl is higher in years with more or larger pulses, which is confirmed by high correlations between annual mean SChl and annual variance of the sub-seasonal component of SChl (Figure 5.8a). The inverse cascade toward low frequencies could result, for example, from changes in the prevalence of extreme wind events or eddy activity (Cravatte et al., 2021), which in turn may be connected to climate variability (Busecke & Abernathey, 2019; Hell et al., 2021), although sub-seasonal SChl fluctuations were only weakly correlated with the SAM index (Figure 5.4d).

The link between annual mean SChl and high-frequency events is important because sub-seasonal SChl variability occurs at spatial scales of $\sim$50-150 km. This leads to similarly small scales over which variations in annual mean SChl remain consistent (Figure 5.8b). In the

ACC, the average length scale associated with correlated fluctuations in annual mean SChl is only 260 km. This is in contrast to the seasonal cycle of SChl, which is forced by large-scale changes in solar irradiance and surface stratification, and thus has much larger spatial scales. For example, vast bloom phenology regimes have been defined based on SChl seasonality, and approximately correspond to the frontal zones of the ACC (Thomalla et al., 2011; Sallée et al., 2015; Ardyna et al., 2017). Indeed, averaging the satellite data over the Subtropical Zone (STZ), Subantarctic Zone (SAZ), and the ACC—as defined by the mean frontal positions from Kim & Orsi (2014)—shows that, in a given frontal zone, the seasonal component of SChl (S_t) has a small standard error (Figure 5.9a); this means that the seasonal cycle is relatively consistent across all grid cells, although note that the calculation of standard error implies Gaussian statistics. However, the full SChl signal (X_t) has larger standard errors within a frontal zone (Figure 5.9b), particularly in the SAZ and ACC where sub-seasonal variability is strong. This is also reflected in the fluctuations of annual mean SChl, which have large standard errors in the SAZ and in the ACC (Figure 5.9c), despite the regularity of the seasonal cycle over these zones. In other words, the bioregions relevant to phytoplankton seasonality are not necessarily meaningful in the context of year-to-year variations.

These results suggest that changes in annual mean SChl are tied to the forcing that drives sub-seasonal SChl fluctuations. This includes anomalies in wind stress or surface buoyancy forcing (Swart et al., 2015; Carranza & Gille, 2015; Keerthi et al., 2021), oceanic mesoscale and sub-mesoscale variability (Frenger et al., 2018; Whitt, Lévy, & Taylor, 2019; McGillicuddy, 2016), or ecosystem interactions such as top-down controls from grazing (Behrenfeld & Boss, 2014; Arteaga et al., 2020), competition for multiple resources (Huisman & Weissing, 2001), and interactions between the two (Mayersohn et al., 2021). It is difficult to separate the effects of these mechanisms for several reasons. First, the timescales associated with mesoscale and submesoscale physical processes overlap with those of intrinsic ecosystem variability. Second, the sign of the SChl response to wind or MLD perturbations exhibits significant seasonal and regional variability (Le Quéré et al., 2002; Llort et al., 2019). For example, several studies have

observed a seasonal progression from light limitation to nutrient limitation in the Southern Ocean (Ryan-Keogh et al., 2018; von Berg et al., 2020; Z. Li et al., 2021). In a light-limited regime (e.g. early spring), phytoplankton growth is associated with restratification due to decreased winds and/or submesoscale buoyancy fluxes (Swart et al., 2015; Thomalla et al., 2015; du Plessis et al., 2017; Pellichero et al., 2020). In contrast, in a nutrient-limited regime (e.g. summer), increases in SChl are driven by transient nutrient entrainment from storm-driven mixing (Carranza & Gille, 2015), eddy activity (Uchida et al., 2020), or wind-eddy interactions (Gille et al., 2014; du Plessis et al., 2019).

Untangling these mechanisms has important implications for year-to-year variability. For example, if sub-seasonal SChl fluctuations are driven primarily by wind-driven nutrient entrainment from synoptic storms, then annual mean SChl could presumably be linked to storm frequency. In contrast, if sub-seasonal SChl fluctuations are forced by oceanic (sub-)mesocale variability, then annual mean SChl would possibly be connected to changes in EKE. Finally, some studies suggest that the surface iron supply is set by wintertime mixing (a. S. J.-B. Tagliabue A. et al., 2014; Nicholson et al., 2019), in which case annual mean SChl would potentially be related to the previous winter's maximum MLD. Testing these hypotheses is difficult using observations. We tried, for example, to correlate annual mean SChl with summer storm frequency (Figure 5.10), defined as the percentage of days in summer (DJF) with daily mean wind speed greater than 10 m/s (Carranza et al., 2018). The correlations are relatively modest, but this could be due to inaccuracy in the wind product at high frequencies, decoupling in time between mixing and wind stress at sub-seasonal timescales (Whitt et al., 2017), the nonlinear relationship between MLD and surface forcing (Whitt, Nicholson, & Carranza, 2019), or variability in the phytoplankton response to MLD perturbations (Llort et al., 2019). Other studies (e.g. Z. Li et al., 2021) have additionally shown a weak relationship between annual mean productivity and MLD. However, further work is needed to quantify the contribution of these different processes to the total year-to-year variability.

While many previous studies have examined sub-seasonal SChl variability and have

highlighted the complex mechanisms at play, the role of high-frequency fluctuations in driving the annual mean SChl and its variability is not widely recognized. Non-seasonal SChl variability in the Southern Ocean has often been attributed to the SAM (Lovenduski & Gruber, 2005; Greaves et al., 2020). However, here we have shown that low-frequency SChl fluctuations, which show a relationship to the SAM index, are dwarfed by the much larger amplitude sub-seasonal variability. Therefore, year-to-year changes in annual mean SChl reflect episodic forcing, such as storms and eddies, rather than multi-annual climate variability. Although future work should investigate the role of climate modes in modulating the prevalence and magnitude of synoptic events and (sub-)mesoscale mixing (Busecke & Abernathey, 2019; Hell et al., 2021). One implication of these results is that annual mean SChl only varies consistently over small spatial scales. Consequently, developing a mechanistic understanding of year-to-year variations in Southern Ocean primary productivity is an inherently local question that requires resolving sub-seasonal, small-scale processes.

5.5 Acknowledgments

C. J. Prend, S. T. Gille, and L. D. Talley are supported by NSF OPP-1936222. C. J. Prend was also supported by a National Science Foundation Graduate Research Fellowship under Grant DGE-1650112 and a Chateaubriand Fellowship from the Office for Science & Technology of the Embassy of France in the United States. M. G. Keerthi is supported by a postdoctoral fellowship from CNRS. M. Lévy and O. Aumont acknowledge support from ANR-SOBUMS under contract number ANR-16-CE01-0014. 8-day composites of satellite surface chlorophyll are available from ESA OC-CCI (http://www.oceancolour.org/). Profiling float data were collected and made freely available by the Southern Ocean and Climate Field Studies with Innovative Tools (SOCLIM) project (http://soclim/com/). Daily wind speeds from the merged CCMP product are available online (http://www.remss.com/measurements/ccmp/). The daily Antarctic Oscillation index is available from the NOAA/NCEP

Climate Prediction Center (http://www.cpc.ncep.noaa.gov/). Mean EKE is calculated from a NOAA surface drifter climatology (http://www.aoml.noaa.gov/phod/gdp/mean_velocity.php).

Chapter Five, in full, has been submitted to Global Biogeochemical Cycles. Prend, C. J., M. G. Keerthi, M. Lévy, O. Aumont, S. T. Gille, L. D. Talley (submitted). Sub-seasonal forcing drives year-to-year variations of Southern Ocean primary productivity, *Global Biogeochemical Cycles*, submitted. The dissertation author was the primary investigator and author of this paper.

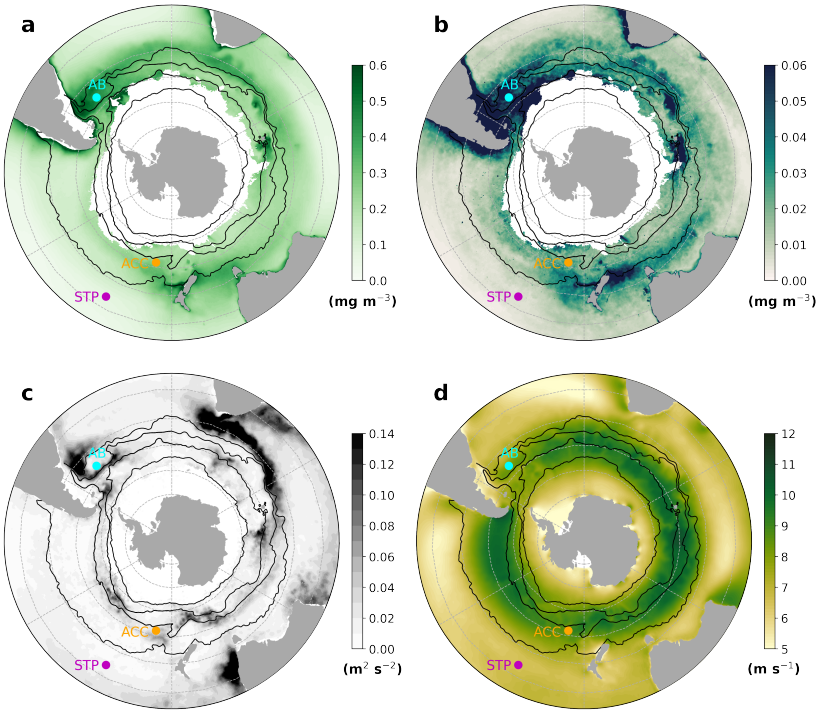

Figure 5.1. (a) 1999-2018 annual mean surface chlorophyll (mg/m^3) and (b) standard deviation of the annual mean (mg/m^3) from the ESA OC-CCI merged ocean color product. (c) 1979-2015 mean eddy kinetic energy (m^2/s^2) from surface drifters (Laurindo et al., 2017) (d) 1999-2018 summer (DJF) mean wind speed from the CCMP merged data product. Colored points in all panels mark the stations whose timeseries are plotted in Figure 5.2: Subtropical Pacific (STP; magenta), ACC (orange), and Argentine Basin (AB; cyan). Black lines in all panels mark the mean position of the ACC fronts from Kim & Orsi (2014).

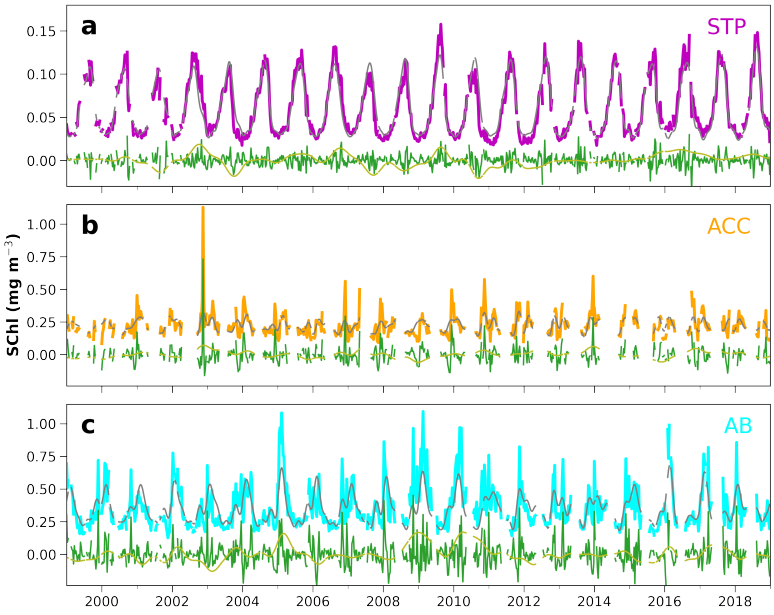

Figure 5.2. SChl timeseries decomposition for three stations marked in Figure 5.1: (a) STP (34°S, 152°W), (b) ACC (52°S, 170°W), and (c) AB (46°S, 45°W). The full signal (X_t) is plotted in (a) magenta, (b) orange, and (c) cyan. In all panels the seasonal component (S_t) is gray, the sub-seasonal component (I_t) is green, and the multi-annual component (T_t) is gold.

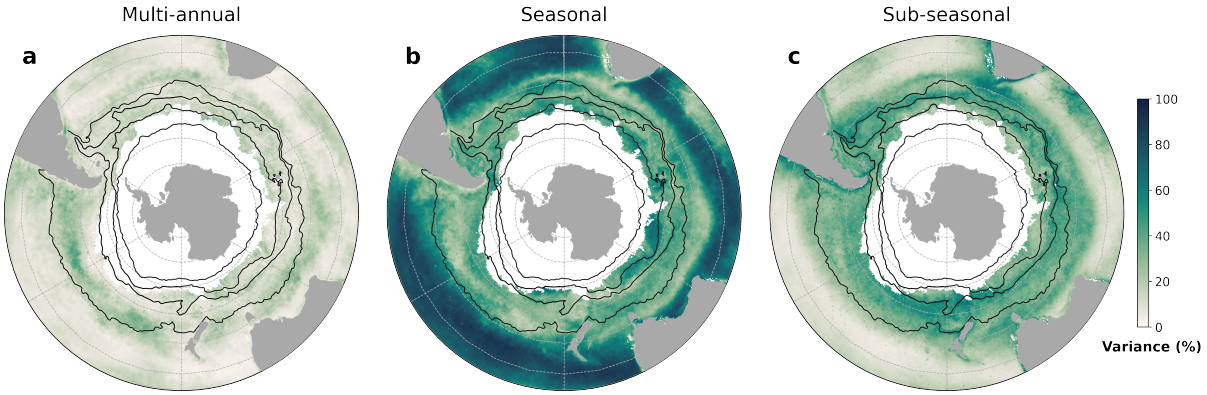

Figure 5.3. Percentage of the total SChl variance explained by the (a) multi-annual, (b) seasonal, and (c) sub-seasonal components of the SChl decomposition.

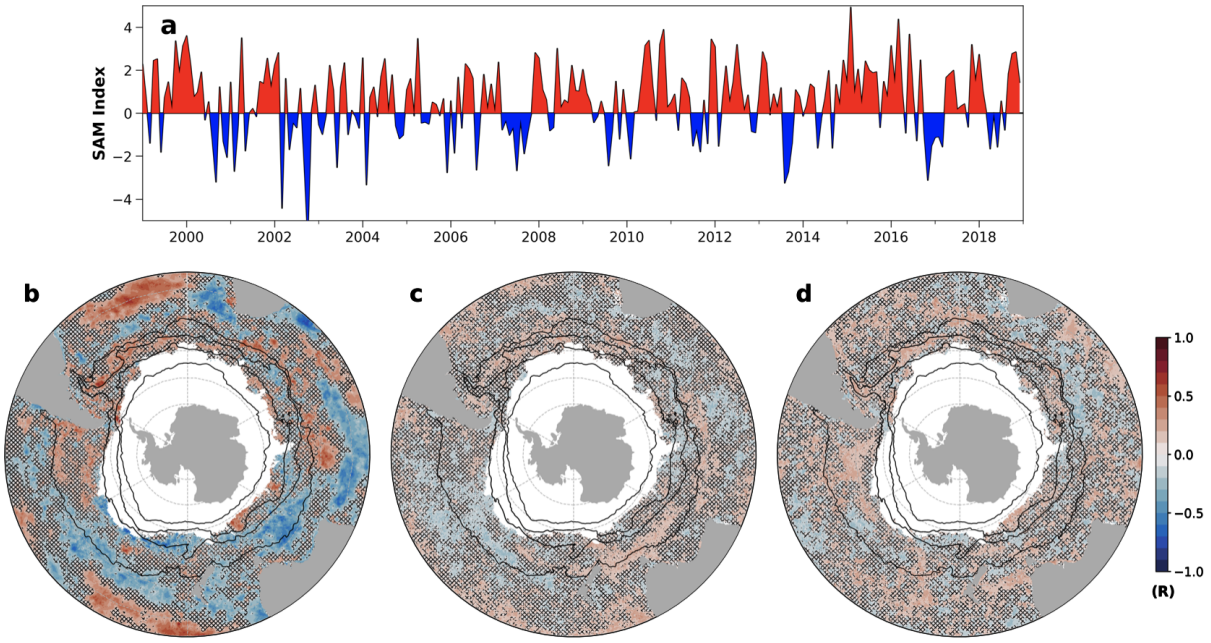

Figure 5.4. (a) 1999-2018 monthly SAM index from NOAA/NCEP Climate Prediction Center. (b-d) Correlation coefficient between the 8-day averages of the daily SAM index (to match the temporal resolution of the satellite SChl data) and the (b) multi-annual, (c) seasonal, and (d) sub-seasonal components of the SChl decomposition. In all panels, cross-hatching indicates where the correlations are not significant at the 95% level.

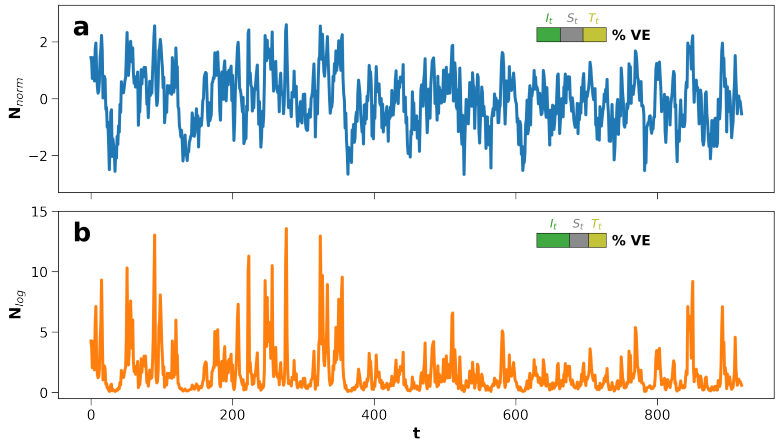

Figure 5.5. Synthetic timeseries of red noise generated by an auto-regressive process with (a) zero-mean and Gaussian distribution and (b) positive-valued and log-normal distribution. In both panels, insets show the percent variance explained by high (green), mid (gray), and low (gold) frequency bands.

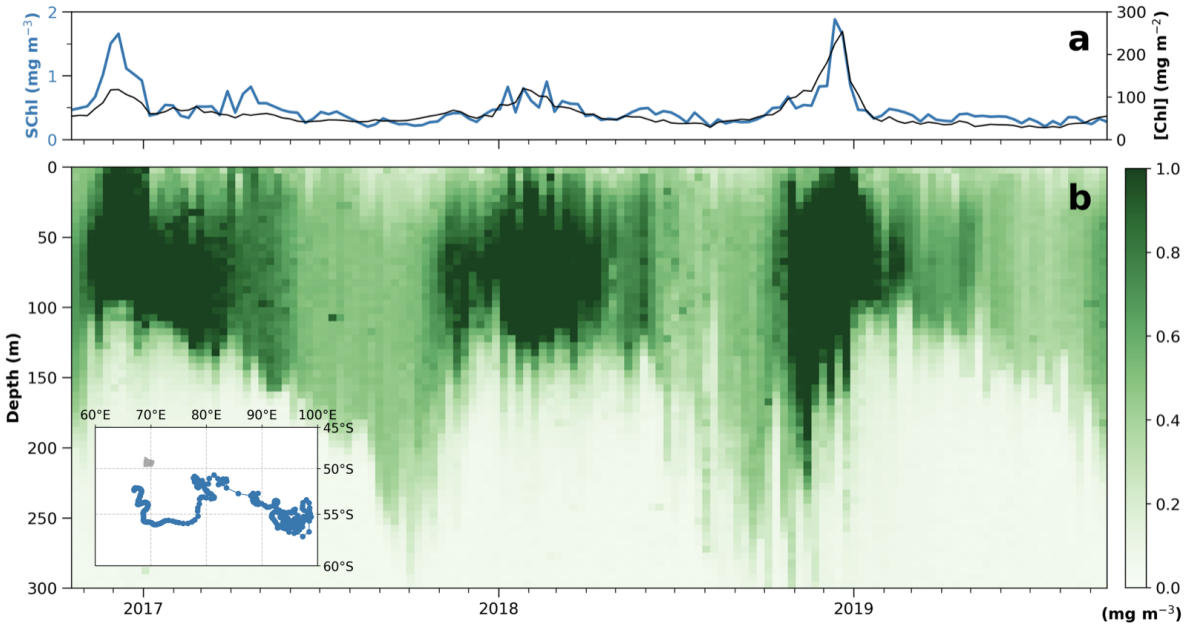

Figure 5.6. Float 6902735 (a) SChl (blue) and [Chl_{tot}] (black) timeseries, as well as (b) vertical chlorophyll section with inlay showing float trajectory.

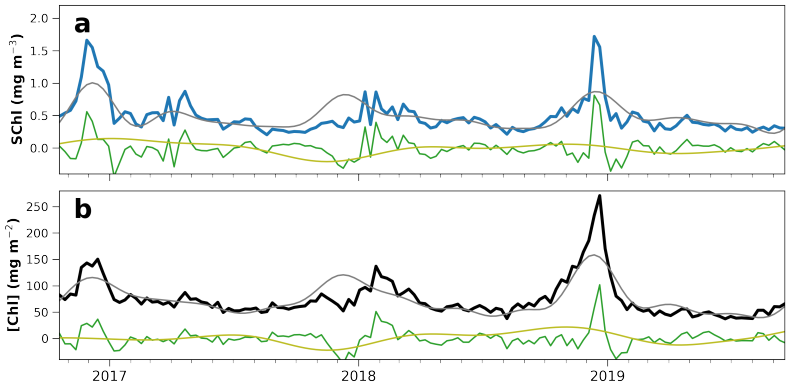

Figure 5.7. Timeseries decomposition of float 6902735 (a) SChl, full signal in blue, and (b) [Chl_{tot}], full signal in black. In both panels the seasonal component is gray, the sub-seasonal component is green, and the multi-annual component is gold.

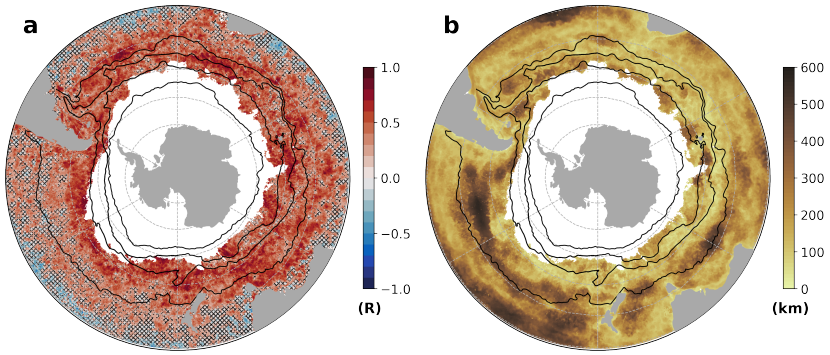

Figure 5.8. (a) Correlation coefficient between annual mean SChl and annual variance in the sub-seasonal component of SChl. Cross-hatching indicates where the correlations are not significant at the 95% level. (b) Length scale (km) associated with consistent variations in annual mean SChl.

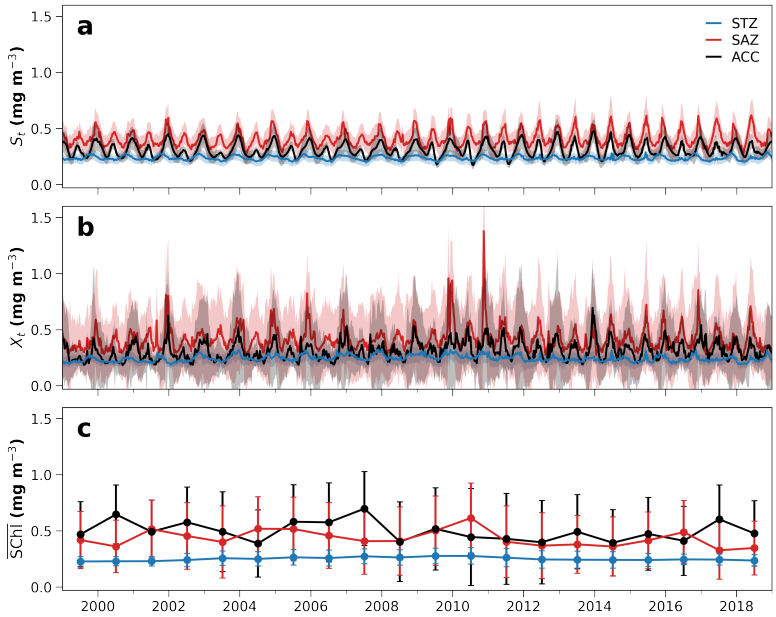

Figure 5.9. (a) Seasonal component of SChl (S_t) averaged over the Subtropical Zone (STZ), Subantarctic Zone (SAZ), and ACC, as defined by the Kim & Orsi (2014) fronts. (b) Full SChl signal (X_t) averaged over the same frontal zones as in (a). (c) Annual mean SChl ($\overline{\text{SChl}}$) for each frontal zone plotted at the mid-point of each respective year (i.e. July 2). Error bars reflect the standard error of all grid cells within each frontal zone.

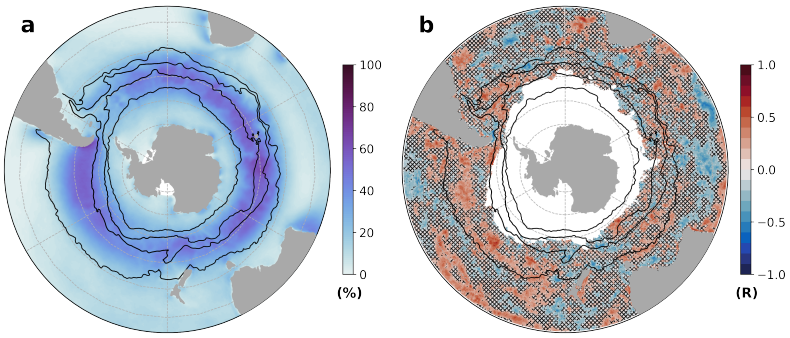

Figure 5.10. (a) 1999-2018 mean summer storm frequency, taken to be the percentage of days in summer (DJF) with daily mean wind speed greater than 10 m/s. (b) Correlation between annual mean chlorophyll and summer storm frequency. Cross-hatching indicates where the correlations are not significant at the 95% level.

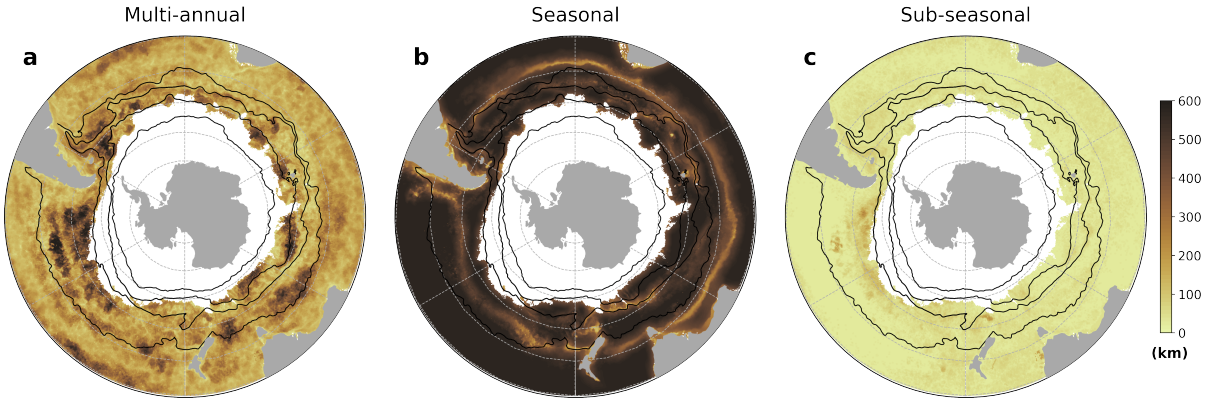

Figure 5.11. Length scale associated with the (a) multi-annual, (b) seasonal, and (c) sub-seasonal components of the SChl decomposition, computed by the cross-correlation method outlined in Section 5.2.2 of the main text.

5.6 Supplementary Material

The Supplementary Material provide six additional figures. These include maps showing the length scales associated with each components of the SChl decomposition, computed by the cross-correlation method outlined in Section 5.2.2, as well as the decomposition of the synthetic timeseries shown in Figure 5.5 of the main text. We also show plots analogous to Figures 5.6 and 5.7 in the main text for two additional autonomous biogeochemical floats (float IDs: 6902736, 6902737), i.e. the vertical chlorophyll sections and timeseries decompositions of float SChl and $[\text{Chl}_{\text{tot}}]$.

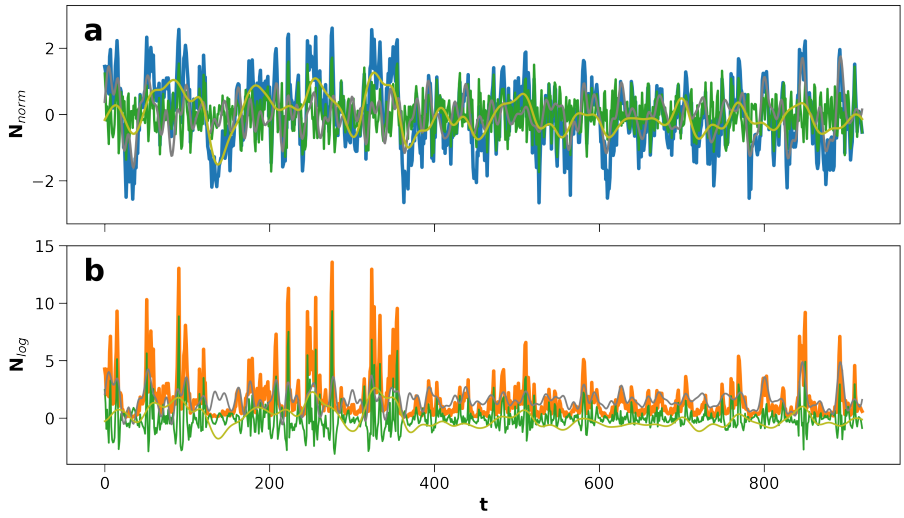

Figure 5.12. Decomposition of synthetic timeseries shown in Figure 5.5 of the main text, i.e. red noise generated by an auto-regressive process with (a) zero-mean and Gaussian distribution (full signal in blue) and (b) positive-valued and log-normal distribution (full signal in orange). In both panels, the green, gray, and gold lines denote the high, mid, and low frequency components of the full signal.

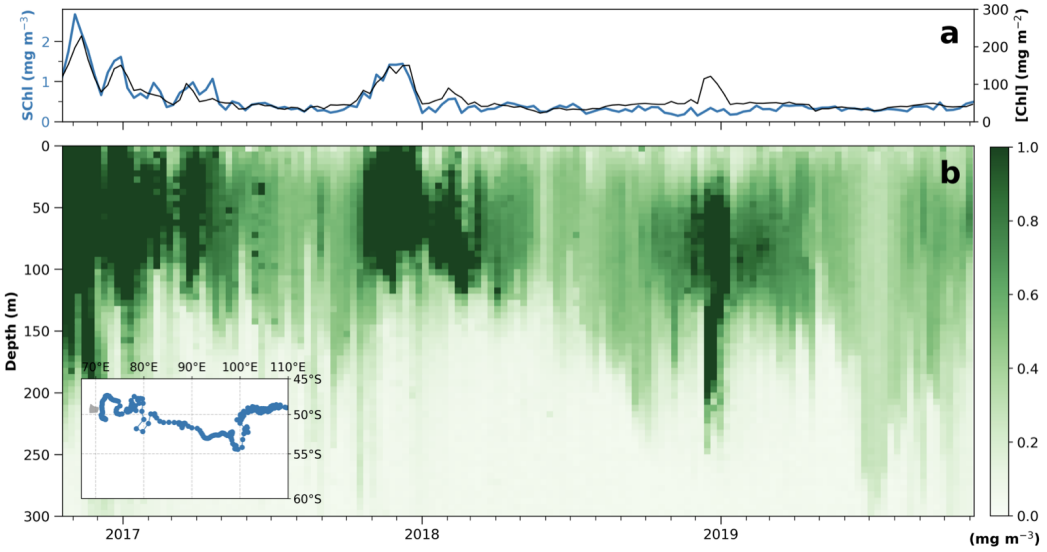

Figure 5.13. Float 6902736 (a) SChl (blue) and [Chl_{tot}] (black) timeseries, as well as (b) vertical chlorophyll section with inlay showing float trajectory.

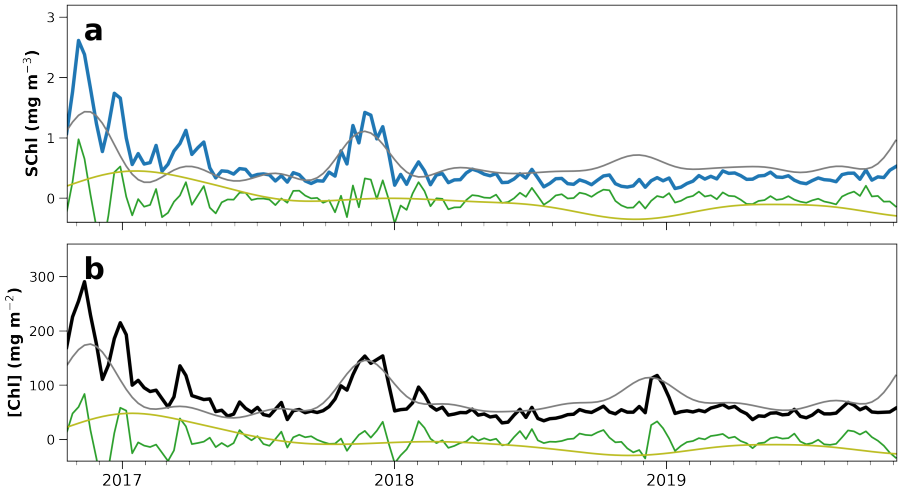

Figure 5.14. Timeseries decomposition of float 6902736 (a) SChl, full signal in blue, and (b) [Chl_{tot}], full signal in black. In both panels the seasonal component is gray, the sub-seasonal component is green, and the multi-annual component is gold.

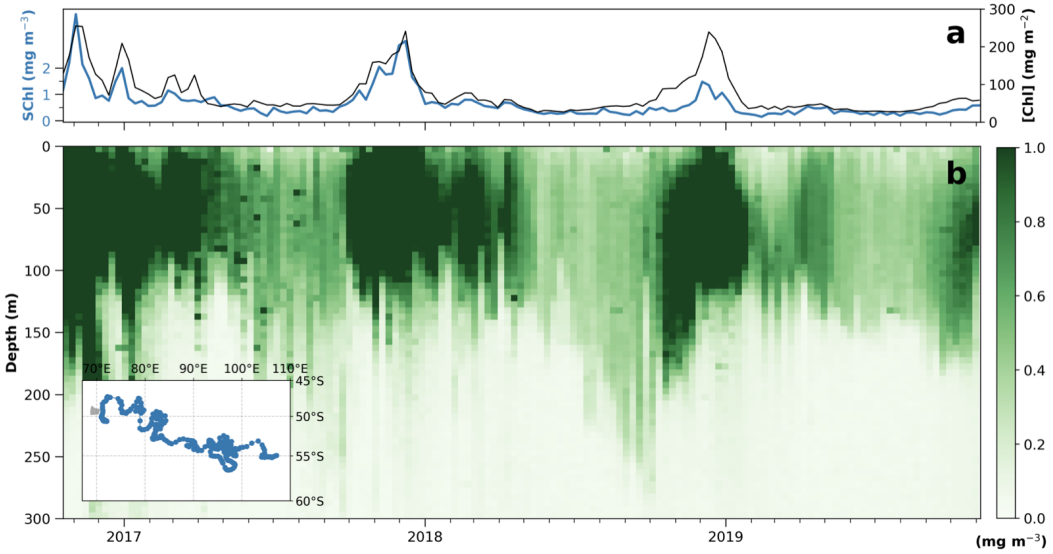

Figure 5.15. Float 6902737 (a) SChl (blue) and [Chl_{tot}] (black) timeseries, as well as (b) vertical chlorophyll section with inlay showing float trajectory.

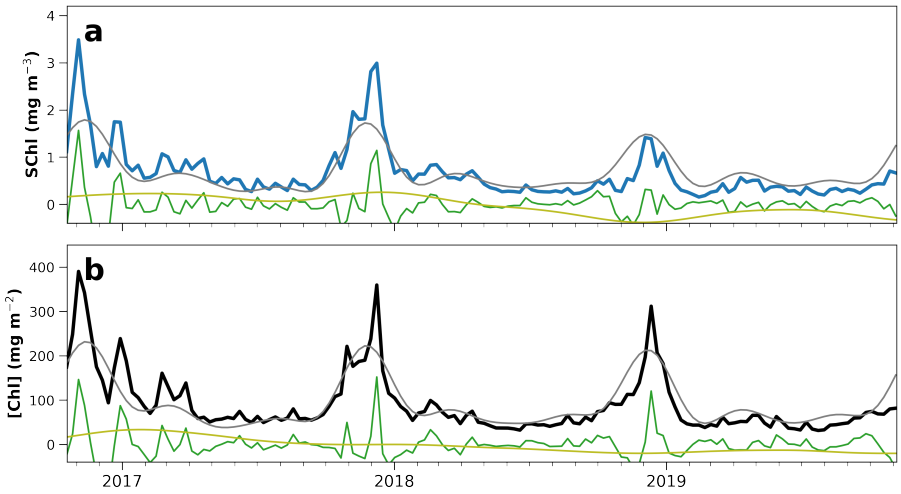

Figure 5.16. Timeseries decomposition of float 6902737 (a) SChl, full signal in blue, and (b) [Chl_{tot}], full signal in black. In both panels the seasonal component is gray, the sub-seasonal component is green, and the multi-annual component is gold.

Chapter 6

Summary and Conclusions

The multi-scale nature of ocean physics and biogeochemistry poses challenges for both observational oceanography and climate modeling. On the observational side, it is simply impossible to collect enough measurements to resolve all of the scales relevant to ocean dynamics and biogeochemical cycling. Therefore, any analysis of in situ data must grapple with the aliasing of variability at scales other than the signal of interest. On the modeling side, the computational cost to run a climate model typically requires a trade off between spatial and temporal resolution—multi-decadal simulations that capture long-term changes in ocean state are coarse and imperfectly parameterize the effects of many key processes, while submesoscale-resolving simulations are either confined to regional domains or short timespans. However, recent advancements in observational technology and computational tools are pushing the boundary on the questions that we are able to address as a scientific community.

This thesis is a small contribution to that end, utilizing novel autonomous float measurements and a state-of-the-art data assimilating model to explore the coupling between physical and biogeochemical processes in the Southern Ocean. In particular, we showed the importance of flow-topography interactions to phytoplankton distribution (Chapter 2), the limitations of eddy diffusion parameterizations for biogeochemical tracers (Chapter 3), the role of mixed-layer entrainment in driving basin asymmetry of air-sea carbon exchange (Chapter 4), and the impact of sub-seasonal events on year-to-year variations of primary productivity (Chapter 5). Many of

these results stemmed from the availability of new measurements in regions with limited historical data. This highlights the critical need for expanded data coverage and sustained long-term observations, particularly in locations with global influence such as the Southern Ocean.

Naturally, many questions are left unanswered as well as new questions raised by this thesis. The most pressing of these include: How does heterogenity of carbon outgassing impact the response of the Southern Ocean carbon sink to climate forcing? What are the precise mechanisms that drive sub-seasonal chlorophyll fluctuations? And more broadly, how does low frequency variability modulate the prevalence and magnitude of extreme events? A common thread is trying to understand how disparate space and time scales project onto one another. Characterizing these scale interactions is a prerequisite to identifying trends associated with anthropogenic climate change.

Therefore, although this thesis has focused on natural variability of phytoplankton biomass and carbon system parameters, it is motivated by understanding long-term changes. Multi-decadal changes in ocean heat content, primary production and carbon fluxes have been observed (Gille, 2002; Behrenfeld et al., 2006; Schmidtko et al., 2014; Landschützer et al., 2015). However, separating the effects of internal variability and anthropogenic forcing is difficult. Here, we have explored several mechanisms, operating at different scales, which lead to spatial and temporal heterogeneity in biogeochemical tracers. These patterns should be considered in the context of trend detection and time of emergence for anthropogenic signals. Furthermore, additional research on the drivers of these patterns is necessary to understand both the natural variability and forced trend. Future work on these processes is crucial given the key role of the Southern Ocean in the global climate system.

References

Abernathey, R. P., Cerovečki, I., Holland, P. R., Newsom, E., Mazloff, M. R., & Talley, L. D. (2016). Water-mass transformation by sea ice in the upper branch of the Southern Ocean overturning. *Nature Geoscience*, *9*, 596–601.

Abraham, E. R. (1998). The generation of plankton patchiness by turbulent stirring. *Nature*, *391*, 577–580.

Allen, M. R., & Smith, L. A. (1996). Monte Carlo SSA: Detecting irregular oscillations in the presence of colored noise. *Journal of Climate*, *9*, 3373–3404.

Anav, A., Friedlingstein, P., Kidston, M., Bopp, L., Ciais, P., Cox, P., Jones, C., Jung, M., Myneni, R., & Zhu, Z. (2013). Evaluating the land and ocean components of the global carbon cycle in the CMIP5 earth system models. *Journal of Climate*, *26*, 6801–6843.

Anderson, R. F., Ali, S., Bradtmiller, L. I., Nielsen, S. H. H., Fleisher, M. Q., Anderson, B. E., & Burckle, L. H. (2009). Wind-driven upwelling in the Southern Ocean and the deglacial rise in atmospheric co_2. *Science*, *323*, 1443–1448.

Ardyna, M., Claustre, H., Sallée, J.-B., D'Ovidio, F., Gentili, B., van Dijken, G., D'Ortenzio, F., & Arrigo, K. R. (2017). Delineating environmental control of phytoplankton biomass and phenology in the southern ocean. *Geophysical Research Letters*, *44*, 5016–5024.

Arrigo, K. R., van Dijken, G. L., & Bushinsky, S. (2008). Primary production in the Southern Ocean, 1997-2006. *Journal of Geophysical Research: Oceans*, *113*, C08004.

Arteaga, L. A., Boss, E., Behrenfeld, M. J., Westberry, T. K., & Sarmiento, J. L. (2020). Seasonal modulation of phytoplankton biomass in the Southern Ocean. *Nature Communications*, *11*, 5364.

Atkinson, A., Siegel, V., Pakhomov, E., & Rothery, P. (2004). Long-term decline in krill stock and increase in salps within the Southern Ocean. *Nature*, *432*, 100–103.

Atkinson, A., Whitehouse, M. J., Priddle, J., Cripps, G. C., Ward, P., & Brandon, M. A. (2001). South Georgia, Antarctica: a productive, cold water, pelagic ecosystem. *Marine Ecology Progress Series*, *216*, 279–308.

Atlas, R., Hoffman, R. N., Ardizzone, J., Leidner, S. M., Jusem, J. C., Smith, D. K., & Gombos, D. (2011). A cross-calibrated, multiplatform ocean surface wind velocity product for meteorological and oceanographic applications. *Bulletin of the American Meteorological Society*, *92*, 157–174.

Aumont, O., Ethe, C., Tagliabue, A., Bopp, L., & Gehlen, M. (2015). PISCES-v2: an ocean biogeochemical model for carbon and ecosystem studies. *Geoscientific Model Development*, *8*, 2465–2513.

Balwada, D., Speer, K. G., LaCasce, J. H., Owens, W. B., Marshall, J., & Ferrari, R. (2016). Circulation and stirring in the southeast Pacific Ocean and the Scotia Sea sectors of the Antarctic Circumpolar Current. *Journal of Physical Oceanography*, *46*, 2005–2027.

Barré, N., Provost, C., Sennechaell, N., & Lee, J. H. (2008). Circulation in the Ona Basin, southern Drake Passage. *Journal of Geophysical Research*, *113*, C04033.

Beadling, R. L., Russell, J. L., Stouffer, R. J., Mazloff, M., Talley, L. D., Goodman, P. J., Sallée, J.-B., Hewitt, H. T., Hyder, P., & Pandde, A. (2020). Representation of Southern Ocean properties across coupled model intercomparison project generations: CMIP3 to CMIP6. *Journal of Climate*, *33*, 6555–6581.

Behrenfeld, M. J. (2010). Abandoning sverdrup's critical depth hypothesis on phytoplankton blooms. *Ecology*, *91*, 977–989.

Behrenfeld, M. J., & Boss, E. S. (2014). Resurrecting the ecological underpinnings of ocean plankton blooms. *Annual Review of Marine Science*, *6*, 167–194.

Behrenfeld, M. J., O'Malley, R. T., Siegel, D. A., McClain, C. R., Sarmiento, J. L., Feldman, G. C., Milligan, A. J., Falkowski, P. G., Letelier, R. M., & Boss, E. S. (2006). Climate-driven trends in contemporary ocean productivity. *Nature*, *444*, 752–755.

Bhamidipati, N., Souza, A. N., & Flierl, G. R. (2020). Turbulent mixing of a passive scalar in the ocean mixed layer. *Ocean Modelling*, *149*, 101615.

Blain, S., Quéguiner, B., Armand, L., Belviso, S., Bombled, B., Bopp, L., Bowie, A., Brunet, C., Brussaard, C., Carlotti, F., Christaki, U., Corbiere, A., Durand, I., Ebersbach, F., Fuda, J.-L., Garcia, N., Gerringa, L., Griffiths, B., Guigue, C., Guillerm, C., Jacquet, S., Jeandel, C., Laan, P., Lefèvre, D., Lo Monaco, C., Malits, A., Mosseri, J., Obernosterer, I., Park, Y.-H., Picheral, M., Pondaven, P., Remenyi, T., Sandroni, V., Sarthou, G., Savoye, N., Scouarnec, L., Souhaut, M., Thuiller, D., Timmermans, K., Trull, T., Uitz, J., van Beek, P., Veldhuis, M., Vincent, D., Viollier, E., L., V., & Wagener, T. (2007). Effect of natural iron fertilization on carbon sequestration in the Southern Ocean. *Nature*, *446*, 1070–1074.

Bopp, L., Lévy, M., Resplandy, L., & Sallée, J.-B. (2015). Pathways of anthropogenic carbon subduction in the global ocean. *Geophysical Research Letters*, *42*, 6416–6423.

Boyd, P. W., Doney, S. C., Strzepek, R., Dusenberry, J., Lindsay, K., & Fung, I. (2008). Climate-mediated changes to mixed-layer properties in the Southern Ocean: assessing the phytoplankton response. *Biogeosciences*, *5*, 847–864.

Brentnall, S., Richards, K., & Brindley, J. (2003). Plankton patchiness and its effect on larger-scale productivity. *Journal of Plankton Research*, *25*, 121–140.

Brody, S. R., & Lozier, M. S. (2015). Characterizing upper-ocean mixing and its effect on the spring phytoplankton bloom with in situ data. *ICES Journal of Marine Science*, *72*, 1961–1970.

Broecker, W. S., & Peng, T.-H. (1982). *Tracers in the Sea*. Eldigio Press.

Bronselaer, B., Zanna, L., Munday, D. R., & Lowe, J. (2018). Southern Ocean carbon-wind stress feedback. *Climate Dynamics*, *51*, 2743–2757. doi: 10.1007/s00382-017-4041-y

Busecke, J. J. M., & Abernathey, R. P. (2019). Ocean mesoscale mixing linked to climate variability. *Science Advances*, *5*, eaav5014.

Bushinsky, S. M., Landschützer, P., Rödenbeck, C., Gray, A. R., Baker, D., Mazloff, M. R., Resplandy, L., Johnson, K. S., & Sarmiento, J. L. (2019). Reassessing Southern Ocean air-sea CO_2 flux estimates with the addition of biogeochemical float observations. *Global Biogeochemical Cycles*, *33*, 1370–1388.

Campbell, J. W. (1995). The lognormal distribution as a model for bio-optical variability in the sea. *Journal of Geophysical Research: Oceans*, *100*, 13237–13254.

Carranza, M. M., & Gille, S. T. (2015). Southern ocean wind-driven entrainment enhances satellite chlorophyll-a through the summer. *Journal of Geophysical Research: Oceans*, *120*, 304–323.

Carranza, M. M., Gille, S. T., Franks, P. J. S., Johnson, K. S., Pinkel, R., & Girton, J. B. (2018). When mixed layers are not mixed: Storm-driven mixing and bio-optical vertical gradients in mixed layers of the Southern Ocean. *Journal of Geophysical Research: Oceans*, *123*, 7264–7289.

Carter, B. R., Feely, R. A., Williams, N. L., Dickson, A. G., Fong, M. B., & Takeshita, Y. (2017). Updated methods for global locally interpolated estimation of alkalinity, pH, and nitrate. *Limnology and Oceanography Methods*, *16*, 119–131.

Carvalho, F., Kohut, J., Oliver, M. J., & Schofield, O. (2017). Defining the ecologically relevant mixed-layer depth for Antarctica's coastal seas. *Geophysical Research Letters*, *44*, 338–345.

Cerovečki, I., & Mazloff, M. R. (2015). The spatiotemporal structure of diabatic processes governing the evolution of Subantarctic Mode Water in the Southern Ocean. *Journal of*

Climate, *46*, 683–710.

Cerovečki, I., Meijers, A. J., Mazloff, M. R., Gille, S. T., Tamsitt, V., & Holland, P. R. (2019). The effects of enhanced sea ice export from the Ross Sea on recent cooling and freshening of the Southeast Pacific. *Journal of Climate*, *32*, 2013–2035.

Cerovečki, I., Talley, L. D., & Mazloff, M. R. (2011). A comparison of Southern Ocean air-sea buoyancy flux from an ocean state estimate with five other products. *Journal of Climate*, *24*, 6283–6306.

Chapman, C. C., Lea, M.-A., Meyer, A., Sallée, J.-B., & Hindell, M. (2020). Defining Southern Ocean fronts and their influence on biological and physical processes in a changing climate. *Nature Climate Change*, *10*, 209–219.

Chen, H., Haumann, F. A., Talley, L. D., Johnson, K. S., & Sarmiento, J. L. (submitted). The deep ocean's carbon exhaust. *Global Biogeochemical Cycles*. doi: https://doi.org/10.1002/essoar.10507757.1

Cramer, J. S. (1987). Mean and variance of r^2 in small and moderate samples. *Journal of Econometrics*, *35*, 253–266.

Cravatte, S., Serazin, G., Penduff, T., & Menkes, C. (2021). Imprint of chaotic ocean variability on transports in the southwestern Pacific at interannual timescales. *Ocean Science*, *17*, 487–507.

Cushing, D. H. (1975). *Marine ecology and fisheries*. Cambridge: Cambridge University Press.

D'Asaro, E. A., Thomson, J., Shcherbina, A. Y., Harcourt, R. R., Cronin, M. F., Hemer, M. A., & Fox-Kemper, B. (2014). Quantifying upper ocean turbulence driven by surface waves. *Geophysical Research Letters*, *41*, 102–107.

da Silva, C. B., & Pereira, J. C. F. (2007). Analysis of the gradient-diffusion hypothesis in large-eddy simulations based on transport equations. *Physics of Fluids*, *19*, 035106.

de Baar, H. J. W., de Jong, J., Baaker, D., Loscher, B. M., Veth, C., Bathmann, U., & Smetacek, V. (1995). Importance of iron for plankton blooms and carbon dioxide drawdown in the Southern Ocean. *Nature*, *373*, 412–415.

de Boyer Montégut, C., Madec, G., Fischer, A. S., & Lazar, A. (2004). Mixed layer depth over the global ocean: An examination of profile data and a profile-based climatology. *Journal of Geophysical Research*, *109*, C12003.

de Jong, J., Schoemann, V., Lannuzel, D., Croot, P., de Barr, H., & Tison, J.-L. (2012). Natural iron fertilization of the Atlantic sector of the Southern Ocean by continental shelf sources of the Antarctic Peninsula. *Journal of Geophysical Research: Oceans*, *117*, G01029.

Denman, K. L. (2003). Modelling plankton ecosystems: Parameterizing complexity. *Progress in Oceanography*, *57*, 429–452.

DeVries, T., Holzer, M., & Primeau, F. (2017). Recent increase in oceanic carbon uptake driven by weaker upper-ocean overturning. *Nature*, *542*, 215–218. doi: 10.1038/nature21068

Doney, S. C., Lindsay, K., Caldeira, K., Campin, J.-M., Drange, H., Dutay, J.-C., & et al. (2004). Evaluating global ocean carbon models: The importance of realistic physics. *Global Biogeochemical Cycles*, *18*, GB3017. doi: 10.1029/2003GB002150

Dong, S., Sprintall, J., Gille, S. T., & Talley, L. D. (2008). Southern Ocean mixed-layer depth from Argo float profiles. *Journal of Geophysical Research: Oceans*, *113*, C06013.

Dower, J., Freeland, H., & Juniper, K. (1992). A strong biological response to oceanic flow past Cobb Seamount. *Deep-Sea Research I*, *39*, 1139–1145.

Dulaiova, H., Ardelan, M. V., Henderson, P. B., & Charette, M. A. (2009). Shelf-derived iron inputs drive biological productivity in the southern Drake Passage. *Global Biogeochemical Cycles*, *23*, GB4014.

du Plessis, M., Swart, S., Ansorge, I. J., & Mahadevan, A. (2017). Submesoscale processes promote seasonal restratification in the Subantarctic Ocean. *Journal of Geophysical Research: Oceans*, *122*, 2960–2975.

du Plessis, M., Swart, S., Ansorge, I. J., Mahadevan, A., & Thompson, A. F. (2019). Southern Ocean seasonal restratification delayed by submesoscale wind-front interactions. *Journal of Physical Oceanography*, *49*, 1035–1053.

Falkowski, P. G., Ziemann, D., Kolber, Z., & Beinfang, P. K. (1991). Role of eddy pumping in enhancing primary production in the ocean. *Nature*, *352*, 55–58.

Fasham, M. J. R., Ducklow, H. W., & McKelvie, S. M. (1990). A nitrogen-based model of plankton dynamics in the oceanic mixed layer. *Journal of Marine Research*, *48*, 591–639.

Ferrari, R., & Nikurashin, M. (2010). Suppression of eddy diffusivity across jets in the southern ocean. *Journal of Physical Oceanography*, *40*, 1501–1519.

Firing, Y., Chereskin, T. K., & Mazloff, M. R. (1982). The net transport of the Antarctic Circumpolar Current through Drake Passage. *Journal of Physical Oceanography*, *12*, 960–971.

Firing, Y., Chereskin, T. K., & Mazloff, M. R. (2011). Vertical structure and transport of the Antarctic Circumpolar Current in Drake Passage from direct velocity measurements. *Journal of Geophysical Research*, *116*, C018015.

Flierl, G. R., & Davis, C. S. (1993). Biological effects of Gulf Stream meandering. *Journal of*

Marine Research, *51*, 529–560.

Flierl, G. R., & McGillicuddy, D. J. (2002). Mesoscale and submesoscale physical-biological interactions. *The Sea - Ideas and Observations on Progress in the Study of the Seas*, *12*, 113–185.

Fox-Kemper, B., Adcroft, A., Boning, C. W., Chassignet, E. P., Curchitser, E., Danabasoglu, G., & et al. (2019). Challenges and prospects in ocean circulation models. *Frontiers in Marine Science*, *6*, 65.

Fox-Kemper, B., Ferrari, R., & Hallberg, R. (2008). Parameterization of mixed layer eddies. part i: Theory and diagnosis. *Journal of Physical Oceanography*, *38*, 1145–1165.

Fragoso, G. M., & Smith, W. O. (2012). Influence of hydrography on phytoplankton distribution in the amundsen and ross seas, antarctica. *Journal of Marine Systems*, *89*, 19–29.

Franks, P. J. S. (2002). NPZ Models of Plankton Dynamics: Their Construction, Coupling to Physics, and Application. *Journal of Oceanography*, *58*(2), 379–387.

Franks, P. J. S. (2015). Has Sverdrup's critical depth hypothesis been tested? Mixed layers vs. turbulent layers. *ICES Journal of Marine Science*, *72*, 1897–1907.

Frants, M., Gille, S. T., Hatta, M., Hiscock, W. T., Kahru, M., & Measures, C. I. (2013). Analysis of horizontal and vertical processes contributing to natural iron supply in the mixed layer in southern Drake Passage. *Deep-Sea Research II*, *90*, 68–76.

Freilich, M., & Mahadevan, A. (2021). Coherent pathways for subduction from the surface mixed layer at ocean fronts. *Journal of Geophysical Research: Oceans*, *126*, e2020JC017042.

Freilich, M. A., & Mahadevan, A. (2019). Decomposition of vertical velocity for nutrient transport in the upper ocean. *Journal of Physical Oceanography*, *49*(6), 1561–1575.

Frenger, I., Münnich, M., & Gruber, N. (2018). Imprint of Southern Ocean mesoscale eddies on chlorophyll. *Biogeosciences*, *15*, 4781–4798.

Friedlingstein, P., O'Sullivan, M., Jones, M. W., Andrew, R. M., Hauck, O. A. P.-G. P. P. W., J., Pongratz, J., Sitch, S., Le Quéré, C., Canadell, J. G., Ciais, P., Jackson, R. B., Alin, S., Aragão, L. E. O. C., Arneth, A., Arora, V., Bates, N. R., Becker, M., Benoit-Cattin, A., Bittig, H. C., Bopp, L., Bultan, S., Chandra, N., Chevallier, F., Chini, L. P., Evans, W., Florentie, L., Forster, P. M., Gasser, T., Gehlen, M., Gilfillan, D., Gkritzalis, T., Gregor, L., Gruber, N., Harris, I., Hartung, K., Haverd, V., Houghton, R. A., Ilyina, T., Jain, A. K., Joetzjer, E., Kadono, K., Kato, E., Kitidis, V., Korsbakken, J. I., Landschützer, P., Lefèvre, N., Lenton, A., Lienert, S., Liu, Z., Lombardozzi, D., Marland, G., Metzl, N., Munro, D. R., Nabel, J. E. M. S., Nakaoka, S.-I., Niwa, Y., O'Brien, K., Ono, T., Palmer, P. I., Pierrot, D., Poulter, B., Resplandy, L., Robertson, E., Rödenbeck, C., Schwinger, J.,

Séférian, R., Skjelvan, I., Smith, A. J. P., Sutton, A. J., Tanhua, T., Tans, P. P., Tian, H., Tilbrook, B., van der Werf, G., Vuichard, N., Walker, A. P., Wanninkhof, R., Watson, A. J., Willis, D., Wiltshire, A. J., Yuan, W., Yue, X., & Zaehle, S. (2020). Global Carbon Budget 2020. *Earth System Science Data*, *12*, 3269–3340.

Frölicher, T. L., Sarmiento, J. L., Paynter, D. J., Dunne, J. P., Krasting, J. P., & Winton, M. (2015). Dominance of the Southern Ocean in anthropogenic carbon and heat uptake in CMIP5 models. *Journal of Climate*, *28*, 862–886. doi: 10.1175/JCLI-D-14-00117.1

Ganachaud, A., & Wunsch, C. (2002). Oceanic nutrient and oxygen transports and bounds on export production during the World Ocean Circulation Experiment. *Global Biogeochemical Cycles*, *16*(4), 1057.

Gent, P. R., Willebrand, J., McDougall, T. J., & McWilliams, J. C. (1995). Parameterizing eddy-induced tracer transports in ocean circulation models. *Journal of Physical Oceanography*, *25*, 463–474.

Gille, S. T. (2002). Warming of the Southern Ocean since the 1950s. *Science*, *295*, 1275–1277.

Gille, S. T., Carranza, M. M., Cambra, R., & Morrow, R. (2014). Wind-induced upwelling in the Kerguelen Plateau region. *Biogeosciences*, *11*, 6389–6400.

Gower, J. F. R., Denman, K. L., & Holyer, R. L. (1980). Phytoplankton patchiness indicates the fluctuations spectrum of mesoscale oceanic structure. *Nature*, *288*, 157–159.

Graff, J. R., & Behrenfeld, M. J. (2018). Photoacclimation responses in subarctic Atlantic phytoplankton following a natural mixing-restratification event. *Frontiers in Marine Science*, *5*, 209.

Graham, R. M., De Boer, A. M., van Sebille, E., Kohfeld, K. E., & Schlosser, C. (2015). Inferring source regions and supply mechanisms of iron in the Southern Ocean from satellite chlorophyll data. *Deep Sea Research Part I: Oceanographic Research Papers*, *104*, 9–25.

Gray, A. R., Johnson, K. S., Bushinsky, S. M., Riser, S. C., Russell, J. L., Talley, L. D., Wanninkhof, R., Williams, N. L., & Sarmiento, J. L. (2018). Autonomous biogeochemical floats detect significant carbon dioxide outgassing in the high-latitude southern ocean. *Geophysical Research Letters*, *45*, 9049–9057.

Gray, A. R., & Riser, S. (2014). A global analysis of Sverdrup Balance using absolute geostrophic velocities from Argo. *Journal of Physical Oceanography*, *44*, 1213–1229.

Greaves, B. L., Davidson, A. T., Fraser, A. D., McKinlay, J. P., Martin, A., McMinn, A., & Wright, S. W. (2020). The Southern Annular Mode (SAM) influences phytoplankton communities in the seasonal ice zone of the Southern Ocean. *Biogeosciences*, *17*, 3815–

3835.

Gregg, W. W., & Rousseaux, C. S. (2019). Global ocean primary production trends in the modern ocean color satellite record (1998-2015). *Environmental Research Letters*, *14*, 124011.

Grenier, M., Della Penna, A., & Trull, T. W. (2015). Autonomous profiling float observations of the high-biomass plume downstream of the Kerguelen Plateau in the Southern Ocean. *Biogeosciences*, *12*, 2707-–2735.

Gruber, N., Gloor, M., Fletcher, S. E. M., Doney, S. C., Dutkiewicz, S., & Follows, M. J. (2009). Oceanic sources, sinks, and transport of atmospheric CO_2. *Global Biogeochemical Cycles*, *23*, GB1005.

Gruber, N., Landschützer, P., & Lovenduski, N. S. (2019). The variable Southern Ocean carbon sink. *Annual Review of Marine Science*, *11*, 159–186. doi: 10.1146/annurev-marine-121916-063407

Haëntjens, N., Boss, E., & Talley, L. D. (2017). Revisiting Ocean Color algorithms for chlorophyll a and particulate organic carbon in the Southern Ocean using biogeochemical floats. *Journal of Geophysical Research: Oceans*, *122*, 6583–6593.

Hamlington, P. E., Roekel, P. V., Fox-Kemper, B., Julien, K., & Chini, G. P. (2014). Langmuir-submesoscale interactions: Descriptive analysis of multiscale frontal spin-down simulations. *Journal of Physical Oceanography*, *44*, 2249–2272.

Hatta, M., Measures, C. I., Selph, K. E., Zhou, M., & Hiscock, W. T. (2013). Iron fluxes from the shelf regions near the South Shetland Islands in the Drake Passage during the austral-winter 2006. *Deep-Sea Research II*, *90*, 89–101.

Heinze, C., Meyer, S., Goris, N., Anderson, L., Steinfeldt, R., Chang, N., Le Quéré, C., & Bakker, D. C. E. (2015). The ocean carbon sink: impacts, vulnerabilities and challenges. *Earth System Dynamics*, *6*, 327–358.

Hell, M., Cornuelle, B. D., Gille, S. T., & Lutsko, N. J. (2021). Time-varying empirical probability densities of Southern Ocean surface winds: linking the leading mode to SAM and quantifying wind product differences. *Journal of Climate*, *34*, 5497–5522.

Henson, S. A., Sarmiento, J. L., Dunne, J. P., Bopp, L., Lima, I., Doney, S. C., John, J., & Beaulieu, C. (2010). Detection of anthropogenic climate change in satellite records of ocean chlorophyll and productivity. *Biogeosciences*, *7*, 621–640.

Hersbach, H., Bell, B., Berrisford, P., Hirahara, S., Horányi, A., Munoz-Sabater, J., Nicolas, J., Peubey, C., Radu, R., Schepers, D., Simmons, A., Soci, C., Abdalla, S., Abellan, X., Balsamo, G., Bechtold, P., Biavati, G., Bidlot, J., Bonavita, M., De Chiara, G., Dahlgren,

P., Dee, D., Diamantakis, M., Dragani, R., Flemming, J., Forbes, R., Fuentes, M., Geer, A., Haimberger, L., Healy, S., Hogan, R. J., Hólm, E., Janisková, M., Keeley, S., Laloyaux, P., Lopez, P., Lupu, C., Radnoti, G., de Rosnay, P., Rozum, I., Vamborg, F., Villaume, S., & Thépaut, J.-N. (2020). The ERA5 global reanalysis. *Quaterly Journal of the Royal Meteorological Society*, *146*, 1999–2049.

Hewes, C. D., Reiss, C. S., Kahru, M., Mitchell, B. G., & Holm-Hansen, O. (2008). Control of phytoplankton biomass by dilution and mixed layer depth in the western Weddell-Scotia Confluence. *Marinee Ecology Progress Series*, *366*, 15–29.

Ho, D. T., Law, C. S., Smith, M. J., Schlosser, P., Harvey, M., & Hill, P. (2006). Measurements of air-sea gas exchange at high wind speeds in the Southern Ocean: Implications for global parameterizations. *Geophysical Research Letters*, *33*, 7384.

Hodges, B. A., & Rudnick, D. L. (2004). Simple models of steady deep maxima in chlorophyll and biomass. *Deep-Sea Research I: Oceanographic Research Papers*, *51*, 999–1015.

Hodges, B. A., & Rudnick, D. L. (2006). Horizontal variability in chlorophyll fluorescence and potential temperature. *Deep-Sea Research I: Oceanographic Research Papers*, *53*, 1460–1482.

Hofmann, E. E., Klinck, J. M., Locarnini, R. A., Fach, B., & Murphy, E. (1998). Krill transport in the Scotia Sea and environs. *Antarctic Science*, *10*, 406–415.

Holm-Hansen, O., Naganobu, M., Kawaguchi, S., Kameda, T., Krasovski, I., Tchernyshkov, P., Priddle, J., Korb, R., Brandon, M., Demer, D., Hewitt, R. P., Kahru, M., & Hewes, C. D. (2004). Factors influencing the distribution, biomass, and productivity of phytoplankton in the Scotia Sea and adjoininng waters. *Deep Sea Research II*, *51*, 1333–1350.

Holte, J., & Talley, L. D. (2009). A new algorithm for finding mixed layer depths with applications to Argo data and Subantarctic Mode Water formation. *Journal of Atmospheric and Oceanic Technology*, *26*, 1920–1939.

Huisman, J., & Weissing, F. J. (2001). Biological conditions for oscillations and chaos generated by multispecies competition. *Ecology*, *82*, 2682–2695.

Humphreys, M. P., Gregor, L., Pierrot, D., van Heuven, S. M. A. C., Lewis, E. R., & Wallace, D. W. R. (2020). PyCO2SYS: marine carbonate system calculations in Python. *Zenodo*. doi: 10.5281/zenodo.3744275

Huppert, H. E. (1975). Some remarks on the initiation of inertial Taylor columns. *Journal of Fluid Mechanics*, *67*, 397–412.

Ito, T., & Follows, M. (2003). Upper ocean control on the solubility pump of CO_2. *Journal of Marine Research*, *61*, 465-489.

Ito, T., Woloszyn, M., & Mazloff, M. (2010). Anthropogenic carbon dioxide transport in the Southern Ocean driven by Ekman flow. *Nature*, *463*, 80–83.

Jenkins, W. J. (1988). Nitrate flux into the euphotic zone near bermuda. *Nature*, *331*, 521.

Jiang, M., Measures, C. I., Barbeau, K. A., Charette, M. A., Gille, S. T., Hatta, M., Kahru, M., Mitchell, B. G., Naveira Garabato, A. C., Reiss, C., Selph, K., & Zhou, M. (2019). Fe sources and transport from the Antarctic Peninsula shelf to the southern Scotia Sea. *Deep-Sea Research I*, *150*, 103060.

Johnson, K. S., Plant, J. N., Coletti, L. J., Jannasch, H. W., Sakamoto, C. M., Riser, S. C., & et al. (2017a). Biogeochemical sensor performance in the soccom profiling float array. *Journal of Geophysical Research: Oceans*, *122*, 6416–6436.

Johnson, K. S., Plant, J. N., Coletti, L. J., Jannasch, H. W., Sakamoto, C. M., Riser, S. C., Swift, D. D., Williams, N. L., Boss, E., Haëntjens, N., Talley, L. D., & Sarmiento, J. L. (2017b). Biogeochemical sensor performance in the SOCCOM profiling float array. *Journal of Geophysical Research: Oceans*, *122*(8), 6416–6436.

Jones, D. C., Ito, T., Takano, Y., & Hsu, W.-C. (2014). Spatial and seasonal variability of the air-sea equilibration timescale of carbon dioxide. *Global Biogeochemical Cycles*, *28*, 1163–1178.

Kahru, M., & Mitchell, B. G. (2010). Blending of ocean colour algorithms applied to the Southern Ocean. *Remote Sensing Letters*, *1*, 119–124.

Kahru, M., Mitchell, B. G., Gille, S. T., Hewes, C. D., & Holm-Hansen, O. (2007). Eddies enhance biological production in the Weddell-Scotia confluence of the Southern Ocean. *Geophysical Research Letters*, *34*, L14603.

Keerthi, M. G., Lévy, M., & Aumont, O. (2021). Intermittency in phytoplankton bloom triggered by modulations in vertical stability. *Scientific Reports*, *11*, 1285.

Keerthi, M. G., Lévy, M., Aumont, O., Lengaigne, M., & Antoine, D. (2020). Contrasted contribution of intraseasonal time scales to surface chlorophyll variations in a bloom and an oligotrophic regime. *Journal of Geophysical Research: Oceans*, *125*, e2019JC015701.

Keerthi, M. G., Prend, C. J., Lévy, M., & Aumont, O. (submitted). Small spatio-temporal scales are key players of year-to-year phytoplankton changes. *Nature Geoscience*.

Keppler, L., & Landschützer, P. (2019). Regional wind variability modulates the Southern Ocean carbon sink. *Scientific Reports*, *9*, 7384.

Keppler, L., Landschützer, P., Gruber, N., Lauvset, S. K., & Stemmler, I. (2020). Seasonal carbon dynamics in the near-global ocean. *Global Biogeochemical Cycles*, *34*, e2020GB006571.

Khatiwala, S., Primeau, F., & Hall, T. (2009). Reconstruction of the history of anthropogenic CO_2 concentrations in the ocean. *Nature*, *462*, 346–349. doi: 10.1038/nature08526

Kim, Y. S., & Orsi, A. H. (2014). On the variability of Antarctic Circumpolar Current fronts inferred from 1992-2011 altimetry. *Journal of Physical Oceanography*, *44*, 3054–3071.

King, B., Stone, M., Zhang, H. P., Gerkema, T., Marder, M., Scott, R. B., & Swinney, H. L. (2012). Buoyancy frequency profiles and internal semidiurnal tide turning depths in the oceans. *Journal of Geophysical Research*, *117*, C04008.

Kunze, E., Firing, E., Hummon, J. M., Chereskin, T. K., & Thurnherr, A. M. (2006). Global abyssal mixing inferred from lowered ADCP shear and CTD strain profiles. *Science*, *36*, 1553–1576.

Kuusela, M., & Stein, M. L. (2018). Locally stationary spatio-temporal interpolation of Argo profiling float data. *Proceedings of the Royal Society A*, *474*, 20180400.

Lacelot, C., de Montety, A., Goosse, H., Becquevort, S., Schoemann, V., Pasquer, B., & Vancoppenolle, M. (2009). Spatial distribution of the iron supply to phytoplankton in the Southern Ocean: A model study. *Biogeosciences*, *6*, 2861–2878.

Landschützer, P., Gruber, N., Haumann, F. A., Rödenbeck, C., Bakker, D. C. E., van Heuven, S., & *et al.* (2015). The reinvigoration of the southern ocean carbon sink. *Science*, *349*, 1221–1224.

Large, W. G., McWilliams, J. C., & Doney, S. C. (1994). Oceanic vertical mixing: A review and a model with a nonlocal boundary layer parameterization. *Reviews of Geophysics*, *32*, 363–403.

Laurindo, L., Mariano, A., & Lumpkin, R. (2017). An improved near-surface velocity climatology for the global ocean from drifter observations. *Deep-Sea Research I*, *124*, 73–92.

Lee, M., Marshall, D., & Williams, R. (1997). On the eddy transfer of tracers: Advective or diffusive? *Journal of Marine Research*, *55*, 483–505.

Le Quéré, C., Andres, R. J., Boden, T., Conway, T., Houghton, R. A., House, J. I., Marland, G., Peters, G. P., van der Werf, G. R., Ahlström, A., Andrew, R. M., Bopp, L., Canadell, J. G., Ciais, P., Doney, S. C., Enright, C., Friedlingstein, P., Huntingford, C., Jain, A. K., Jourdain, C., Kato, E., Keeling, R. F., Klein Goldewijk, K., Levis, S., Levy, P., Lomas, M., Poulter, B., Raupach, M. R., Schwinger, J., Sitch, S., Stocker, B. D., Viovy, N., Zaehle, S., & Zeng, N. (2013). The global carbon budget 1959–2011. *Earth System Science Data*, *5*, 165–185.

Le Quéré, C., Bopp, L., & Tegen, I. (2002). Antarctic circumpolar wave impact on marine

biology: A natural laboratory for climate change study. *Geophysical Research Letters*, *29*, 1407.

Le Quéré, C., Rödenbeck, C., Buitenhuis, E. T., Conway, T. J., Langenfelds, R., Gomez, A., Labuschagne, C., Ramonet, M., Nakazawa, T., Metzl, N., Gillett, N., & Heimann, M. (2007). Saturation of the Southern Ocean CO_2 sink due to recent climate change. *Science*, *316*, 1735–1738.

Lévy, M., Ferrari, R., Franks, P. J. S., Martin, A. P., & Rivière, P. (2012). Bringing physics to life at the submesoscale. *Geophysical Research Letters*, *39*, L14602.

Lévy, M., Franks, P. J. S., & Smith, K. S. (2018). The role of submesoscale currents in structuring marine ecosystems. *Nature Communications*, *9*, 4758.

Lévy, M., Klein, P., & Treguier, A.-M. (2001). Impact of sub-mesoscale physics on production and subduction of phytoplankton in an oligotrophic regime. *Journal of Marine Research*, *59*, 535–565.

Lévy, M., & Martin, A. P. (2013). The influence of mesoscale and submesoscale heterogeneity on ocean biogeochemical reactions. *Global Biogeochemical Cycles*, *27*, 1139–1150.

Lévy, M., Resplandy, L., & Lengaigne, M. (2014). Oceanic mesoscale turbulence drives large biogeochemical interannual variability at middle and high latitudes. *Geophysical Research Letters*, *41*, 2467–2474.

Li, Q., Reichl, B. G., Fox-Kemper, B., Adcroft, A. J., Belcher, S. E., & Danabasoglu, t., G. (2019). Comparing ocean surface boundary vertical mixing schemes including Langmuir turbulence. *Journal of Advances in Modeling Earth Systems*, *11*, 3545–3592.

Li, Z., Lozier, M. S., & Cassar, N. (2021). Linking Southern Ocean mixed-layer dynamics to Net Community Production on various timescales. *Journal of Geophysical Research: Oceans*, *126*, e2021JC017537.

Lightstone, M. F., & Raithby, G. D. (2009). On the validity of the gradient diffusion approach as applied to modelling particle dispersion in a turbulent gaseous flow. *The Canadian Journal of Chemical Engineering*, *78*, 478–485.

Liu, L. L., & Huang, R. X. (2012). The global subduction/obduction rates: Their interannual and decadal variability. *Journal of Climate*, *25*, 1096–1115.

Llort, J., Lévy, M., Sallée, J.-B., & Tagliabue, A. (2019). Nonmonotonic response of primary production and export to changes in mixed-layer depth in the Southern Ocean. *Geophysical Research Letters*, *46*, 3368–3377.

Lovenduski, N. S., & Gruber, N. (2005). Impact of the Southern Annular Mode on Southern Ocean circulation and biology. *Geophysical Research Letters*, *32*, L11603.

Lovenduski, N. S., Gruber, N., & Doney, S. C. (2008). Toward a mechanistic understanding of the decadal trends in the Southern Ocean carbon sink. *Global Biogeochemical Cycles*, *22*(3), GB3016. doi: 10.1029/2007GB003139

Mahadevan, A. (2016). The impact of submesoscale physics on primary productivity of plankton. *Annual Review of Marine Science*, *8*, 161–184.

Mahadevan, A., & Campbell, J. W. (2002). Biogeochemical patchiness at the sea surface. *Geophysical Research Letters*, *29*, 1926. doi: 10.1029/2001GL014116

Manucharyan, G. E., Thompson, A. F., & Spall, M. A. (2017). Eddy memory mode of multidecadal variability in residual-mean ocean circulations with application to the beaufort gyre. *Journal of Physical Oceanography*, *47*, 855–866.

Maraun, D., Kurths, J., & Holschneider, M. (2007). Nonstationary Gaussian processes in wavelet domain: Synthesis, estimation, and significance testing. *Physical Review E*, *75E*, 016707.

Marshall, D., & Marshall, J. (1995). On the thermodynamics of subduction. *Journal of Physical Oceanography*, *25*, 138–151.

Marshall, J., & Speer, K. (2012). Closure of the meridional overturning circulation through Southern Ocean upwelling. *Nature Geoscience*, *5*, 171–180.

Martin, A. (2003). Phytoplankton patchiness: The role of lateral stirring and mixing. *Progress in Oceanography*, *57*, 125–174.

Martin, A., Richards, K., Bracco, A., & Provenzale, A. (2002). Patchy productivity in the open ocean. *Global Biogeochemical Cycles*, *16*, 1025. doi: 10.1029/2001GB001449

Martinez, E., Antoine, D., D'Ortenzio, F., & Gentili, B. (2009). Climate-driven basin-scale decadal oscillations of oceanic phytoplankton. *Science*, *326*, 1253–1256.

Mashayek, A., Ferrari, R., Merrifield, S., Ledwell, J. R., St Laurent, L., & Naveira Garabato, A. C. (2017). Topographic enhancement of vertical turbulent mixing in the Southern Ocean. *Nature Communications*, *8*, 14197.

Mayersohn, B., Smith, S. K., Mangolte, I., & Lévy, M. (2021). Intrinsic timescales of variability in a marine plankton model. *Ecological Modelling*, *443*, 109446.

Mazloff, M. R., Heimbach, P., & Wunsch, C. (2010). An eddy permitting Southern Ocean state estimate. *Journal of Physical Oceanography*, *40*, 880–899.

McGillicuddy, D. J. (2016). Mechanisms of physical-biological-biogeochemical interaction at the oceanic mesoscale. *Annual Review of Marine Science*, *8*, 125–159.

McKiver, W., Neufeld, Z., & Scheuring, I. (2009). Plankton bloom controlled by horizontal

stirring. *Nonlinear Processes in Geophysics*, *16*, 623–630.

Measures, C. I., Brown, M. T., Selph, K. E., Apprill, A., Zhou, M., Hatta, M., & Hiscock, W. T. (2013). The influence of shelf processes in delivering dissolved iron to the HNLC waters of the Drake Passage, Antarctica. *Deep-Sea Research II*, *90*, 77–88.

Meier, W. N., Fetterer, F., Savoie, M., Mallory, S., Duerr, R., & Stroeve, J. (2017). NOAA/NSIDC Climate Data Record of Passive Microwave Sea Ice Concentration, Version 3, Boulder, CO USA. NSIDC: National Snow and Ice Data Center.

Meijers, A. J. S., Cerovečki, I., King, B. A., & Tamsitt, V. (2019). A see-saw in Pacific Subantarctic Mode Water formation driven by atmospheric modes. *Geophysical Research Letters*, *46*, 13152–13160.

Meredith, M. P., Meijers, A. S., Naveira Garabato, A. C., Brown, P. J., Venables, H. J., & Abrahamsen, E. P. (2015). Circulation, retention, and mixing of waters within the Weddell-Scotia Confluence, Southern Ocean: The role of stratified Taylor columns. *Journal of Geophysical Research*, *120*, 547–562.

Meredith, M. P., Watkins, J. L., Murphy, E. J., Cunningham, N. J., Wood, A. G., & Korb, R. (2003). An anticyclonic circulation above the Northwest Georgia Rise, Southern Ocean. *Geophysical Research Letters*, *30*, 2061.

Mitchell, B. G., Brody, E. A., Holm-Hansen, O., McClain, C., & Bishop, J. (1991). Light limitation of phytoplankton biomass and macronutrient utilization in the Southern Ocean. *Limnology and Oceanography*, *36*, 1662–1677.

Mitchell, B. G., & Holm-Hansen, O. (1991). Observations and modeling of the Antarctic phytoplankton crop in relation to mixing depth. *Deep Sea Research I*, *38*, 981–1007.

Mongin, M., Molina, E., & Trull, T. W. (2008). Seasonality and scale of the Kerguelen plateau phytoplankton bloom: A remote sensing and modeling analysis of the influence of natural iron fertilization in the Southern Ocean. *Deep-Sea Research II*, *55*, 880–892.

Mongwe, N. P., Vichi, M., & Monteiro, P. M. S. (2018). The seasonal cycle of pCO_2 and CO_2 fluxes in the Southern Ocean: diagnosing anomalies in CMIP5 Earth system models. *Biogeosciences*, *15*, 2851–2872.

Monteiro, P. M. S., Gregor, L., Lévy, M., Maenner, S., Sabine, C. L., & Swart, S. (2015). Intraseasonal variability linked to sampling alias in air-sea CO_2 fluxes in the Southern Ocean. *Geophysical Research Letters*, *42*, 8507–8514.

Mooney, C. J., & Wilson, J. D. (1993). Disagreements between gradient-diffusion and lagrangian stochastic dispersion models, even for sources near the ground. *Boundary-Layer Meteorology*, *64*, 291–296.

Morel, A., & Maritorena, S. (2001). Bio-optical properties of oceanic waters: A reappraisal. *Journal of Geophysical Research*, *106*, 7163–7180.

Murphy, E. J., Thorpe, S. E., Watkin, J. L., & Hewitt, R. (2004). Modeling the krill transport pathway in the Scotia Sea: Spatial and environmental connections generating the seasonal distribution of krill. *Deep Sea Research II*, *51*, 1435–1456.

Murphy, E. J., Watkins, J. L., Trathan, P. N., Reid, K., Meredith, M. P., Thorpe, S. E., Johnston, N. M., Clarke, A., Tarling, G. A., Collins, M. A., Forcada, J., Shreeve, R. S., Atkinson, A., Korb, R., Whitehouse, M. J., Ward, P., Rodhouse, P. G., Enderlein, P., Hirst, A. G., Martin, A. R., Hill, S. L., Staniland, I. J., Pond, D. W., Briggs, D. R., Cunningham, N. J., & Fleming, A. H. (2007). Spatial and temporal operation of the Scotia Sea ecosystem: a review of large-scale links in a krill centred food. *Philosophical Transactions of the Royal Society B*, *362*, 113–148.

Naveira Garabato, A. C., Polzin, K. L., King, B. A., Heywood, K. J., & Visbeck, M. (2004). Widespread intense turbulent mixing in the Southern Ocean. *Science*, *303*, 210–213.

Nicholson, S.-A., Lévy, M., Jouanno, J., Capet, X., Swart, S., & Monteiro, P. M. S. (2019). Iron supply pathways between the surface and subsurface waters of the Southern Ocean: From winter entrainment to summer storms. *Geophysical Research Letters*, *46*, 14567–14575.

Nicholson, S.-A., Whitt, D. B., Fer, I., du Plessis, M. D., Lebéhot, A. D., Swart, S., Sutton, A. J., & Monteiro, P. M. S. (2022). Storms drive outgassing of CO_2 in the subpolar Southern Ocean. *Nature Communications*, *13*, 158.

Omand, M. M., D'Asaro, E. A., Lee, C. M., Perry, M. J., Briggs, N., Cetinić, C., & Mahadevan, A. (2015). Eddy-driven subduction exports particulate organic carbon from the spring bloom. *Science*, *348*, 222–225.

Orsi, A. H., Whitworth III, T., & Nowlin Jr., W. D. (1995). On the meridional extent and fronts of the antarctic circumpolar current. *Deep-Sea Research I*, *42*, 641–673.

Papanicolaou, G., & Pironneau, O. (1981). On the asymptotic behavior of motion in random flows. In L. Arnold & R. Lefever (Eds.), *Stochastic nonlinear systems* (p. 36-41). Springer.

Pasquero, C. (2005). Differential eddy diffusion of biogeochemical tracers. *Geophysical Research Letters*, *32*, L17603. doi: 10.1029/2005GL023662

Pellichero, V., Boutin, J., Claustre, H., Merlivat, L., Salée, J.-B., & Blain, S. (2020). Relaxation of wind stress drives the abrupt onset of biological carbon uptake in the Kerguelen bloom: A multisensor approach. *Geophysical Research Letters*, *47*, e2019GL085992.

Perissinotto, R., & Duncombe Rae, C. M. (1990). Occurrence of anticyclonic eddies on the Prince Edward Plateau (Southern Ocean): Effects on phytoplankton biomass and production.

Deep-Sea Research I, *37*, 777–793.

Pierrehumbert, R. T. (1994). Tracer microstructure in the large-eddy dominated regime. *Chaos, Solitons and Fractals*, *4*, 1091–1110.

Pierrehumbert, R. T. (2000). Lattice models of advection-diffusion. *Chaos*, *10*, 61–74.

Platt, T., & Sathyendranath, S. (1988). Oceanic primary production: estimation by remote sensing at local and regional scales. *Science*, *241*, 1613–1620.

Plumb, R. (1979). Eddy fluxes of conserved quantities by small-amplitude waves. *Journal of Atmospheric Science*, *36*, 1699–1704.

Polzin, K. L., Toole, J. M., Ledwell, J. R., & Schmitt, R. W. (1997). Spatial variability of turbulent mixing in the abyssal ocean. *Science*, *276*, 93–96.

Prend, C. J., Gille, S. T., Talley, L. D., Mitchell, B. G., Rosso, I., & Mazloff, M. R. (2019). Physical drivers of phytoplankton bloom initiation in the Southern Ocean's Scotia Sea. *Journal of Geophysical Research: Oceans*, *124*, 5811–5826.

Qiu, B., & Huang, R. X. (1995). Ventilation of the North Atlantic and North Pacific: Subduction versus obduction. *Journal of Physical Oceanography*, *25*, 2374–2390.

Renner, A. H. H., Thorpe, S. E., Heywood, K. J., Murphy, E. J., Watkins, J. L., & Meredith, M. P. (2012). Advective pathways near the tip of the Antarctic Peninsula: Trends, variability and ecosystem implications. *Deep-Sea Research I*, *63*, 91–101.

Resplandy, L., Lévy, M., & McGillicuddy, D. J. (2019). Effects of eddy-driven subduction on ocean biological carbon pump. *Global Biogeochemical Cycles*, *33*, 1071–1084.

Richards, K., & Brentnall, S. (2006). The impact of diffusion and stirring on the dynamics of interacting populations. *Journal of Theoretical Biology*, *238*, 340–347.

Rintoul, S. R. (2018). The global influence of localized dynamics in the Southern Ocean. *Nature*, *558*, 209–218. doi: 10.1038/s41586-018-0182-3

Rintoul, S. R., & Wunsch, C. (1991). Mass, heat, oxygen and nutrient fluxes and budgets in the north atlantic ocean. *Deep Sea Research Part I. Oceanographic Research Papers*, *38*, 355–377.

Riser, S. C., Swift, D., & Drucker, R. (2018). Profiling floats in SOCCOM: Technical capabilities for studying the Southern Ocean. *Journal of Geophysical Research: Oceans*, *123*, 4055–4073.

Rödenbeck, C., Keeling, R. F., Bakker, D. C. E., Metzl, N., Olsen, A., Sabine, C., & Heimann, M. (2013). Global surface-ocean pCO_2 and sea-air CO_2 flux variability from an observation-

driven ocean mixed-layer scheme. *Ocean Science*, *9*, 193–216.

Roemmich, D., Alford, M. H., Claustre, H., Johnson, K., King, B., Moum, J., Oke, P., Owens, W. B., Pouliquen, S., Purkey, S., Scanderbeg, M., Suga, T., Wijffels, S., Zilberman, N., Bakker, D., Baringer, M., Belbeoch, M., Bittig, H. C., Boss, E., Calil, P., Carse, F., Carval, T., Chai, F., Conchubhair, D. O., d'Ortenzio, F., Dall'Olmo, G., Desbruyeres, D., Fennel, K., Fer, I., Ferrari, R., Forget, G., Freeland, H., Fujiki, T., Gehlen, M., Greenan, B., Hallberg, R., Hibiya, T., Hosoda, S., Jayne, S., Jochum, M., Johnson, G. C., Kang, K., Kolodziejczyk, N., Kortzinger, A., Traon, P.-Y. L., Lenn, Y.-D., Maze, G., Mork, K. A., Morris, T., Nagai, T., Nash, J., Garabato, A. N., Olsen, A., Pattabhi, R. R., Prakash, S., Riser, S., Schmechtig, C., Schmid, C., Shroyer, E., Sterl, A., Sutton, P., Talley, L., Tanhua, T., Thierry, V., Thomalla, S., Toole, J., Troisi, A., Trull, T. W., Turton, J., Velez-Belchi, P. J., Walczowski, W., Wang, H., Wanninkhof, R., Waterhouse, A. F., Waterman, S., Watson, A., Wilson, C., Wong, A. P. S., Xu, J., & Yasuda, I. (2019). On the future of Argo: A global, full-depth, multi-disciplinary array. *Frontiers in Marine Science*, *6*, 439.

Roesler, C., Uitz, J., Claustre, E., H. aand Boss, Xing, X., Organelli, E., Briggs, A., N. aand Bricaud, Schmechtig, C., Poteau, A., D'Ortenzio, F., Ras, J., Drapeau, S., Haentjens, N., & Barbieux, M. (2017). Recommendations for obtaining unbiased chlorophyll estimates from in situ chlorophyll fluorometers: A global analysis of WET Labs ECO sensors. *Limnology and Oceanography: Methods*, *15*, 572–585.

Rohr, T., Long, M. C., Kavanaugh, M. T., Lindsay, K., & Doney, S. C. (2017). Variability in the mechanisms controlling Southern Ocean phytoplankton bloom phenology in an ocean model and satellite observations. *Global Biogeochemical Cycles*, *31*, 922–940.

Rosso, I., Hogg, A. M., Kiss, A. E., & Gayen, B. (2015). Topographic influence on submesoscale dynamics in the Southern Ocean. *Geophysical Research Letters*, *42*, 1139–1147.

Rosso, I., Hogg, A. M., Strutton, P. G., Kiss, A. E., Matear, R., Klocker, A., & van Sebille, E. (2014). Vertical transport in the ocean due to sub-mesoscale structures: Impacts in the Kerguelen region. *Ocean Modelling*, *80*, 10–23.

Rosso, I., Hogg, A. M. C., Matear, R., & Strutton, P. G. (2016). Quantifying the influence of sub-mesoscale dynamics on the supply of iron to southern ocean phytoplankton blooms. *Deep Sea Research I*, *115*, 199–209.

Rosso, I., Mazloff, M. R., Talley, L. D., Purkey, S. G., Freeman, N. M., & Maze, G. (2020). Water mass and biogeochemical variability in the Kerguelen sector of the Southern Ocean: A machine learning approach for a mixing hot spot. *Journal of Geophysical Research: Oceans*, *125*, e2019JC015877.

Rousseaux, C. S., & Gregg, W. W. (2014). Interannual variation in phytoplankton primary production at a global scale. *Remote Sensing*, *9*, 1–19.

Russell, J. L., Kamenkovich, I., Bitz, C., Ferrari, R., Gille, S. T., Goodman, P. J., Hallberg, R., Johnson, K., Khazmutdinova, K., Marinov, I., Mazloff, M., Riser, S., Sarmiento, J. L., Speer, K., Talley, L. D., & Wanninkhof, R. (2018). Metrics for the evaluation of the Southern Ocean in coupled climate models and Earth System Models. *Journal of Geophysical Research: Oceans*, *123*, 3120–3143.

Ryan-Keogh, T. J., Thomalla, S. J., Mtshali, T. N., van Horsten, N. R., & Little, H. J. (2018). Seasonal development of iron limitation in the sub-Antarctic zone. *Biogeosciences*, *15*, 4647–4660.

Sallée, J.-B., Llort, J., Tagliabue, A., & Lévy, M. (2015). Characterization of distinct bloom phenology regimes in the Southern Ocean. *ICES Journal of Marine Science*, *72*, 1985–1998.

Sallée, J.-B., Speer, K. G., & Rintoul, S. R. (2010). Zonally asymmetric response of the Southern Ocean mixed-layer depth to the Southern Annular Mode. *Nature Geoscience*, *3*, 273–279.

Sallée, J.-B., Matear, R. J., Rintoul, S. R., & Lenton, A. (2012). Localized subduction of anthropogenic carbon dioxide in the Southern Hemisphere oceans. *Nature Geoscience*, *5*(8), 579–584. doi: 10.1038/ngeo1523

Sallée, J.-B., Shuckburgh, E., Bruneau, A., Meijers, A. J. S., Bracegirdle, T. J., & Wang, Z. (2013). Assessment of Southern Ocean mixed-layer depths in CMIP5 models: Historical bias and forcing response. *Journal of Geophysical Research: Oceans*, *118*, 1845–1862.

Sallée, J.-B., Speer, K., Rintoul, S., & Wijffels, S. (2010). Southern Ocean thermocline ventilation. *Journal of Physical Oceanography*, *40*(3), 509–529. doi: 10.1175/2009JPO4291.1

Sarmiento, J. L., Gruber, N., Brzezinski, M. A., & Dunne, J. P. (2004). High-latitude controls of thermocline nutrients and low latitude biological productivity. *Nature*, *427*, 56–60.

Sarmiento, J. L., Hughes, T. M. C., Stouffer, R. J., & Manabe, S. (1998). Simulated response of the ocean carbon cycle to anthropogenic climate warming. *Nature*, *393*, 245–249.

Sathyendranath, S., Brewin, R. J., Jackson, T., F., M., & Platt, T. (2017). Ocean-colour products for climate-change studies: What are their ideal characteristics? *Remote Sensing of Environment*, *203*, 125–138.

Schmidtko, S., Heywood, K. J., Thompson, A. F., & Aoki, S. (2014). Multidecadal warming of Antarctic waters. *Science*, *346*, 1227–1231.

Schulte, J. A., Duffy, C., & Najjar, R. G. (2015). Geometric and topologic approaches to significance testing in wavelet analysis. *Nonlinear Processes in Geophysics*, *22*, 139–156.

Sévellec, F., Naveira Garabato, A. C., Brearley, J. A., & Sheen, K. L. (2015). Vertical flow in the Southern Ocean estimated from individual moorings. *Journal of Physical Oceanography*,

45, 2209–2220.

Skinner, L. C., Fallon, S., Waelbroech, C., Michel, E., & Barker, S. (2010). Ventilation of the deep Southern Ocean and deglacial CO_2 rise. *Science*, *328*, 1147–1151.

Smith, K. M. (2017). *Effects of submesoscale turbulence on reactive tracers in the upper ocean* (Unpublished doctoral dissertation). University of Colorado Boulder.

Smith, K. M., Hamlington, P. E., & Fox-Kemper, B. (2016). Effects of submesoscale turbulence on ocean tracers. *Journal of Geophysical Research: Oceans*, *121*, 908–933.

Sobel, A. (1999). Diffusion versus nonlocal models of stratospheric mixing, in theory and practice. *Journal of Atmospheric Science*, *56*, 2571–2584.

Sokolov, S., & Rintoul, S. R. (2007). On the relationship between fronts of the Antarctic Circumpolar Current and surface chlorophyll concentrations in the Southern Ocean. *Journal of Geophysical Research*, *112*, C07030.

Sokolov, S., & Rintoul, S. R. (2009). Circumpolar structure and distribution of the Antarctic Circumpolar Current fronts: 2. Variability and relationship to sea surface height. *Journal of Geophysical Research*, *114*, C11019.

Srokosz, M., Martin, A., & Fasham, M. (2003). On the role of biological dynamics in plankton patchiness at the mesoscale: An example from the eastern North Atlantic Ocean. *Journal of Marine Research*, *61*, 517–537.

Sullivan, C. W., Arrigo, K. R., McClain, C. R., Comiso, J. C., & Firestone, J. (1993). Distribution of phytoplankton blooms in the Southern Ocean. *Science*, *262*, 1832–1837.

Sverdrup, H. U. (1953). On conditions for the vernal blooming of phytoplankton. *ICES Journal of Marine Science*, *18*, 287–295.

Swart, S., Speich, S., Ansorge, I. J., Goni, G. J., Gladyshev, S., & Lutjeharms, J. R. E. (2008). Transport and variability of the antarctic circumpolar current south of africa. *Journal of Geophysical Research*, *113*, C09014.

Swart, S., Thomalla, S. J., & Monteiro, P. M. S. (2015). The seasonal cycle of mixed layer dynamics and phytoplankton biomass in the Sub-Antarctic Zone: A high-resolution glider experiment. *Journal of Marine Systems*, *147*, 103–115.

Tagliabue, A., Mtshali, T., Aumont, O., Bowie, A. R., Klunder, M. B., Roychoudhury, A. N., & Swart, S. (2012). A global compilation of dissolved iron measurements: focus on distributions and processes in the Southern Ocean. *Biogeosciences*, *9*, 2333–2349.

Tagliabue, a. S. J.-B., A., Bowie, A. R., Lévy, M., Swart, S., & Boyd, P. W. (2014). Surface-water iron supplies in the Southern Ocean sustained by deep winter mixing. *Nature Geoscience*,

7, 314–320.

Takahashi, T., Feely, R. A., Weiss, R. F., Wanninkhof, R. H., Chipman, D. W., Sutherland, S. C., & Takahashi, T. T. (1997). Global air-sea flux of CO_2: An estimate based on measurements of sea-air pCO_2 difference. *Proceedings of the National Academy of Sciences*, *94*, 8292–8299.

Takahashi, T., Sutherland, S. C., Chipman, D. W., Goddard, J. G., Ho, C., Newberger, T., Sweeney, C., & Munro, D. R. (2014). Climatological distributions of pH, pCO_2, total CO_2, alkalinity, and $CaCO_3$ saturation in the global surface ocean, and temporal changes at selected locations. *Marine Chemistry*, *164*, 95–125.

Takahashi, T., Sutherland, S. C., Sweeney, C., Poisson, A., Metzl, N., Tilbrook, B., Bates, N., Wanninkhof, R., Feely, R. A., Sabine, C., Olafsson, J., & Nojiri, Y. (2002). Global sea-air CO_2 flux based on climatological surface ocean pCO_2, and seasonal biological and temperature effects. *Deep-Sea Research II*, *49*, 1601–1622.

Talley, L. D. (2011). *Descriptive Physical Oceanography: An Introduction*. Academic Press.

Talley, L. D. (2013). Closure of the Global Overturning Circulation through the Indian, Pacific, and Southern Oceans: Schematics and transports. *Oceanography*, *26*, 80–97.

Talley, L. D., Rosso, I., Kamenkovich, I., Mazloff, M. R., Wang, J., Boss, E., Gray, A. R., Johnson, K. S., Key, R. M., Riser, S. C., Williams, N. L., & Sarmiento, J. L. (2019). Southern Ocean biogeochemical float deployment strategy, with example from the Greenwich Meridian line (GO-SHIP A12). *Journal of Geophysical Research: Oceans*, *124*, 403–431.

Tamsitt, V., Abernathey, R. P., Mazloff, M. R., Wang, J., & Talley, L. D. (2018). Transformation of deep water masses along lagrangian upwelling pathways in the southern ocean. *Journal of Geophysical Research: Oceans*, *123*, 1994–2017.

Tamsitt, V., Drake, H., Morrison, A. K., Talley, L. D., Dufour, C. O., Gray, A. R., Griffies, S. M., Mazloff, M. R., Sarmiento, J. L., Wang, J., & Weijer, W. (2017). Spiraling pathways of global deep waters to the surface of the southern ocean. *Nature Communications*, *8*, 172.

Tamsitt, V., Talley, L. D., Mazloff, M. R., & Cerovečki, I. (2016). Zonal variations in the Southern Ocean heat budget. *Journal of Climate*, *29*, 6563–6579.

Taniguchi, D. A. A., Franks, P. J. S., & Poulin, F. J. (2014). Planktonic biomass size spectra: an emergent property of size-dependent physiological rates, food web dynamics, and nutrient regimes. *Marine Ecology Progress Series*, *514*, 13–33.

Tarling, G. A., Ward, P., Atkinson, A., Collins, M. A., & Murphy, E. (2012). DISCOVERY 2010: Spatial and temporal variability in a dynamic polar ecosystem. *Deep-Sea Research II*, *59*, 1–13.

Taylor, G. I. (1921). Diffusion by continuous movements. *Proceedings of the Royal Society A*, *20*, 196–212.

Taylor, G. I. (1923). Experiments on the motion of solid bodies in rotating fluids. *Proceedings of the Royal Society A*, *106*, 213–218.

Taylor, J. R., & Ferrari, R. (2011). Shutdown of turbulent convection as a new criterion for the onset of spring phytoplankton blooms. *Limnology and Oceanography*, *56*, 2293–2307.

Thomalla, S. J., Fauchereau, N., Swart, S., & Monteiro, P. M. S. (2011). Regional scale characterisitics of the seasonal cycle of chlorophyll in the southern ocean. *Biogeosciences*, *8*, 2849–2866.

Thomalla, S. J., Racault, M.-F., Swart, S., & Monteiro, P. M. S. (2015). High-resolution view of the spring bloom initiation and net community production in the Subantarctic Southern Ocean using glider data. *ICES Journal of Marine Science*, *72*, 1999–2020.

Thompson, A. F., & Youngs, M. K. (2013). Surface exchange between the Weddell and Scotia Seas. *Geophysical Research Letters*, *40*, 5920–5925.

Thompson, D. W. J., & Wallace, J. M. (2000). Annular modes in the extratropical circulation. Part I: Month-to-month variability. *Journal of Climate*, *13*, 1000–1016.

Tomczak, M., & Large, D. G. B. (1989). Optimum multiparameter analysis of mixing in the thermocline of the Eastern Indian Ocean. *Journal of Geophysical Research*, *94*, 16141–16149.

Torrence, C., & Compo, G. P. (1998). A practical guide to wavelet analysis. *Bulletin of the American Meteorological Society*, *79*, 61–78.

Turner, E. L., Bruesewitz, D. A., Mooney, R. F., Montagna, P. A., McClelland, J. W., Sadovski, A., & Buskey, E. J. (2014). Comparing performance of five nutrient phytoplankton zooplankton (npz) models in coastal lagoons. *Ecological Modelling*, *277*, 13–26.

Tzella, A., & Haynes, P. H. (2007). Small-scale spatial structure in plankton distributions. *Biogeosciences*, *4*, 173–179.

Uchida, T., Balwada, D., Abernathey, R. P., McKinley, G. A., Smith, S. K., & Lévy, M. (2020). Vertical eddy iron fluxes support primary production in the open southern ocean. *Nature Communications*, *11*, 1125.

Uchida, T., Balwada, D., Abernathey, R. P., Prend, C. J., Boss, E., & Gille, S. T. (2019). Southern Ocean phytoplankton blooms observed by biogeochemical floats. *Journal of Geophysical Research: Oceans*, in press.

Vanag, V. K., & Epstein, I. R. (2009). Cross-diffusion and pattern formation in reaction-diffusion

systems. *Physical Chemistry Chemical Physics*, *11*, 897–912.

van Sebille, E., Griffies, S. M., Abernathey, R., Adams, T. P., Berloff, P., Biastoch, A., Blanke, B., Chassignet, E. P., Cheng, Y., Cotter, C. J., Deleersnijder, E., Döös, K., Drake, H., Drijfhout, S., Gary, A. W., S. F¿ Heemink, Kjellsson, J., Koszalka, I. M., Lange, M., Lique, C., MacGilchrist, G. A., Marsh, R., Adame, C. G. M., McAdam, R., Nencioli, F., Paris, C. B., Piggott, M. D., Polton, J. A., Rühs, S., Shah, S. H., Thomas, M. D., Wang, J., Wolfram, P. J., Zanna, L., & Zika, J. D. (2018). Lagrangian ocean analysis: fundamentals and practices. *Ocean Modelling*, *121*, 49–75.

Vantrepotte, V., & Mélin, F. (2009). Temporal variability of 10-year global SeaWiFS time-series of phytoplankton chlorophyll *a* concentration. *ICES Journal of Marine Science*, *66*, 1547–1556.

Verdy, A., Dutkiewicz, S., Follows, M. J., Marshall, J., & Czaja, A. (2007). Carbon dioxide and oxygen fluxes in the Southern Ocean: Mechanisms of interannual variability. *Global Biogeochemical Cycles*, *21*, GB2020.

Verdy, A., & Mazloff, M. R. (2017). A data assimilating model for estimating Southern Ocean biogeochemistry. *Journal of Geophysical Research: Oceans*, *122*, 6968–6988.

Viglione, G. A., & Thompson, A. F. (2016). Lagrangian pathways of upwelling in the Southern Ocean. *Journal of Geophysical Research: Oceans*, *121*, 6295–6309.

Visbeck, M., Marshall, J., Haine, T., & Spall, M. (1997). Specifications of eddy transfer coefficients in coarse-resolution ocean circulation models. *Journal of Physical Oceanography*, *27*, 381–402.

von Berg, L., Prend, C. J., Campbell, E. C., Mazloff, M. R., Talley, L. D., & Gille, S. T. (2020). Weddell Sea phytoplankton blooms modulated by sea ice variability and polynya formation. *Geophysical Research Letters*, *47*, e2020GL087954.

Wallhead, P. J., Garçon, V. C., & Martin, A. P. (2013). Efficient upscaling of ocean biogeochemistry. *Ocean Modelling*, *63*, 40–55.

Wanninkhof, R. (2014). Relationship between wind speed and gas exchange over the ocean revisited. *Limnology and Oceanography: Methods*, *12*, 351–362.

Ward, P., Whitehouse, M., Meredith, M., Murphy, E., Shreeve, R., & Korb, R. (2002). The southern Antarctic Circumpolar Current front: physical and biological coupling at South Georgia. *Deep-Sea Research I*, *49*, 2183–2202.

Weiss, R. (1974). Carbon dioxide in water and seawater: The solubility of a non-ideal gas. *Marine Chemistry*, *2*, 203–215.

Whalen, C. B., Talley, L. D., & MacKinnon, J. A. (2012). Spatial and temporal variability

of global ocean mixing inferred from Argo profiles. *Geophysical Research Letters*, *39*, L18612.

Whitt, D. B., Lévy, M., & Taylor, J. R. (2019). Submesoscales enhance storm-driven vertical mixing of nutrients: Insights from a biogeochemical Large Eddy Simulation. *Journal of Geophysical Research: Oceans*, *124*, 8140–8165.

Whitt, D. B., Nicholson, S. A., & Carranza, M. M. (2019). Global impacts of subseasonal (<60 day) wind variability on ocean surface stress, buoyancy flux, and mixed layer depth. *Journal of Geophysical Research: Oceans*, *124*, 8798–8831.

Whitt, D. B., Taylor, J. R., & Lévy, M. (2017). Synoptic-to-planetary scale wind variability enhances phytoplankton biomass at ocean fronts. *Journal of Geophysical Research: Oceans*, *122*, 4602–4633.

Williams, N. L., Juranek, L. W., Feely, R. A., Johnson, K. S., Sarmiento, J. L., Talley, L. D., Dickson, A. G., Gray, A. R., Wanninkhof, R., Russell, J. L., Riser, S. C., & Takeshita, Y. (2017). Calculating surface ocean pCO_2 from biogeochemical Argo floats equipped with pH: An uncertainty analysis. *Global Biogeochemical Cycles*, *31*, 591–604.

Williams, N. L., Juranek, L. W., Feely, R. A., Russell, J. L., Johnson, K. S., & Hales, B. (2018). Assessment of the carbonate chemistry seasonal cycles in the Southern Ocean from persistent observational platforms. *Journal of Geophysical Research: Oceans*, *123*, 4833–4852.

Young, W. R., Roberts, A. J., & Stuhne, G. (2001). Reproductive pair correlations and the clustering of organisms. *Nature*, *412*, 328–331.

Youngs, M. K., Thompson, A. F., Flexas, M. M., & Heywood, K. J. (2015). Weddell Sea export pathways from surface drifters. *Journal of Physical Oceanography*, *45*, 1068–1085.

Zeebe, R. E., & Wolf-Gladrow, D. (2001). *CO_2 in Seawater: Equilibrium, Kinetics, Isotopes*. Elsevier.

Zhou, M., Zhu, Y., Measures, C. I., Hatta, M., Charette, M. A., & Gille, S. T. (2013). Winter mesoscale circulation on the shelf slope region of the southern Drake Passage. *Deep-Sea Research II*, *90*, 4–14.